2017

Spin and Charge Transport in Graphene Based Devices

Marta Anguera Antonana
University of Central Florida

SPIN AND CHARGE TRANSPORT IN GRAPHENE BASED DEVICES

by

MARTA ANGUERA ANTONANA
B.S. Universitat de Barcelona, 2011
M.S. University of Central Florida, 2015

A dissertation submitted in partial fulfillment of the requirements
for the degree of Doctor of Philosophy
in the Department of Physics
in the College of Science
at the University of Central Florida
Orlando, Florida

Summer Term
2017

Major Profesor: Enrique del Barco

ABSTRACT

The present dissertation is comprehended in two main parts. The first part is focused on understanding the mechanisms behind spin current to charge current interconversion (*i.e.* the spin Hall angle), where the spin current is generated by means of spin pumping. The measurement of a positive spin Hall angle of magnitude 0.004 in Uranium is reported in Chapter 2. These results support the idea that the electronic configuration may be at least as important as the atomic number in governing spin Hall effects. In Chapter 3, the design of a spintronics device designed to interconvert charge and spin currents in CVD graphene is presented.

The second part of the thesis is centered in the study of transport through single molecules with the use of three-terminal devices. The first evidence of a molecular double quantum dot is detailed in Chapter 5. The conclusions are supported by self-assembled monolayers (SAMs) and single-electron transistors (SETs) measurements. Using gold electrodes for SETs measurements has its disadvantages, two of the main ones being: the junctions are not stable at room temperature and it does not allow for transport measurements in the presence of light. Graphene electrodes, on the other hand, have been reported to be stable at temperatures above room temperature and have no absorption in the visible range. Along those lines, the development of a multilayer graphene-based SET is reported in Chapter 6. Finally, a new technique, based on CVD graphene transistors, that will allow three-terminal measurements on an STM is described in Chapter 7.

To my parents, for their love and support

ACKNOWLEDGMENTS

I would not have been able to complete my PhD without the support and help from my family, friends and colleagues and I would like to use this section to thank each and every one of them.

First of all, I would like to thank my advisor, Dr. Enrique del Barco, for all the support over the years and for giving me the opportunity to do research at UCF. Thank you for the two summers at NUS in Singapore (amazing cleanroom and food!), for having the steadiest hands and, against all odds, saving some of my devices with silver paint and, most importantly, thank you for challenging me to always be better.

I also want to thank current and past members of "del Barco's" group: Hajra, Asma, Simran (expert of everything in the lab), Jim, Rebecca, Priyanka (or "chamber lady"), Cameron (the wirebonder and jinx of the group), Gyan and the undergrads: Chris (the lab's handyman) and Tyler (competing with Cameron for jinx of the group). All of you have made the lab a second home to me.

Thanks to my committee members: Dr. Robert Peale, Dr. Aniket Battacharya and Dr. Winston Schoenfeld and thanks to Dr. Masahiro Ishigami and his group (Jyoti, Ryuichi, Mike and Brandon) for being like my second group, helping me with graphene exfoliation, SEM writing and STM measurements.

Thanks to UCF and the Department of Physics for giving me the means to finish my PhD without having to worry too much about the money. And thank you: Dr. Eduardo Mucciolo, Dr. Talat Rahman, Jessica, Monika, Esperanza, Elizabeth, Pat, David and Felix for all your help over the years. Special thanks to Dr. Elena Flitsiyan, for being the best lab coordinator one could ever ask for.

The first year of PhD is one of the hardest; away from home, missing family and friends. This is why I could not have been able to succeed without my first-year classmates and now friends: Roxana, Dan, Khan, Tomas.

Thanks to all my "Orlando" friends for all the good times spent together: Tracy, Chris and the Spaniards (Belen, Javi, Irene, Angel, Carlota, Noelia …). I hope to see you all in Portland!

I cannot finish this section without thanking Alvar, you made everything easier since the beginning: helping me in my first class as an instructor ever (I was terrified!), finding the first apartment, introducing me to all your friends making sure I didn't feel alone, … and I could keep on writing without ending. You have pushed me to be better in my PhD and as a person. Thank you for everything, I cannot wait to join you in Portland.

Finally, I want to thank my family. Thanks to my parents for all the support since ALWAYS and for taking loving care of me, I really love it when you come and visit me in Orlando. Nina and I miss you! Also, thanks to my cousin Laura and my aunt and uncle for receiving me with so much love every time I come back to Barcelona. And to finish, thanks to my grandmother ("iaia") who could not see me graduate. Us estimo!

TABLE OF CONTENTS

LIST OF FIGURES

LIST OF TABLES

CHAPTER 1:
INTRODUCTION: DYNAMICAL SPIN PUMPING

1.1. Introduction

The control and manipulation of the spin and charge of electrons in nanoscale systems has developed into a very active field of research during the past few years, prompted by possible applications in emerging technologies, for instance spintronics and molecular electronics. Spintronics final goal is to actively manipulate the spin degree of freedom of electrons. In addition, it has the potential to provide smaller, non-volatile memory devices than standard CMOS [1]. It has also been demonstrated that pure spin current devices offer advantages over spin and charge current devices, the main one being reduced power dissipation [2]. Chapter 1, 2 and 3 will be focused on studying a particular technique for obtaining pure spin currents: Dynamical spin injection.

On the other hand, molecular electronics is another very promising substitute to silicon nanoelectronics [1]. The idea that single molecules could replace every electric component in a circuit represents a final miniaturization for devices [3]. Molecules have already been functionalized to act as diodes, transistors and switches, to name a few [2]. To advance in the field, the electronic properties of single-molecules must be studied and only few techniques allow the study of transmolecular conduction, scanning tunneling microscopy (STM) and single-electron transistors (SETs) spectroscopy are two of them [2]. Chapter 5 demonstrates single-molecule transport on a molecular double quantum dot, Chapter 6 reports the development of a multilayer graphene SET, and in Chapter 7 a newly developed STM technique is presented.

1.2. Dynamical Spin Pumping

As indicated in the introduction, pure spin currents offer further advantages in spintronics applications: reduced power dissipation, absence of stray Oesterd fields, and decoupling of spin and charge, to name a few [2]. Different experimental techniques can be used to obtain spin currents, for instance: nonlocal electrical injection from ferromagnetic contacts; spin Hall effect; thermal gradients; and spin pumping. The present chapter focuses on the generation of spin current by dynamical spin injection or spin pumping.

In spin pumping, the precessing magnetization of an externally excited ferromagnet undergoing ferromagnetic resonance (FMR) is dynamically coupled to the charge carriers in an adjacent non-magnetic system, resulting in a net transfer of spin angular momentum across the ferromagnet/non-magnetic (FM/NM) interface [4].

1.2.1. Ferromagnetic Resonance

At microwave frequencies, spin resonance in ferromagnets is similar to nuclear and electron spin resonance [5]. In a system of electronic or nuclear spin moments, the resonance arises when there is a Zeeman splitting of the energy levels, as a result of a uniform magnetic field being applied, and the system absorbs energy from an oscillating magnetic field at the frequencies that correspond to the transitions between levels (*Equation 1.1*). [6]

$$\hbar\omega = \Delta E_{mn} \tag{1. 1}$$

where $\hbar$ is the reduced Planck's constant and ω is the frequency of the electromagnetic radiation.

The value of the energy difference between the levels *m* and *n* is defined by *Equation 1.2*:

$$\Delta E_{mn} = g\mu_B \Delta m_{mn} H_0 \tag{1. 2}$$

where g is the Lande factor, μ_B is the Bohr magneton, Δm_{mn} is the difference of the magnetic quantum numbers of the states *m* and *n* and H_0 is the external magnetic field [7].

Combining *Equations 1.1* and *1.2* we obtain the resonant condition:

$$\omega_{res} = \frac{g\,\mu_B}{\hbar} \Delta m_{mn} H_0 \tag{1. 3}$$

The values of the differences Δm_{mn} are limited by selection rules, which for a dipole radiation and given that for a Zeeman multiplet all levels have different quantum number ($m \neq n$), are the following:

$$\Delta m_{mn} = \pm 1 \tag{1. 4}$$

For transitions that obey $\Delta m_{mn} = \pm 1$, the plane of polarization is perpendicular to the applied external magnetic field H_0. In other words, to achieve the resonance condition the oscillating magnetic field (H_{ac}) must be perpendicular to H_0 [8]. Taking into consideration selection rules and using *Equation 1.3* we can write a simplified expression for ω_{res}:

$$\omega_{res} = \gamma\, H_0 \tag{1. 5}$$

where,

$$\gamma = \frac{g\,\mu_B}{\hbar} = g\,\frac{e}{2\mathrm{mc}} \tag{1. 6}$$

Sometimes it is more convenient in experiments to set a constant frequency and sweep the magnetic field. In that case, we can express the resonant condition in terms of the frequency:

$$H_{res} = \frac{1}{\gamma}\omega_0 \tag{1. 7}$$

It is significant that we can express ω_{res} (*Equation 1.5)* without the Planck's constant. Which means that it is possible to use a classical approximation not only in the case of atomic magnetic resonance but also in the treatment of magnetic resonance phenomena in solids.

The difference in the resonance condition between an isolated atom and a ferromagnet is the strong exchange interaction between the electrons in the latter. Because of the exchange interaction, the uncompensated magnetic spin moments of the atoms in the ferromagnet orient parallel to each other, which leads to the need of an effective field in *Equation 1.5*. Due to the effective field, if the magnetization shifts from the equilibrium position it will start precessing around H_{eff} at the Larmor frequency (*Figure 1*). The classical equation of motion that describes the system is:

$$\frac{dm}{dt} = -\gamma[m \times \mathrm{H}] \tag{1. 8}$$

where m is the mean magnetization per unit volume, γ is the gyromagnetic ratio and $\boldsymbol{H} = \boldsymbol{H}_{ac} + \boldsymbol{H}_0$

Near the Larmor frequency the magnetic susceptibility depends on the frequency of the electromagnetic radiation and the energy absorption is maximum. The width and shape of the absorption line have a strong dependence on the internal interactions in the ferromagnet (exchange interaction, dipole-dipole interaction, spin-orbit interaction…) as well as on its shape

and symmetry. Thus, FMR study provides very detailed information of the different properties of the system under study.

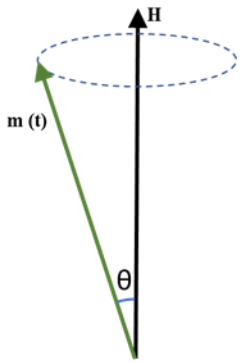

Figure 1: Graphical representation of the precession of the magnetization about a uniform magnetic field in the absence of an A.C magnetic field.

Equation 1.8 depicts a correct description of the system when energy losses are not present. Bearing that in mind, *Equation 1.9* was suggested by L. D. Landau and E. M. Lifshitz, introducing a damping term to *Equation 1.8*:

$$\frac{dm}{dt} = -\gamma[m \times H] - \alpha \frac{\gamma}{M_S}[m \times [m \times H]] \qquad (1.9)$$

where $\alpha = \lambda/\gamma M$ is a non-dimensional damping parameter and λ characterizes the dipole-dipole interaction in the ferromagnet.

For pulsed remagnetization processes the previous equation is not precise, the increment of the damping parameter is inversely proportional to the time of total reorientation of the magnetization. In order to correct this issue, Gilbert modified *Equation 1.9*:

$$\frac{dm}{dt} = -\gamma[m \times H] + \frac{\alpha}{M_S}[m \times \frac{\mathrm{dm}}{dt}] \qquad (1.\ 10)$$

The first term on the right-hand side represents the precessional torque and the second term represents the Gilbert damping torque. In the limit of small damping (α / M_S << 1), *Equation 1.9* and *1.10* are equivalent [9]. In the majority of experiments the relation α / M_S << 1 is true.

In Gilbert's equation, the relaxation term is proportional to the rate of change of the magnetization in time. Figure 2a shows a graphical representation of the two different torques acting on the magnetization vector, while Figure 2b is an illustration of the trajectory of the time dependent magnetization under the action of damping.

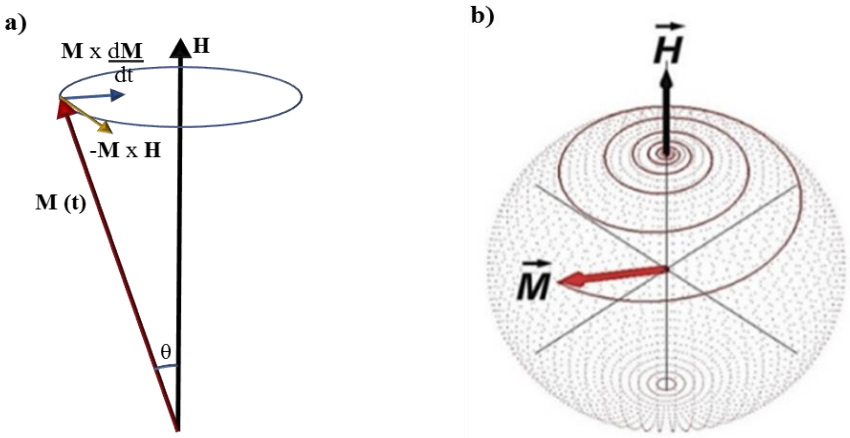

Figure 2: a) Schematics of the magnetization vector (M), the applied magnetic field (H), the precessional torque (-M x H) and the Gilbert damping torque (M x $\frac{dM}{dt}$). b) Damped precession of the magnetization vector. The magnetization spirals down along the field direction and gradually approaches equilibrium position.

1.2.2. Theory of Precession-Induced Spin Pumping

Yaroslav Tserkovnyak and Arne Brataas developed the theory of spin pumping in 2002 to explain why the Gilbert damping constant was found to be dependent on the substrate and capping layer of the ferromagnet. Their theory demonstrates that the enhancement of the Gilbert

damping constant is due to a transfer of spins between the ferromagnet and the adjacent normal metal [4,10], *i.e.*, the precessing magnetization vector transfers spin angular momentum into the normal metal.

Tserkovnyak et al. [10] derived the adiabatic spin pumping theory via scattering theory. Considering a Ferromagnet/non-magnetic junction (FM/NM for future references), in the absence of voltage bias no charge currents flow and if the magnetization is constant in time there will be no spin currents. Once an external magnetic field is applied, the magnetization of the FM will start precessing, transferring spin angular momentum to the NM (*Figure 3*).

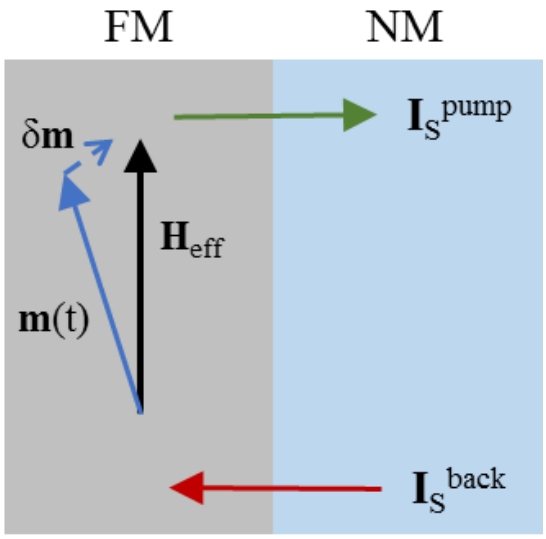

Figure 3: At the interface between a ferromagnet and a normal metal, the precession of the magnetization (m(t)) induces a spin current in the NM (I_S^{pump}). I_S^{back} represents the spin current that flows back to the ferromagnet. Figure based on reference [13].

The pumped current is given by:

$$I_S^{pump} = \frac{\hbar}{4\pi}\left(A_r m \times \frac{dm}{dt} - A_i \frac{dm}{dt}\right) \quad (1.\ 11)$$

where $A \equiv A_r + iA_i$ is the spin-pumping conductance parameter and $\boldsymbol{m}(t)$ is the unit vector of the magnetization of the ferromagnet.

The spin-pumping conductance can be written in terms of the transmission and reflection coefficients:

$$A = g^{\uparrow\downarrow} - t^{\uparrow\downarrow} \tag{1. 12}$$

$g^{\uparrow\downarrow}$ being the complex interfacial mixing conductance and $t^{\uparrow\downarrow}$ the transmission matrix. In ferromagnetic films thicker than their spin-coherence length, $t^{\uparrow\downarrow}$ vanishes and the spin pumping through the FM/NM interface is governed by $g^{\uparrow\downarrow}$.

Previous calculations seem to indicate that A_i is very small for Cu/Co and Fe/Cr [11], and it vanishes in nonmagnetic tunnel barriers and in ballistic and diffusive contacts [12]. Consequently, A_i may be neglected in many systems. If that is the case, the spin current pumped into the NM is:

$$I_S^{pump} = \frac{\hbar}{4\pi} g_r^{\uparrow\downarrow} m \times \frac{dm}{dt} \tag{1. 13}$$

where $g_r^{\uparrow\downarrow}$ is the real part of the interfacial mixing conductance.

In order to generalize the theory of spin pumping and consider the spin build-up in the NM, the backflow of spin current into the FM ($\boldsymbol{I}_S^{back}$) has to be included. The total spin accumulation can be written as:

$$I_S = I_S^{pump} - I_S^{back} \tag{1. 14}$$

As a first approximation, we are going to assume $\boldsymbol{I}_S^{back} \approx 0$. The model will be valid for highly conductive metals with effective spin-flip processes that prevent any backscattering into the FM [13]. Taking that into consideration, the total spin current transferred to the NM is:

$$\mathrm{I}_S = \frac{\hbar}{4\pi} g_r^{\uparrow\downarrow} m \times \frac{dm}{dt} \tag{1. 15}$$

Note that $\boldsymbol{I}_S$ represents the instantaneous spin-pumping current at the interface. Pure spin currents are not conserved in real systems, spins relax over the NM spin diffusion length and the accumulated spin density diffuses across the NM (*Figure 4*). The spin accumulation diffuses according to [2, 13]:

$$i\omega\mu_S = D\frac{\partial^2 \mu_S}{\partial x^2} - \frac{\mu_S}{\tau_{Sf}} \tag{1. 16}$$

where ω is the precession frequency, $\boldsymbol{\mu_S}$ is the spin accumulation (difference in local electrochemical potentials of up and down spins), D is the diffusion coefficient and τ_{sf} is the spin-flip time.

Equation 1.16 is valid for $\tau/\tau_{sf} << 1$, that is, the spin-flip relaxation can be treated as a perturbation (τ is the transport mean free time). The boundary conditions for *Equation 1.16* are set by the continuity of the spin current at the interface ($x = 0$) and the vanishing of $\boldsymbol{I}_S$ for $x = t_N$:

$$x = 0: I_S(x = 0) = -D\frac{\partial \mu_S}{\partial x} \tag{1. 17}$$

$$x = t_N: \frac{\partial \mu_S}{\partial x} = 0 \tag{1. 18}$$

where t_N is the thickness of the normal metal and λ_{sd} is the spin diffusion length.

Solving *Equation 1.16* for the previous boundary conditions, we find the spin current density [2]:

$$I_S(x) = I_S \frac{\sinh[\frac{x-t_N}{\lambda_{sd}}]}{\sinh(t_N/\lambda_{sd})} \tag{1. 19}$$

The spin accumulation in the metal produces a spin backflow into the FM. This effect can be considered by replacing $g_r^{\uparrow\downarrow}$ in *Equation 1.15* with an effective spin mixing conductance $g_{eff}^{\uparrow\downarrow}$:

$$g_{eff}^{\uparrow\downarrow} = \frac{4\pi\gamma M_S t_{FM}}{g\mu_B\omega_f}(\Delta H_{FM/NM} - \Delta H_{FM}) \tag{1. 20}$$

where γ is the gyromagnetic ratio, M_S is the FM saturation magnetization in T, t_{FM} is the thickness of the FM, μ_B is the Bohr magneton, ω_f is the microwave angular frequency and ΔH is the linewidth of the FMR signal [10].

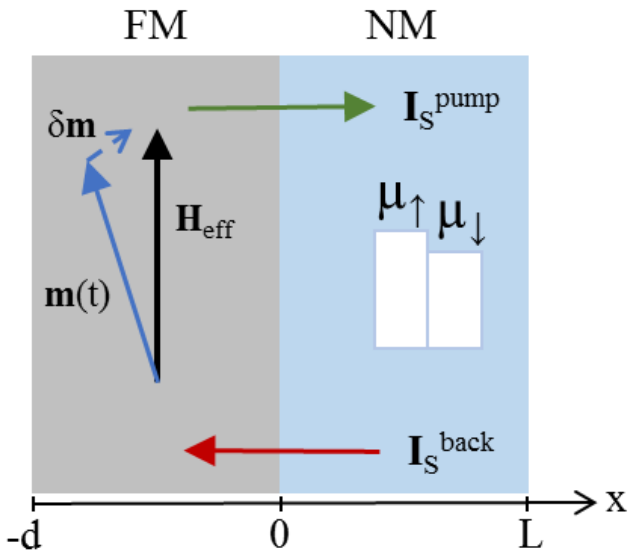

Figure 4: In a real material, the spin current pumped at the interface builds up a spin accumulation dependent on the position. This spin accumulation can relax by spin-flip scattering or flow back into the ferromagnet. Figure based on reference [13].

Combining *Equations 1.15, 1.19* and *1.20*, we obtain a final expression for $\boldsymbol{I_s(x)}$:

$$I_S(x) = \frac{\hbar}{4\pi} \frac{\sinh\left[\frac{x-t_N}{\lambda_{sd}}\right]}{\sinh(t_N/\lambda_{sd})} g_{eff}^{\uparrow\downarrow} (m \times \frac{dm}{dt}) \qquad (1.\ 21)$$

1.2.3. Spin Pumping Formulation in Thin Films

According to *Equation 1.21*, $\boldsymbol{I}_S$ depends on the variation of the magnetization with time (*i.e.*, the trajectory of the magnetization precession). In thin films the magnetization precession trajectory is conditioned to the angle between the magnetization and the normal plane of the film (*Figure 5*). The following section is dedicated to the formulation of the spin pumping theory regarding thin films.

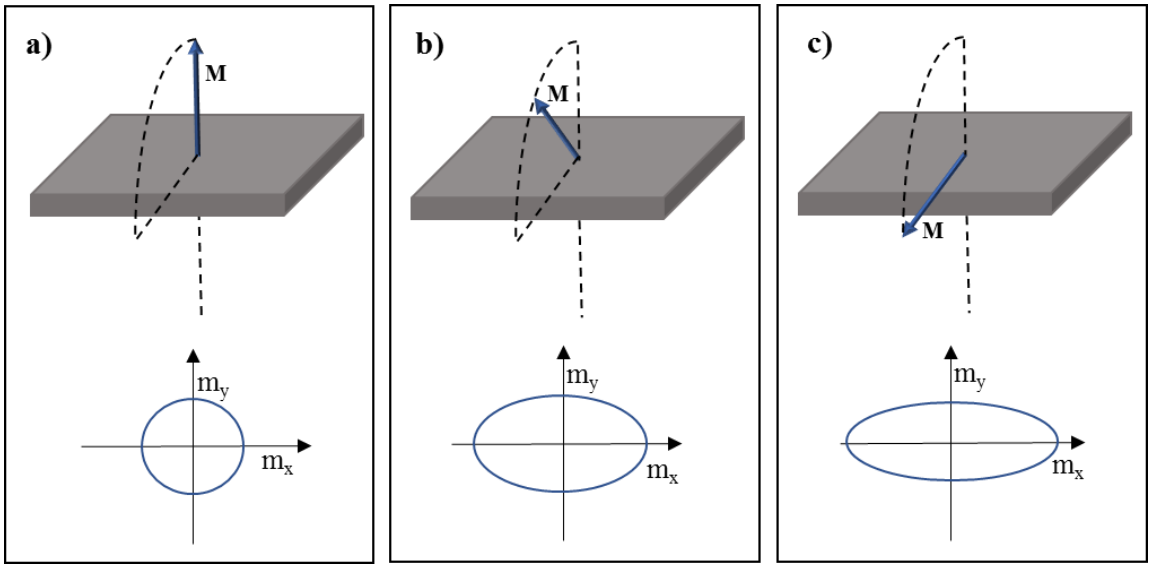

Figure 5: Graphical representation of the magnetization precession trajectory for different angles between the magnetization-precession axis and the film plane. a) Magnetization-precession axis perpendicular to the film plane. b) Magnetization-precession axis oblique to the film plane. c) Magnetization-precession axis parallel to the film plane. Figure based on reference [14]

In equilibrium conditions, we set the direction of the magnetization $\boldsymbol{M}$ parallel to the *z* axis (*Figure 6*) and neglect the magnetocrystalline anisotropy. The total effective field is given in terms of the external magnetic field $\boldsymbol{H}$ and the static demagnetizing field $\boldsymbol{H}_M$. The demagnetizing magnetic field is conditioned to the shape and anisotropy of the ferromagnet. The terms for *Equation 1.24* are taken from reference [14].

$$H_{eff} = H + H_M \tag{1. 22}$$

where

$$H = H\begin{pmatrix} 0 \\ \sin(\theta_M - \theta_H) \\ cos(\theta_M - \theta_H) \end{pmatrix} \tag{1. 23}$$

$$H_M = -M_S cos\theta_M \begin{pmatrix} 0 \\ \sin\theta_M \\ \cos\theta_M \end{pmatrix} \tag{1. 24}$$

H is the strength of the external magnetic field, θ_M and θ_H are the magnetization angle and the external magnetic field angle to the normal axis of the film plane (*Figure 6*) [14]. $\boldsymbol{M} \times \boldsymbol{H}_{eff} = 0$ (static equilibrium condition) leads to the following condition:

$$2Hsin(\theta_M - \theta_H) + M_S sin2\theta_M = 0 \tag{1. 25}$$

Now, taking into account an external ac field $\boldsymbol{h}(t)$ and the consequent small precession of the magnetization $\boldsymbol{m}(t)$ that it induces:

$$H_{eff}(t) = H + H_M + H_m(t) + h(t) \tag{1. 26}$$

where

$$H_m(t) = -4\pi m_y(t) sin\theta_M \begin{pmatrix} 0 \\ sin\theta_M \\ cos\theta_M \end{pmatrix} \quad (1.\ 27)$$

$$h(t) = \begin{pmatrix} he^{i\omega t} \\ 0 \\ 0 \end{pmatrix} \quad (1.\ 28)$$

$$m(t) = (m_x e^{i\omega t}, m_y e^{i\omega t}, 0) \quad (1.\ 29)$$

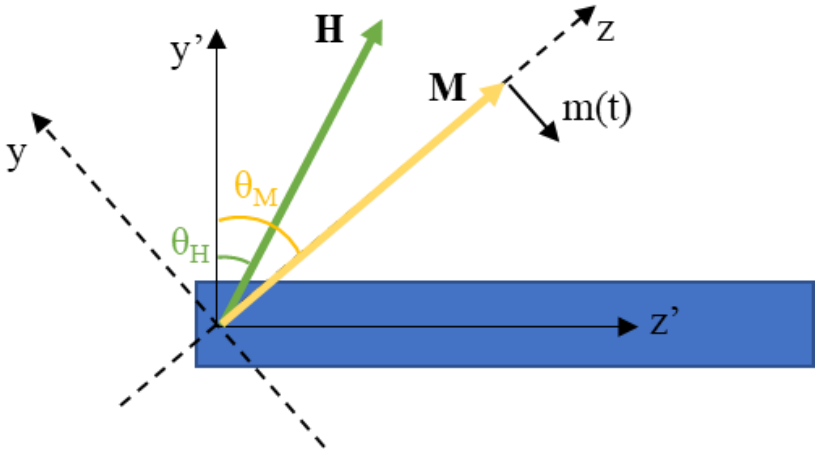

Figure 6: A schematic illustration of the coordinate system used for describing a ferromagnetic film (blue in the figure). M and m(t) are the static and dynamic components of the magnetization. H is the external magnetic field. θ_M and θ_H are the magnetization angle and the external magnetic field angle to the normal axis of the film plane. Figure based on reference [14].

The resonance condition can be obtained from *Equation 1.10*, neglecting the external ac field, the damping term and disregarding second order contributions from the precession amplitude (*Equation 1.30*):

$$\left(\frac{\omega}{\gamma}\right)^2 = [H_{FMR}cos(\theta_M - \theta_H) - M_S cos2\theta_M] \times [H_{FMR}cos(\theta_M - \theta_H) - M_S cos^2\theta_M] \quad (1.\ 30)$$

We can now solve *Equation 1.10* for the different components of the time dependent magnetization ***m****(t)* by means of the relationships set in *Equations 1.25* and *1.30*:

$$m_x(t) = \frac{M_S h\gamma\left\{2\alpha\omega cos\omega t + \left[M_S\gamma sin^2\theta_M + \sqrt{(M_S)^2\gamma^2 sin^4\theta_M + 4\omega^2}\right] sin\omega t\right\}}{8\pi\alpha\omega\sqrt{(M_S)^2\gamma^2 sin^4\theta_M + 4\omega^2}} \quad (1.\ 31)$$

$$m_y(t) = -\frac{M_S h\gamma cos\omega t}{4\pi\alpha\sqrt{(M_S)^2\gamma^2 sin^4\theta_M + 4\omega^2}} \quad (1.\ 32)$$

Finally, time averaging *Equation 1.15* for one period of precession and combining it with *Equations 1.31* and *1.32* we find a general expression for the spin current density at the interface between a thin film of a FM and a NM:

$$I_s = \frac{g_{eff}^{\uparrow\downarrow}\gamma^2 h^2 \hbar\left[4\pi M_S\gamma sin^2\theta_M + \sqrt{(4\pi M_S)^2\gamma^2 sin^4\theta_M + 4\omega^2}\right]}{8\pi\alpha^2[(4\pi M_S)^2\gamma^2 sin^4\theta_M + 4\omega^2]} \quad (1.\ 33)$$

CHAPTER 2:
MODERATE POSITIVE SPIN HALL ANGLE IN URANIUM

2.1. Introduction

The present chapter is based on the work published in Applied Physics Letters [27].

Spin pumping has been studied in a wide variety of materials, including transition metals [2,14,15], organic materials [17] and two-dimensional crystals [18-20], among others. Experimentally, the pumped spin current can be detected as an enhancement of the Gilbert damping in the ferromagnet. The injected spin current can be converted into an electrical signal by the inverse spin Hall effect (ISHE) for non-magnetic layers with sufficiently large spin-charge current interconversion [21, 22]. The latter has a figure of merit known as the spin Hall angle, θ_H, defined as the ratio of the inject spin current and resulting charge current.

It is generally understood that the spin-orbit coupling, and consequently the spin Hall angle, scales as Z^4 (being Z the atomic number) [17, 18, 23]. Indeed, most spin pumping and ISHE studies concentrate on metals with high spin-orbit coupling [18-20, 24]. However, a recent systematic study with transition metals shows that the spin Hall angle is strongly modulated by the orbital filling and can become comparable to that obtained in some heavy metals [18]. This indicates that the electronic structure is quite important in determining spin Hall conductivities and spin Hall angles, leaving the ultimate importance of the atomic number at a secondary level. Therefore, exploring higher atomic number elements in the periodic table is an important direction for understanding the underlying mechanisms governing the spin Hall effect in non-magnetic materials.

As pointed out by Tanaka *et al*. [18-20, 23], the higher magnetic moment and the smaller band splitting near the Fermi surface of *f*-electron systems when compared to *d*-electron elements, place Lanthanides and Actinides as excellent candidates to display "giant" spin Hall and orbital Hall effects. In this context, this chapter reports the experimental realization of spin pumping and subsequent electrical detection of the generated spin current in the actinide metal Uranium, a super-heavy *f*-electron metal whose atomic number (Z = 92) is larger than any element studied to date in the context of spintronics.

2.2. Sample Preparation

Thin layers of permalloy (Py; $Ni_{80}Fe_{20}$) and bilayers of permalloy/uranium (Py/U) were deposited using a dedicated actinide sputter deposition chamber [25]. DC magnetron sputtering was employed to synthesize samples with thicknesses, t_{Py} and t_U of 12.5 nm and 3 nm, respectively. 3 nm of Nb was used as a capping layer to prevent oxidation of the underlying films. The growth rates were held between 0.05 and 0.1 nm/s in an argon pressure of 7×10^{-3} mbar at a temperature of 300 K. The films were deposited onto BK7 glass with rms surface < 0.5 nm. Depleted uranium sputtering targets are commercially available.

2.3. FMR Measurements

2.3.1. Experimental set-up

As explained in *Section 1.2.*, in order to perform FMR studies a dc magnetic field and a perpendicular a.c. magnetic field need to be applied to the sample. In our experiment, the d.c magnetic field is applied using an electromagnet (*Figure 7a*) with the capability of supplying approximately 1 Tesla. The electromagnet can be rotated 360 degrees, which allows for the

angular dependence studies of the FMR signal. The a.c. magnetic field is achieved by using on-chip co-planar waveguides (CPW) fabricated on an insulating substrate (undoped GaAs) by means of optical lithography (*Figure 7b*).

The CPW design must follow specific guidelines to minimize losses. The most important one being that the impedance throughout the entire CPW has to match the impedance of the microwave source (50 Ohms). This fact sets a relationship between the central line and the gap widths. *Figure 7b* shows a picture of a CPW with its critical dimensions [26].

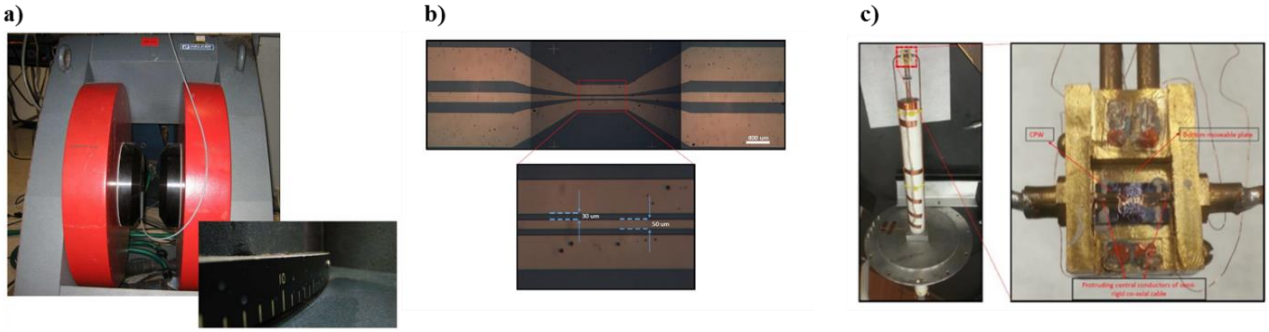

Figure 7: a) Picture of the electromagnet used for the experiments. b) Optical image of a CPW patterned on a GaAs substrate with a closer look that shows the dimensions of the central line and the gap. c) Picture of a CPW mounted on the housing box.

To maximize the magnetic field lines density, the width of the central line is reduced in the area where the sample is going to be placed [27]. The pattern becomes wider at both ends in order to facilitate the connection to the coaxials. The CPW is then placed inside a custom-built housing box that will connect the CPW to the microwave source. The housing box containing the CPW is attached to a solid probe (*Figure 7c*) that will be positioned between the poles of the electromagnet.

Before proceeding to measure the sample, the CPW must be characterized. The transmission characterization is done with an Agilent Technologies Performance Network Analyzer (PNA). The PNA will send a microwave signal through port P1 and will measure the signal received in port P2. The transmission spectra of one of our CPWs is shown in *Figure 8a*.

The sample is then placed upside-down on top of the CPW. During FMR measurements, the dc magnetic field is swept while the PNA sends constant frequency microwave radiation and measures the transmission coefficient. A Labview program is used to record the data and control the different elements of the circuit. A schematic of the set-up is shown below (*Figure 8b*).

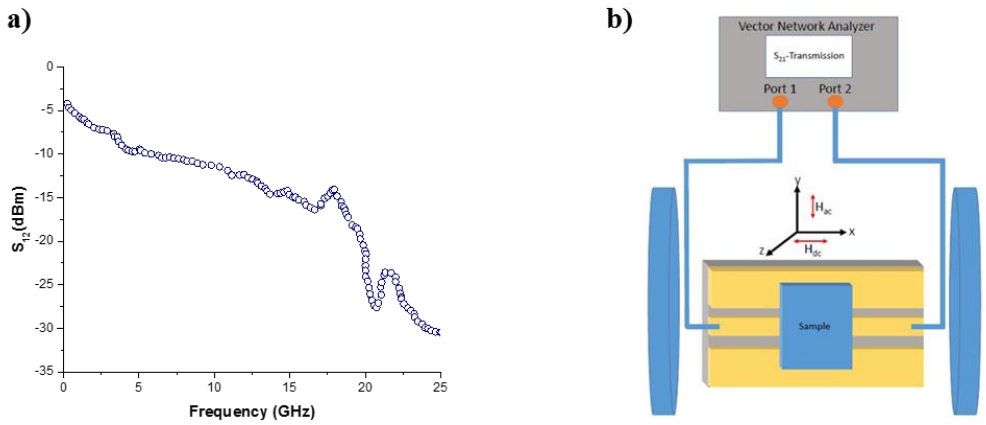

Figure 8: a) Transmission spectra of an on-chip CPW measured with the PNA between 100MHz and 25GHz. b) Schematic of the FMR measurement set-up with the CPW situated between the two poles of the electromagnet and connected to the two ports of the PNA. In this geometry, the ac magnetic field will oscillate in the y direction while the dc magnetic field can be applied on the xz plane.

2.3.2 Results

The transmission absorption spectra of the two different set of samples (Py and Py/U) were measured for frequencies up to 18 GHz with the external dc magnetic field applied in-plane (*Figure 9 a-b*). The observed frequency dependence of the FMR linewidth for the Py and Py/U samples is shown in *Figure 10* [27].

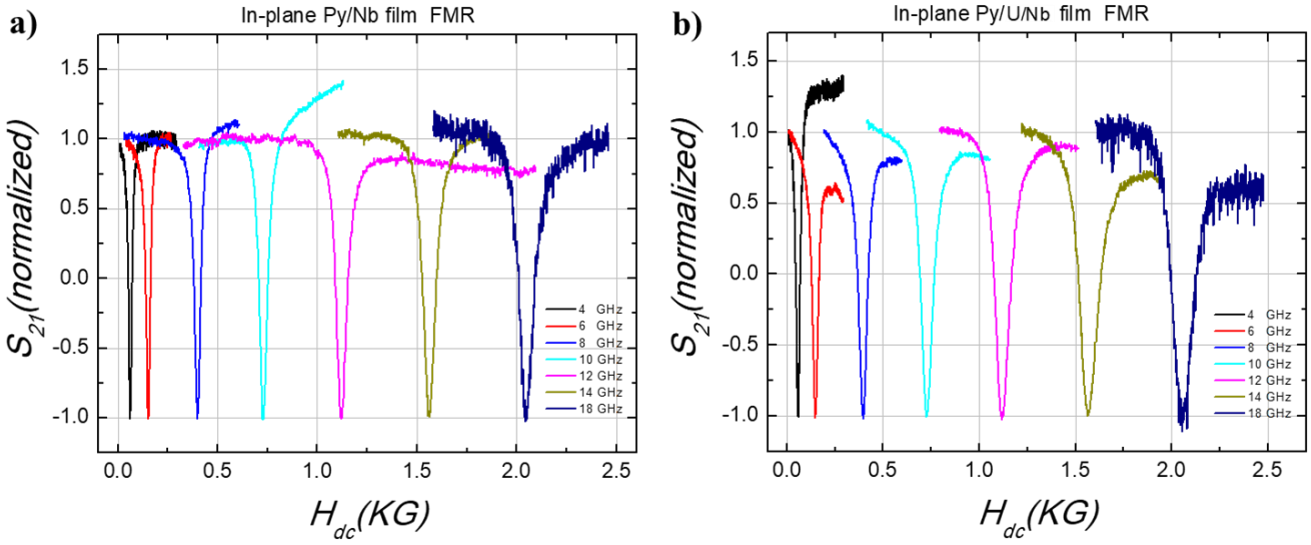

Figure 9: In-plane FMR signals for: a) the Py/Nb and b) the Py/U/Nb samples at eight different frequencies: 4 GHz, 6 GHz, 8 GHz, 10 GHz, 12 GHz, 14 GHz and 18 GHz.

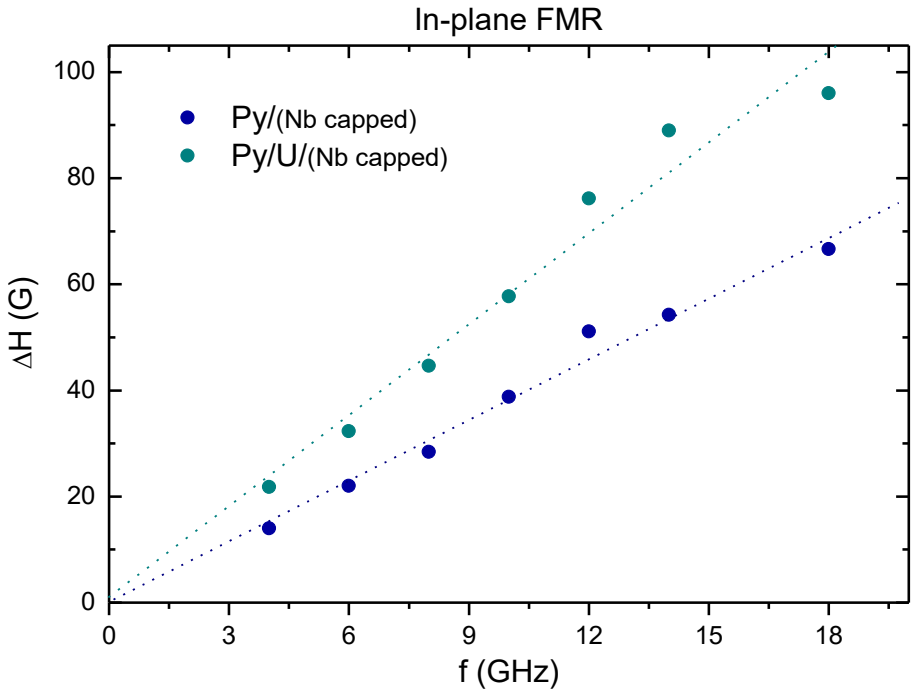

Figure 10: Frequency dependence of the FMR linewidths for Py/Nb and Py/U/Nb samples.

The presence of Uranium substantially increases the FMR linewidth at all frequencies, while it does not alter the quality of the Py film (as inferred from the linear behavior of the data and the zero-width frequency intercepts). This implies an enhancement of the magnetic damping of Py film due to spin pumping into the U layer. The damping is determined via the slope of the linewidth with frequency, as per the phenomenological Gilbert damping model [13]:

$$\delta H = \delta H_0 + \frac{4\pi\alpha}{\sqrt{3}\,\gamma} f \qquad (2.\ 1)$$

The first term in *Equation 2.1* is the frequency independent inhomogeneous broadening, which is negligible in the samples studied here. The second term denotes the dynamical damping. The extracted damping parameters for both samples are represented in *Table 1*:

Table 1:Values of the damping parameter α and the Gilbert damping parameter G for the samples of Py and Py/U. The Gilbert damping damping parameter is related to α as $G = \alpha\gamma M_s$, with M_s (= 9.5 kG) being the saturation magnetization. The saturation magnetization is obtained from the dependence of the magnetic field position of the FMR peak with frequency.

	α	**G (GHz)**
Py	9.6×10^{-3}	0.257
Py/U	14.3×10^{-3}	0.384

The observed damping enhancement (150%) can be understood as a direct consequence of the spin pumping mechanism which transfers angular momentum from the ferromagnet into the Uranium. The efficiency of spin pumping across the Py/U interface is given by the spin-mixing conductance [13]:

$$g_r = \frac{4\pi M_s t_{Py}}{\gamma h}\,(\alpha_{Py/U} - \alpha_{Py}) \qquad (2.\ 2)$$

where t_{Py} is the Py thickness. Using the damping parameters obtained from the linewidth-frequency data and the saturation magnetization of the Py [28]:

$$g_r^{\uparrow\downarrow} = 2.28\times10^{19} m^{-2} \quad (2.\ 3)$$

This value is comparable to those found in Py/heavy-metal interfaces. One needs to keep in mind that *Equation 2.2* assumes that no spins flow back into the Py film. This assumption should hold for this thickness of Uranium owing to its large expected spin-orbit coupling and hence small spin diffusion length, which, while unknown at this moment, should be, at least, comparable to those found in heavy metals (*e.g.*, 1-4nm in Pt) [29,30].

This spin mixing conductance value should be taken as a lower bound for Py/U since it comes from comparison measurements between Py and Py/U samples, both capped with a 3nm Nb layer. The Nb already contributes to the magnetic damping in the Py/Nb control sample, which enhances the damping slightly from that of isolated Py. Consequently, using the damping change observed between Py/Nb and Py/U/Nb samples would underestimate the spin-mixing conductance of the Py/U interface.

2.4. ISHE Measurements

2.4.1. Experimental set-up

Next, we turn our attention to the experimental realization of spin-charge conversion in Uranium. The sample was placed on the bottom plate of a high-quality factor cylindrical resonant cavity with inner radius of 1.75 cm and inner length of 3 cm, machined out of a Copper piece (*Figure 11*).

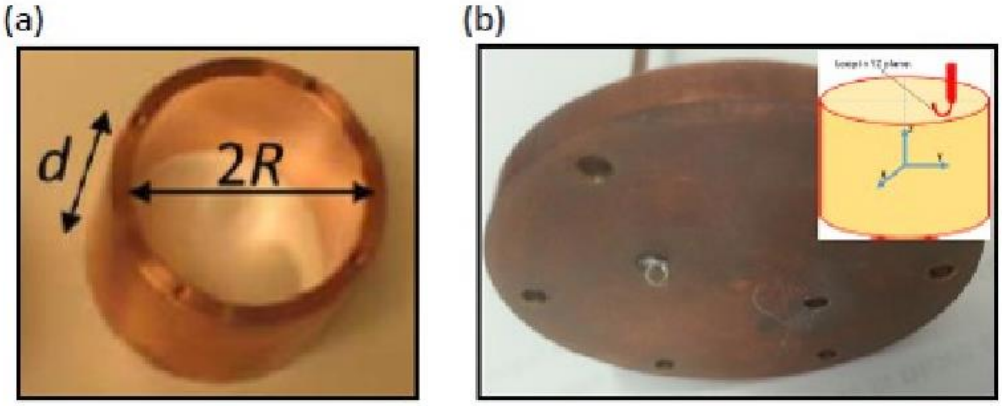

Figure 11: a) Optical image of the copper cavity b) Optical image of the top plate of the cavity. The metallic circular loop is used to couple the microwave radiation from the source to the cavity.

Different Transverse Electric (TE) and Transverse Magnetic (TM) modes can be excited. Each mode has a particular resonance frequency. *Figure 12* identifies specific modes to their

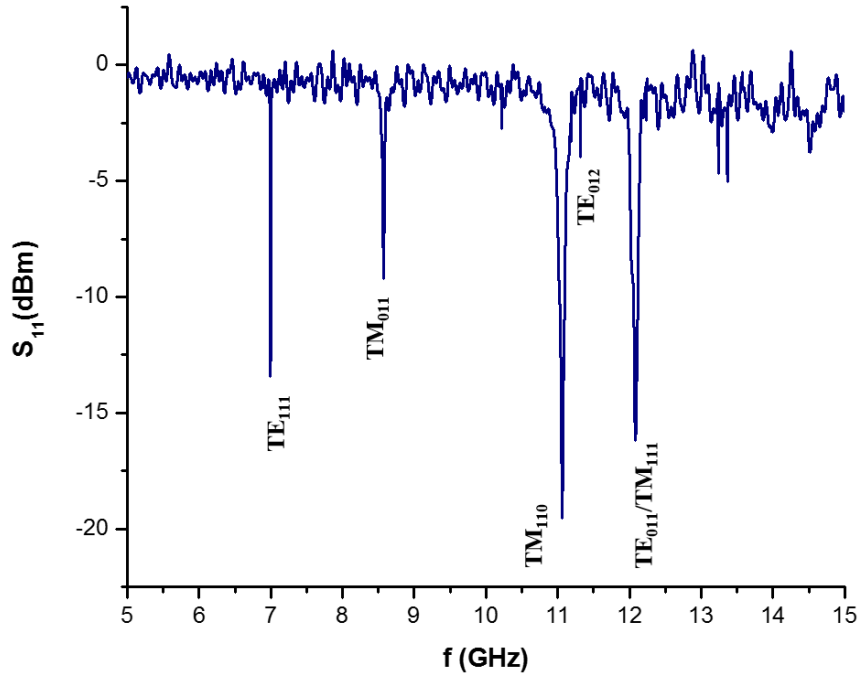

Figure 12: Reflexion spectra of the cavity for frequencies up to 15 GHz. The different TE and TM modes are identified.

resonance frequency.

The ISHE measurements were carried out by tuning the cavity to its TM_{011} mode (8.54 GHz). The sample is placed such that the rf magnetic field is maximum and parallel to the direction of the current generated through the ISHE (*Figures 13a* and *13b)*. This configuration minimizes the electric field components of the oscillating field along the ISHE field direction, avoiding interference with the measurements.

The rf field is then pulse-modulated at a few kHz, and the generated ISHE voltage measured by a lock-in amplifier. The schematic of a typical ISHE measurement is depicted in *Figure 13c*, wherein the precessing magnetization of the Py (about the y-axis) adiabatically pumps a dc component of spin current into the U.

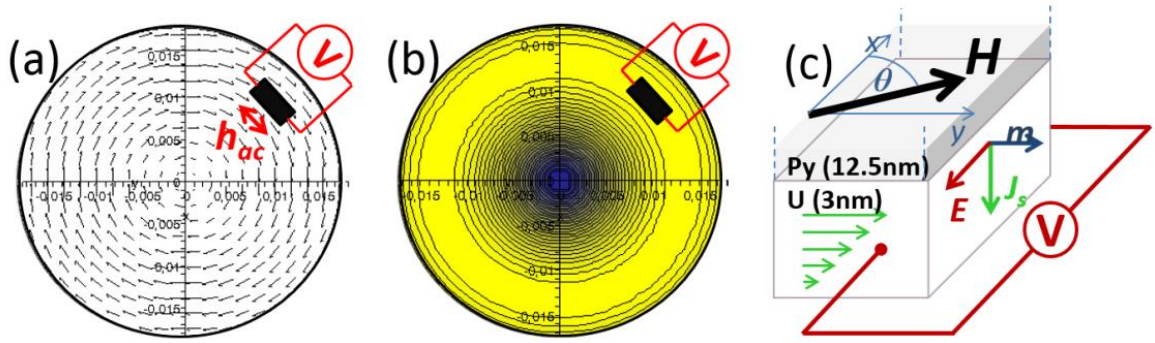

Figure 13: a) Schematics of the direction and magnitude (length) of the microwave magnetic field at the bottom plate of the cavity for the TM $_{001}$ mode. b) Color-coded plot of the magnitude of microwave magnetic field at the bottom plate of the cavity. c) The schematic of ISHE experiment, θ is the angle between the externally applied dc magnetic field and x direction. The spin currents are injected into uranium with polarization along the y-axis. The spin gradient normal to the interface results in electromotive force along the x-axis

2.4.2. Results

The spin current generated from spin pumping (*Equation 1.33*) is converted into an electromotive force through the Inverse Spin Hall effect. The equivalent circuit for the Py/U bilayer is represented in *Figure 14b* and the expression for the originated voltage is [14]:

$$V_{ISHE} = \frac{R_{Py}R_U}{R_{Py}+R_U} I_C = \frac{\frac{w}{lt_{Py}\sigma_{Py}}\frac{w}{lt_U\sigma_U}}{\frac{w}{lt_{Py}\sigma_{Py}}+\frac{w}{lt_U\sigma_U}} I_C = \frac{w}{l}\frac{1}{t_{Py}\sigma_{Py}+t_U\sigma_U} I_C = \frac{wd_U}{t_{Py}\sigma_{Py}+t_U\sigma_U}\langle j_C\rangle \qquad (2.4)$$

where R_{Py} id the resistance of the Py film, R_U is the resistance of the Uranium film, $I_C = ld_U < j_c >$ is the charge current created, σ_{Py} is the conductivity of Py, σ_U is the conductivity of U, t_{Py} is the thickness of Py, t_U is the thickness of U, w is the distance between the contacts and l is the length of the sample (*Figure 14a*).

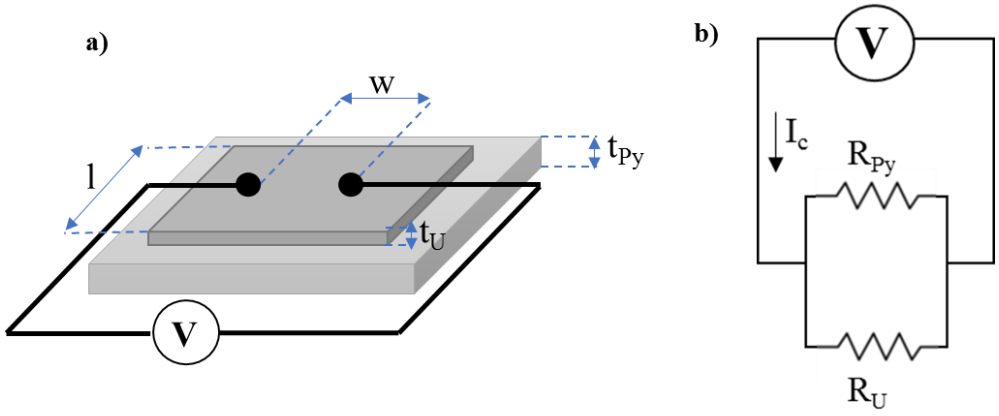

Figure 14: a) Graphical representation of the Py/U sample, where w is the distance between the contacts, l is the length of the sample, t_U is the thickness of Uranium and t_{Py} is the thickness of Permalloy b) Equivalent circuit for the Py/U bilayer.

The spin current density and the charge current density are related by the spin hall angle, θ_H, as follows:

$$\langle j_C \rangle = \theta_H \left(\frac{2e}{\hbar}\right) \langle j_S \rangle \tag{2. 5}$$

$<j_S>$ being the averaged spin current density:

$$\langle j_S \rangle = \frac{1}{t_U} \int_0^{t_U} j_s(x) dx \tag{2. 6}$$

where $j_S(x)$ is given by *Equation 2.19*:

$$\langle j_S \rangle = \frac{1}{t_U} \int_0^{t_U} \frac{\sinh[\frac{x-t_U}{\lambda_{sd}}]}{\sinh(t_U/\lambda_{sd})} j_S^0 dx = \frac{\lambda_{sd}}{t_U} tanh\left(\frac{t_U}{2\lambda_{sd}}\right) j_S^0 \tag{2. 7}$$

Combining *Equations 2.5* and *2.7* and recovering the expression of j_S^0 for thin films with the magnetization parallel to the film (*Equation 1.33*):

$$\langle j_C \rangle = \theta_H \left(\frac{2e}{\hbar}\right) \frac{\lambda_{sd}}{t_U} tanh\left(\frac{t_U}{2\lambda_{sd}}\right) j_S^0 = \theta_H \left(\frac{2e}{\hbar}\right) \frac{\lambda_{sd}}{t_U} tanh\left(\frac{t_U}{2\lambda_{sd}}\right) \frac{g_{eff}^{\uparrow\downarrow} \gamma^2 h^2 \hbar \left[M_S\gamma + \sqrt{(M_S)^2\gamma^2 + 4\omega^2}\right]}{8\pi\alpha^2[(M_S)^2\gamma^2 + 4\omega^2]} \tag{2. 8}$$

Finally, substituting *Equation 2.8* into *Equation 2.4*:

$$V_{ISHE} = \frac{w\, \theta_H \lambda_{SD} tanh\left(\frac{t_U}{2\lambda_{sd}}\right)}{t_{Py}\sigma_{Py} + t_U\sigma_U} \left(\frac{2e}{\hbar}\right) \frac{g_r \gamma^2 h^2 \hbar \left[M_S\gamma + \sqrt{(M_S)^2\gamma^2 + 4\omega^2}\right]}{8\pi\alpha^2[(M_S)^2\gamma^2 + 4\omega^2]} \tag{2. 9}$$

As observed from *Equation 2.9*, the spin Hall angle depends on the magnitude of measured ISHE voltage signal, thus it is necessary to separate the ISHE signal from any other unwanted voltage generation effect. One of the most common alternative voltage contributions can be originated by the anisotropic magnetoresistance (AMR), which is due to a classical induction effect of in-plane oscillating magnetic fields within the film plane [2, 30]. Fortunately, the AMR voltage is antisymmetric around the resonance field [2], contrary to the symmetric nature of the voltage generation expected from the ISHE [2, 22, 23].

Figure 15 shows the measured dc signal corresponding to the FMR resonance of the sample with the dc magnetic field along opposite directions along the y-axis (θ = 90 and -90 degrees). In order to separate the ISHE voltage signal arising from the spin pumping in our experiments, the observed signal (black circles in *Figure 14*) is fitted (solid black line) using a combination of symmetric, $V_S(H)$, and antisymmetric, $V_{AS}(H)$ functions:

$$V(H) = V_S(H) + V_{AS}(H) \tag{2. 10}$$

$$V_S(H) = V_S \frac{\Gamma^2}{(H-H_{res})^2+\Gamma^2} \; ; V_{AS}(H) = V_{AS} \frac{[-2\Gamma(H-H_{res})]}{(H-H_{res})^2+\Gamma^2} \tag{2. 11}$$

where H_{res} is the FMR resonance field and Γ is the resonance width extracted from the FMR measurements.

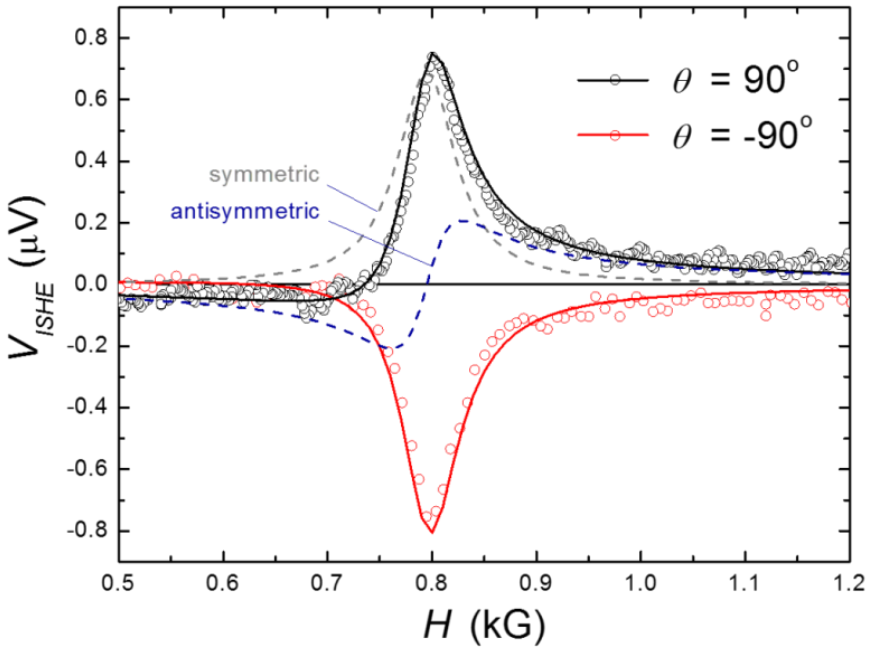

Figure 15: Field dependence of the measured dc voltage in Py/U (circles). The continuous lines are fits to a sum of symmetric and antisymmetric functions (shown for 90 degrees as dashed grey and blue lines, respectively).

The symmetric and antisymmetric contributions to the observed data are shown in *Figure 15* with gray and blue dashed lines, respectively. The pure ISHE voltage originated from the spin pumping mechanism can be extracted from the peak value of the symmetric component at resonance. *Figure 15* also shows the switching of the induced voltage upon reversal of the magnetic field polarity, thus confirming the pumping of spins from the permalloy into the uranium film. Perhaps the most conspicuous feature of these results is that the ISHE voltage signal indicates that the spin Hall angle for U is positive [28].

According to spin pumping theory, the amplitude of the generated spin current depends on the microwave power proportionally to the cone-angle of magnetization precession in the ferromagnet. As expected, the measured ISHE signal increases with microwave power (*Figure 16a)*. The linear behavior of the ISHE voltage with microwave power agrees well with the expectation from spin pumping (*Figure 16b*).

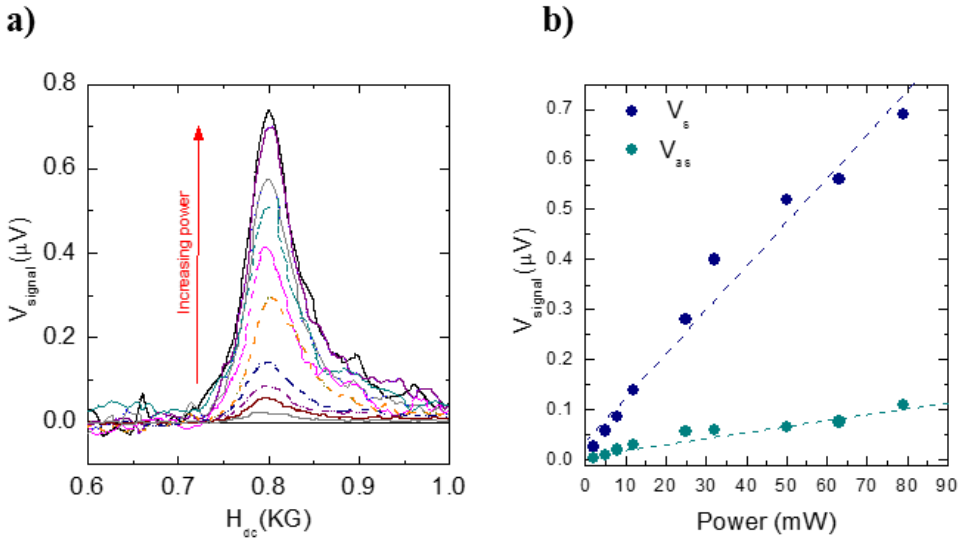

Figure 16: a) Microwave power dependence of inverse spin Hall effect voltage signal in Py/U. The red arrow points to the increasing microwave power direction. b) Voltage amplitude for the symmetric and antisymmetric signals. The symmetric contribution scales linearly with power, confirming the spin pumping origin of the signal.

Finally, in order to quantify the spin-charge current interconversion efficiency in uranium we proceed to calculate the spin Hall angle from *Equation 2.9*. The values for the different parameters are shown in *Table 2*.

Table 2: Values of the different parameters used to calculate the spin hall angle from Equation 3.9, where h is the magnitude of the ac magnetic field and λ_{SD} the spin diffusion length of Uranium.

σ_U	3.5×10^{6} $(\Omega m)^{-1}$
σ_{Py}	1.5×10^{6} $(\Omega m)^{-1}$
t_U	3×10^{-9} m
t_{Py}	12.5×10^{-9} m
w	1×10^{-3} m
M_S	0.95 T
γ	2.06
h	0.86×10^{-4} T
g_r	2.28×10^{19} m^{-2}
V_{ISHE}	0.76×10^{-6} V
λ_{SD}	3×10^{-9} m

Since no data is available for the spin diffusion length in uranium, we have used $\lambda_{SD} = 3$ nm (a value within the range of those found in Pt), noting that the obtained result from *Equation 2.9* would not change much for $\lambda_{SD} > 3$ nm. In addition, we note that the Nb capping layer may contribute to the ISHE signal if not all spins are diffused within the 3nm-thick U layer, which will ultimately depend on the spin diffusion length of uranium. Due to the negative spin Hall angle for Nb (-0.0087) [22], the small fraction of spin current interconverted to electric current in the Nb film would decrease the signal obtained from U, and lead to an underestimation of the spin Hall angle of the latter, although this effect is expected to be minimal for a 3 nm-thick U film, since most spins would be absorbed before reaching the Nb layer.

With the values given in *Table 2* we find the spin Hall angle in uranium to be θ_H = 0.004(0.4%) [28]. Where if we were to use the spin mixing conductance estimated relative to isolated Py, θ_H would be about 30% lower, with all else constant. Surprisingly for such a high atomic number material, this value is lower than that of Pt, the most common system explored for spin pumping/ISHE experiments and for which there is still debate and different values ranging from 0.006 to 0.4 have been reported in the literature [2, 30-32].

2.5. Conclusions

According to the rule of thumb that the spin-orbit interaction is proportional to the atomic number, platinum (Z = 78) should present a lower spin-charge interconversion efficiency than uranium. This is contrary to our observations, which points to alternative explanations for the origin of spin-orbit coupling in metallic systems. Following those same lines, Du *et al*. have recently reported a comprehensive study of spin pumping at FM/NM interfaces using several transition metals [16]. They found that the spin Hall angle in some of these elements is comparable to that found in substantially heavier metals (*e.g.*, Pt), and that its value and sign do not follow a proportional law with the atomic weight within the studied series of elements. Indeed, the authors find the spin Hall angle sign to oscillate within the series, being maximum for Cr (θ_H = -0.05) and Ni (θ_H = 0.05), and associate this behavior to a dominant role of the *d*-electron configuration in the spin Hall effect in 3*d* elements. More specifically, these authors find that the effects of atomic number and *d*-orbital filling are additive. For example, for elements with filled electronic orbitals, such as in the Cu, Au, Ag series, the atomic number is the most relevant parameter governing spin-orbit coupling because of their zero orbital moment [15, 16,

24], while for transition metals with partially filled *d*-orbitals, the orbital moment contribution is dominant [15, 16, 24]. It is likely that the same construction applies to Lanthanides (4*f*) and Actinides (5*f* metals), and that the *f*-orbital filling in elements of these series may govern the spin Hall conductivities.

Our results clearly show there is novelty in the *f*-electron systems: aside from the moderate magnitude of the spin-Hall angle in uranium, its positive sign is incommensurate with results of transition metals. Since its electronic configuration ([Rn]$5f^3 6d^1 7s^2$) has less than half filling of both the *d* and *f* orbitals, one would have expected a negative spin Hall angle, as is observed in transition metals. Perhaps, the strong spin-orbit coupling in lanthanides and actinides mixes the spin and orbital Hall effects in the same way that it makes only the total angular momentum, $J = S+L$, to be a good quantum number, and one should start thinking about the total angular momentum Hall effect (JHE) to understand spintronics effects in *f*-electron systems. A comprehensive study involving more elements on these series would be necessary to completely understand the underlying physics behind the spin and orbital Hall effects in heavy metals.

CHAPTER 3:
DYNAMICAL SPIN INJECTION IN GRAPHENE

3.1. Introduction

Commonly, the studies of dynamical spin pumping on FM/NM interfaces use a heavy element as the NM layer [2, 16, 27], since heavy metals present efficient spin current to charge current interconversion, as reported in Chapter 2. Nonetheless, in the past few years, a great deal of effort has been made towards exploring the possibilities of carbon-based materials, such as organic semiconductors [33, 34], carbon nanotubes [35], and graphene [36], for novel spintronics applications. Graphene, in particular, is a very promising spin channel material owing to high electron mobility [37], gate-tunable charge carrier density, and room-temperature long spin-diffusion length [38]. Above all mentioned advantages, the possibility of enhancing spin-orbit coupling in graphene, by either doping [39,40] or by the proximity effect [41,42], is the most promising one, as it facilitates the electrical manipulation of spin currents in 2D systems.

Although spin pumping at FM/Graphene (FM/Gr) interfaces has already been demonstrated [18, 19, 42-46], the real nature of spin pumping and the spin relaxation processes in graphene are still poorly understood. Along those lines, J. B. S. Mendes *et al.* [45] and S. Dushenko *et al.* [46] reported measurements of spin current to charge current interconversion generated in FM/Gr devices, offering conflicting interpretations (*Figure 17a* and *17b*). On one hand, Mendes and collaborators associated the results to the inverse Rashba-Edelstein effect, and noted that the effect could not be ascribed to the ISHE due to the geometrical disposition of the experiment (see *Figure 17b*). On the other hand, S. Dushenko *et al.* conducted the same

experiment with the capability of gating, and observed that the amplitude of the signal was independent of the gating voltage far away from the Dirac point. The absence of gate dependence made them conclude that the effect could not be associated to the Rashba-Edelstein effect, since the latter depends on the Fermi velocity of the carriers, which would be modified by an electric field in graphene. Therefore, the detected signal had to be originated from the ISHE. However, they did not provide with a clear explanation of the impossibility to obtain an ISHE signal in the plane of the device, since it violates the required symmetry, i.e., that the spin polarization, spin current and induced ISHE electric field must be orthogonal to each other ($E_{ISHE} \propto \theta_H J_S \times \sigma$). For this, the spin current should flow into the graphene layer perpendicularly to the FM/graphene interface, which obviously not possible given the real bidimensionality of single-layer graphene.

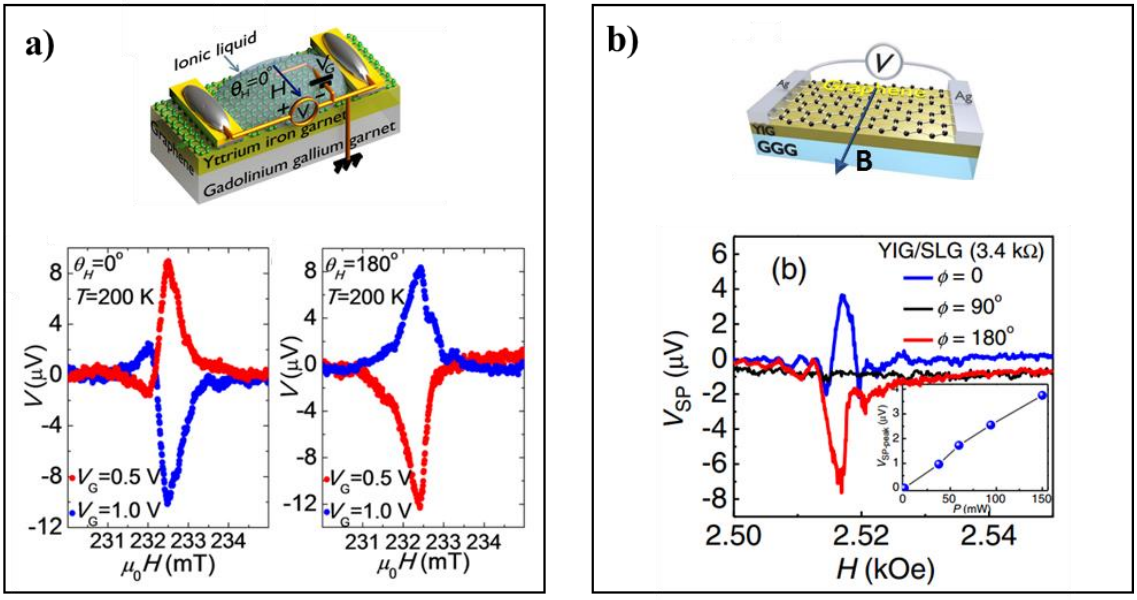

Figure 17: a) Results obtained by M. Shirashi *et al.* with a schematic of the sample configuration. Figures adapted from [46] b) Voltage signal measured in an in-plane configuration by J. B. S. Mendes *et al.* The inset shows linear dependence of the voltage amplitude versus the microwave power. Figures adapted from [45].

The goal of the experiment proposed in the present chapter is to better comprehend the processes involved in dynamical spin injection in FM/graphene interfaces.

3.2. Set-up and Sample Preparation

Damping studies performed in Py/Gr bilayers by our group [19], show an enhancement of the Gilbert damping parameter in the Py/Gr sample only when graphene is protruding away from a ferromagnetic strip (*Figure 18)*. The indicated enhancement can only be associated with the loss of spin angular momentum of the Py as taken away by the graphene areas away from the ferromagnet (*i.e.*, spin pumping). Hence, the report proves that when graphene is under the ferromagnet no additional damping is observed. This is likely due a strong hybridization between the ferromagnet and the graphene, and/or because all the spins pumped into graphene flow back into the ferromagnet, as there is no possibility for the spins to decay, since the whole area underneath is homogenously excited. Therefore, if one is to measure the ISHE in graphene, the contacts of such device should be placed on a strip of graphene protruding away from the ferromagnet and the external magnetic field should be applied perpendicular to the plane.

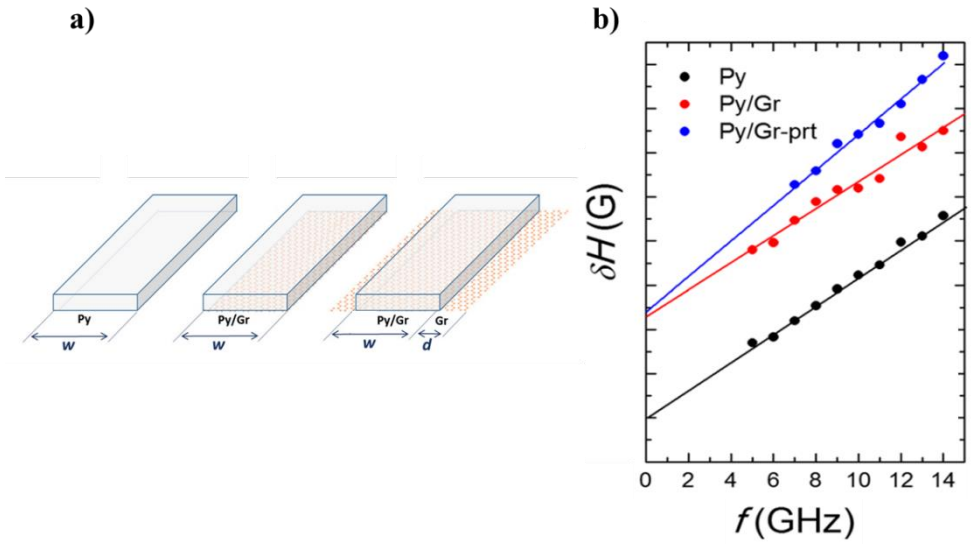

Figure 18: a) Sketches illustrating the strips used in the experiment [19] b) Out-of-plane frequency dependences of the FMR linewidth of the three strips measured by S. Simran *et al.* [19].

The proposed device schematics is illustrated in *Figure 19*. Following the design, when the magnetization of the ferromagnet is directed perpendicular to the plane of the device (z-axis), its precession will generate spin current in graphene with spins polarized in the z direction. The spins will then decay away from the ferromagnet, in opposite directions for each of the strips, along x-axis as seen from the figure. Considering that $E_{ISHE} \propto \theta_H J_S \times \sigma$, the ISHE voltage will be generated along the y-axis.

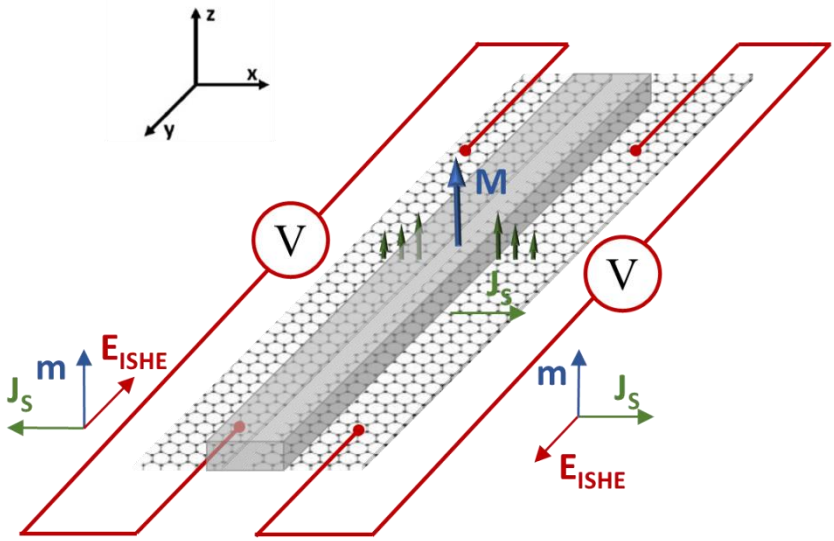

Figure 19: Schematic of the proposed device configuration. Two independent graphene strips protrude away from the ferromagnet, the spins are pumped into graphene and decay along the x-direction. Note that the spin current has opposite directions for the different strips. The electric field can be measured along the y direction by inducing the ferromagnet FMR out of the plane of the film (z-axis).

It should be pointed out, that metallic ferromagnets cannot be used in this experiment, since they would shunt the ISHE signal considering the large resistance of the single layer graphene strips. To avoid this, a ferromagnetic insulator, Yttrium Iron Garnet (YIG), will be employed instead of Permalloy.

3.2.1. ISHE device fabrication

After a sample of a YIG patterned bar (25µm x 1mm x 25nm) is provided by our collaborators at Argonne National Lab (Axel Hoffman's group), a single layer CVD graphene sheet is transferred onto the substrate. Developing a good transfer process is imperative, since a continuous sheet of graphene is crucial for dynamical spin injection measurements (see *Appendix A* for graphene transfer recipe).

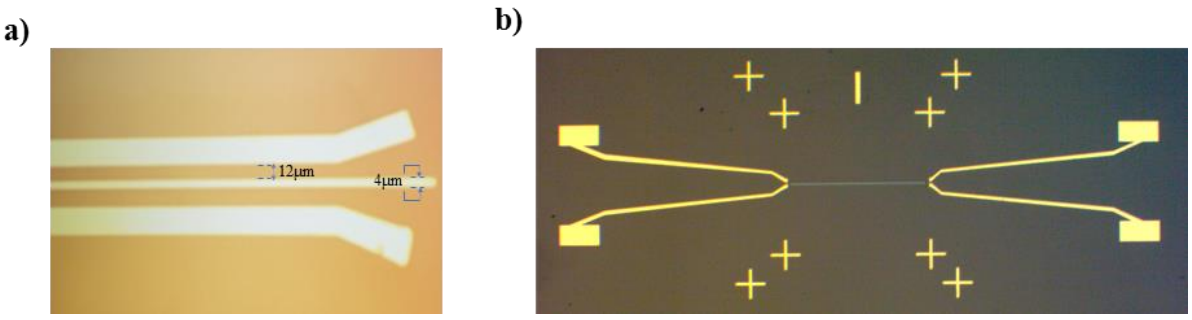

Figure 20: a) Optical microscope image of the homemade mask used for graphene etching. b) Optical image of the device after the evaporation of the Ti/Au contacts.

The graphene sheet is then etched into two 1mm long and 15µm wide strips, separated 4µm using a homemade optical lithography mask (*Figure 20a*). Following the etching of graphene, Ti/Au electrodes are patterned on top of the protruding ends of graphene (*Figure 20b*). Before proceeding to the next step, the device is characterized with a probe station to confirm there is contact between the two ends of each graphene strip. If the probe station characterization shows kΩ resistance on both strips, a layer of 200nm of SiO_2 is e-beam evaporated only on the central part of the sample using a shadow mask to avoid liftoff issues. The SiO_2 layer will insulate the YIG/Gr structure from the CPW central line that will lay on top and at the same time will act as a dielectric for the gate. Finally, the last step is to pattern the

CPW on top, followed by an e-beam evaporation of Ti/Cu/Au (10nm/250nm/10nm). *Figure 21* is an illustration of the patterned device.

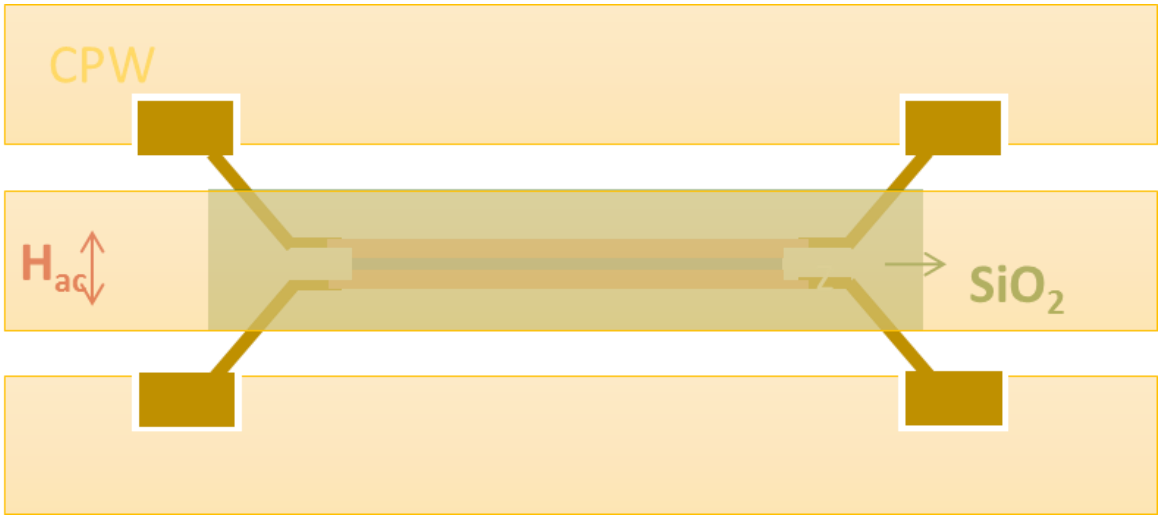

Figure 21: Illustration of the patterned graphene ISHE device. The YIG/Gr bilayer is underneath 200nm of SiO_2. H_{ac} shows the direction of the ac magnetic field.

3.2.2. Experimental set-up

As seen in Chapter 2, the ISHE signal is linearly dependent on the microwave power. With the purpose of improving the transmission over the device, a CPW circuit board was developed as a replacement for the housing box set-up. The CPW circuit board contains a cavity in the center, where the patterned sample will be placed. The connections from the sample to the CPW circuit board are done through a wire bonder. The developed set-up consists of a commercially available R04000 Rogers Corporation circuit board machined in the machine shop. In *Figure 22*, an optical image of a sample mounted on the circuit board CPW exemplifies the assembly.

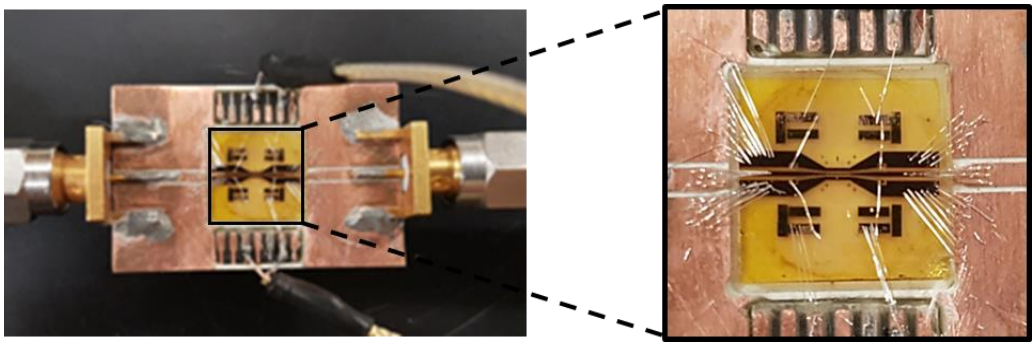

Figure 22: Picture of a ISHE device wire-bonded into the developed CPW circuit board. The inset is a zoom on the sample.

A comparison between the transmissions of a sample mounted in the traditional housing box and a sample wire bonded to the CPW circuit board can be seen in *Figure 23*. The transmission through the sample in the new set-up has been improved by ~4dB.

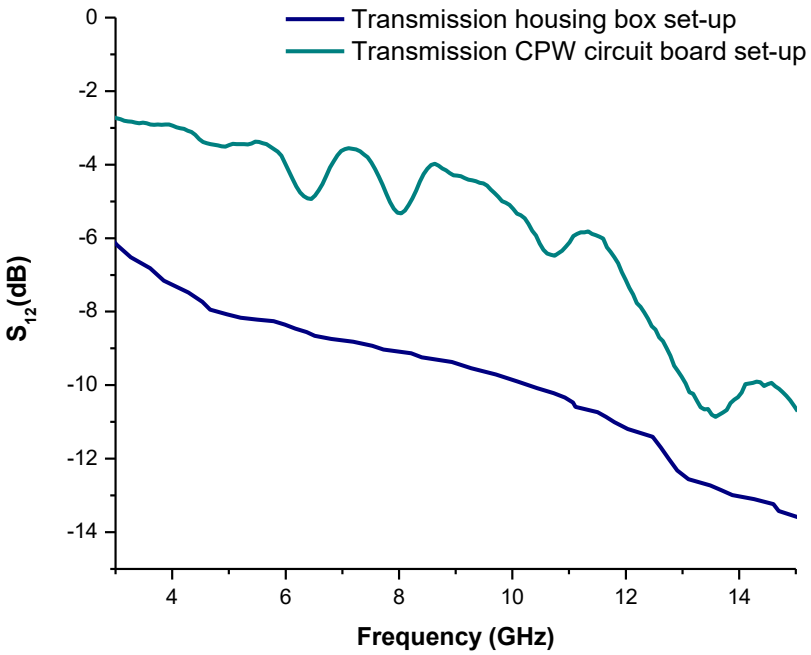

Figure 23**: Comparison between the transmission of the sample when wire bonded into the circuit board and the transmission of the sample when placed in the housing box.**

Once the sample is wire bonded to the circuit board and mounted on the probe it is ready to measure. A schematic of the circuits used to measure the ISHE voltage is shown in *Figure 24a and 24b*. The expected amplitude of the ISHE voltage signal is in the order of microvolts, therefore a lock-in detection technique will be used. To measure the signal generated by the microwaves with a Lock-in amplifier, the microwave source (PNA or HP source-meter) must be pulsed with a duty cycle controlled by the lock-in amplifier. Both an Agilent vector network analyzer (PNA) and a HP microwave synthesizer have been used as microwave sources for these experiments. To pulse the signal in these two different sources, different approaches had to be followed. The HP synthesizer output can be directly pulsed, whereas for pulsing the PNA an external microwave switch must be employed (*Figure 24a* and *24b* illustrate the two variations).

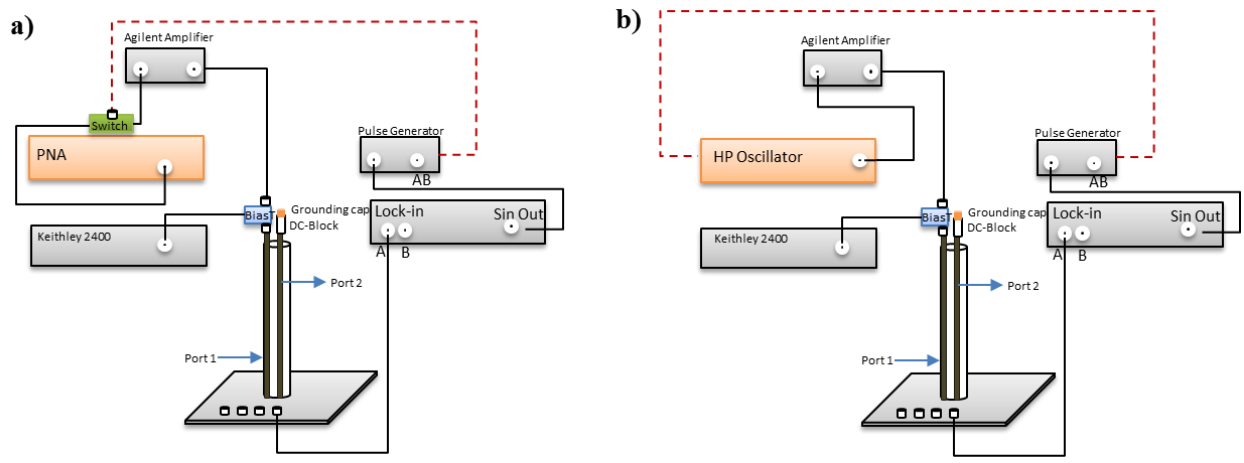

Figure 24: Schematic of all the elements used for the ISHE instrumentation set-up. a) when the source-meter used is the PNA. b) when the HP Sweep Oscillator is the microwave source.

In order to gate using the central line of the CPW, the dc voltage is superimposed to the microwave signal by means of a bias-tee on port 1. The dc voltage is sourced by a Keithley 2400. The second port should be grounded for ac signal but floating for dc voltage. To achieve that, a DC-Block is placed before the grounding cap in Port 2.

3.3. Results

Graphene characterization is done by measuring the strip resistance while sweeping the dc voltage (gate) applied to the central line of the CPW (see *Figure 24* for instrumentation set-up). The gate dependence of one of the graphene strips is shown in *Figure 25*. Notice that graphene is slightly p-doped, since the Dirac point (highest resistance value) is positively shifted from zero gate voltage. This value has to be kept in mind as the ISHE voltage is going to be zero at the charge neutrality point [46].

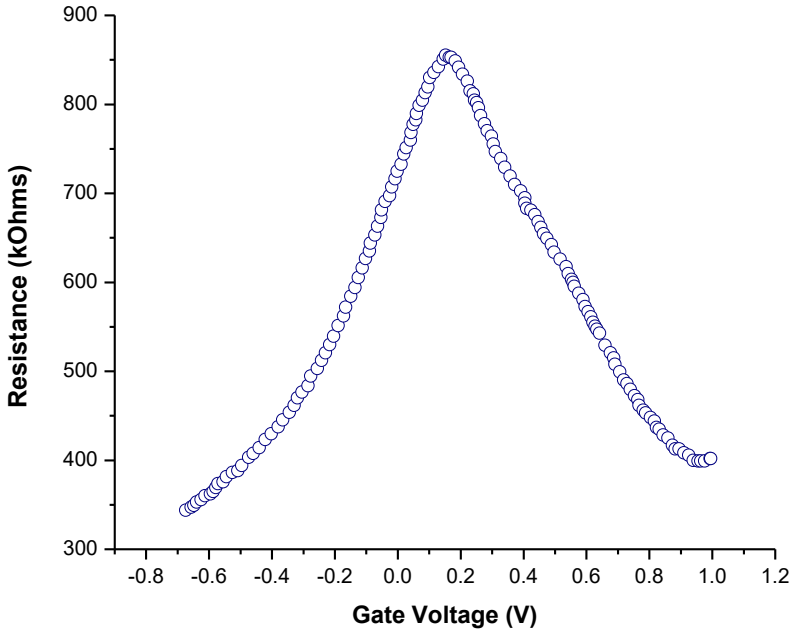

Figure 25: Resistance in kOhms versus Gate voltage for one of the graphene strips. The charge neutrality point is situated at 0.2 V.

Before attempting to measure the ISHE voltage, the FMR response should be studied. After all, V_{ISHE} will be generated only during the resonance condition of the ferromagnet. The experimental set-up used for the FMR measurements is very similar to the one explained in

Chapter 2, with the only difference being that the sample is now imbedded in the CPW. *Figure 26* displays the FMR signals obtained at seven different frequencies. The advantage of using a CPW versus a resonant cavity is that there is no limitation in the number of frequencies one can study.

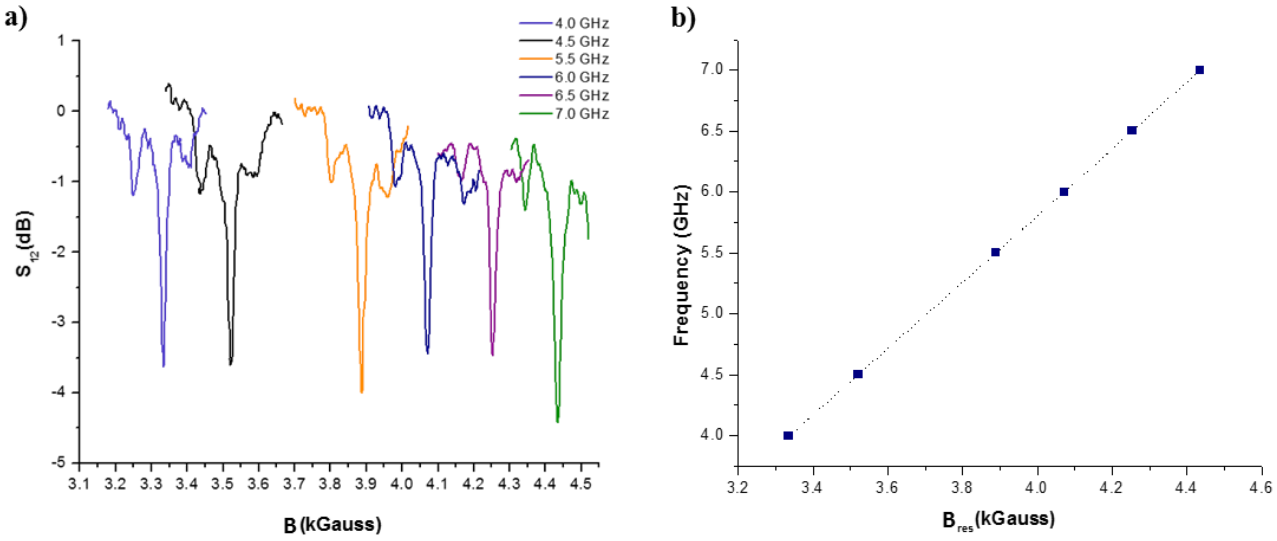

Figure 26: a) Transmission versus out of plane Magnetic Field showing the Ferromagnetic Resonance of YIG for: 4GHz, 4.5 GHz, 5.5 GHz, 6GHz, 6.5GHz and 7GHZ. b) Frequency versus on resonance out of plane magnetic field.

Figure 27b shows the measured voltage when a 7GHz microwave signal is sent to the sample. The magnetic field sweeping values were determined from the FMR signal (*Figure 27a*). The amplitude of the signal is in the mV range and the noise observed is ±20uV, larger than the expected signal (≈2uV) [45, 46]. The mV range signal is due to the coupling between the substrate (GGG) and graphene. To uncouple the substrate from our sample a thicker layer of YIG is needed.

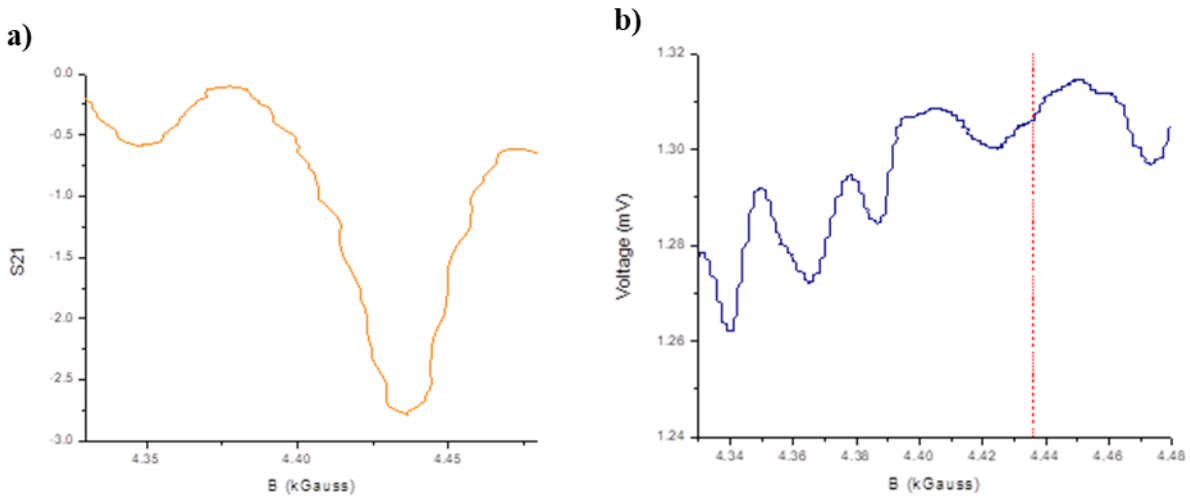

Figure 27: a) Transmission versus magnetic field at 7GHz (FMR). b) Voltage versus magnetic field at 7GHz. The red dashed line marks the position where the signal should have been.

The next step is to measure the same set of experiments with a sample containing a μm thick YIG.

CHAPTER 4:
ELECTRICAL TUNNELING TRANSPORT SPECTROSCOPY

4.1. Introduction

A different approach on utilizing graphene is to take advantage of its electronic and structural properties. The trend towards achieving smaller electronic devices is driving electronics to its ultimate molecular-scale limit [47]. Following this tendency, in the past decade, molecules have been functionalized to act as diodes [48], switches [49], transistors [50] and sensors [51], among others. Different experimental methods can be employed to characterize single-molecules, such as, scanning tunneling microscopy (STM) [52] and single-electron transistors (SETs) [50]. Up to date, gold is the favored material electrode used in both techniques because of its noble character. However, the fact that it has a very high atomic mobility makes the junction stable only at low temperatures [53]. Graphene, on the other hand, has a higher structural stability, given its covalent-bond structure, even at high temperatures. Moreover, it will reduce the size mismatch with the molecule, as most of the functionalized molecules mentioned above are organic [53, 54]. The following chapters will deepen on the use of graphene as an electrode for: Single-electron transistors (SETs) (Chapter 6) and scanning tunneling microscopy (STM) (Chapter 7), while Chapter 5 reports on the characterization of a molecular double quantum dot on gold-based SETs. The aim of the current chapter is to provide with the necessary concepts for the second part of this thesis.

4.2. Single-Molecule Spectroscopy Techniques

In electron transport measurements, the system under study is contacted by two electrodes. These electrodes connect the object of study with the external circuitry in order to measure its conductance. In principle, it is a very simple set-up. Still, only after STM and SETs were developed could single-molecule measurements be performed [48].

4.2.1. Scanning tunneling microscopy

Three decades ago, Binning and Rohrer developed the first STM [55]. Since then, the technique has advanced into being able to atomically resolve a range of structural, vibrational, magnetic, and spectroscopic properties of the system under study [56].

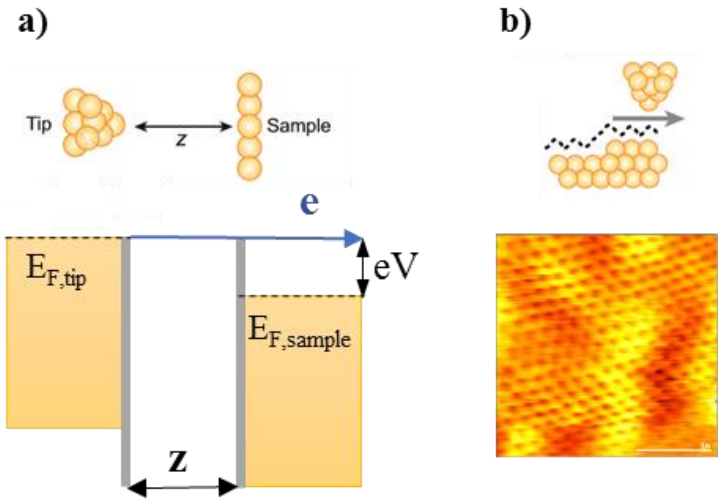

Figure 28: a) Energy diagram of the tip and the sample, where *z* is the distance between them, $E_{F,tip}$ is the Fermi level of the tip and $E_{F,sample}$ is the Fermi level of the sample, *eV* is the offset between $E_{F,tip}$ and $E_{F,sample}$. b) Illustration of the tip displacement in constant current mode. STM image of graphene taken in constant current mode of one of our devices. Figure a) adapted from reference [55].

On STM measurements, a bias voltage is applied between a sharp conducting metal tip, often tungsten or a platinum/iridium alloy, and a conducting or semiconducting sample. The tip, by means of piezoelectric materials that control with precision its position and movement, is able

to scan the surface of the sample at a very short distance (~3–10 ˚A) [57]. A schematic of the STM operation is represented in *Figure 28*. *Figure 28a* shows an energy diagram of the tip and the sample. The respective Fermi levels are offset by *e* times the applied bias voltage, where *e* is the electron charge. When the STM is set to constant tunneling current mode at a constant bias voltage, it can image the local density of states of the conducting surface with atomic-scale resolution (*Figure 28b*).

4.2.2. Single-electron transport spectroscopy

SETs are three-terminal devices consisting of two conducting electrodes (source and drain) bridging in between the quantum dot (QD) or molecule, similarly to an STM but with a fixed distance between the electrodes, and a third electrode (gate) electrically isolated from the previous ones (see *Figure 29*). It is the presence of the third electrode that allows SETs to shift the electrostatic potential of the QD with respect to the leads, revealing additional information about the molecule, for instance, the presence of vibrational modes and excited states and effects such as Franck–Condon blockade and superconductivity [54, 58].

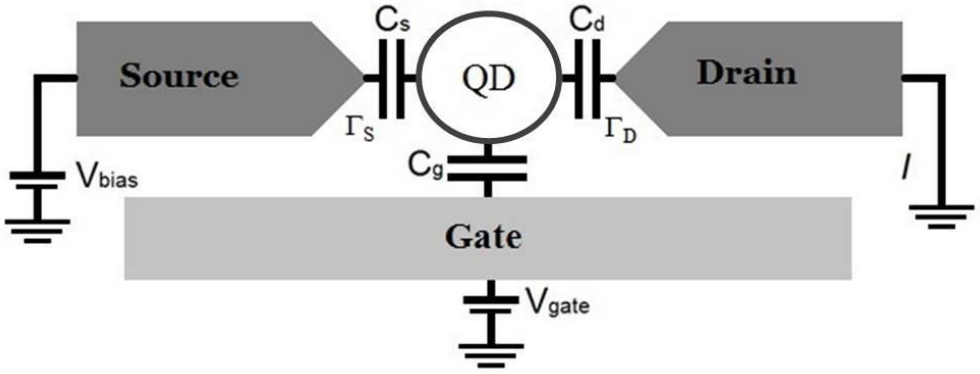

Figure 29: Schematic illustration of a SET. When a bias voltage is applied between source and drain, the electrons tunnel from the source to the quantum dot (QD), with a tunneling rate of Γ_S, and again to the drain (Γ_D). Voltage is applied to the gate electrode, also capacitively coupled to the QD.

The molecule is capacitively coupled to the three electrodes by three different capacitances: *Cs*, *Cd* and *Cg* (*Figure 28*). These capacitances depend on how strongly coupled is the molecule to each of the electrodes. From the single-electron transport spectroscopy is possible to experimentally find the value of these capacitances. *Figure 30* depicts a typical SET spectroscopy contour plot. The slopes of *Figure 30b* are related to the capacitance in the following manner [58]:

$$V = -\frac{C_G}{C_S}(V_G - V_C), \;\; \mu_{N+1} = \mu_D \tag{4. 1}$$

$$V = \frac{C_G}{C_G + C_D}(V_G - V_C), \;\; \mu_{N+1} = \mu_S \tag{4. 2}$$

where V_G is the gate voltage, V_C is the charge degeneracy point (voltage gate value for zero bias), μ_{N+1} is the chemical potential of the molecular level and μ_D and μ_S are the chemical potentials of the drain and source respectively.

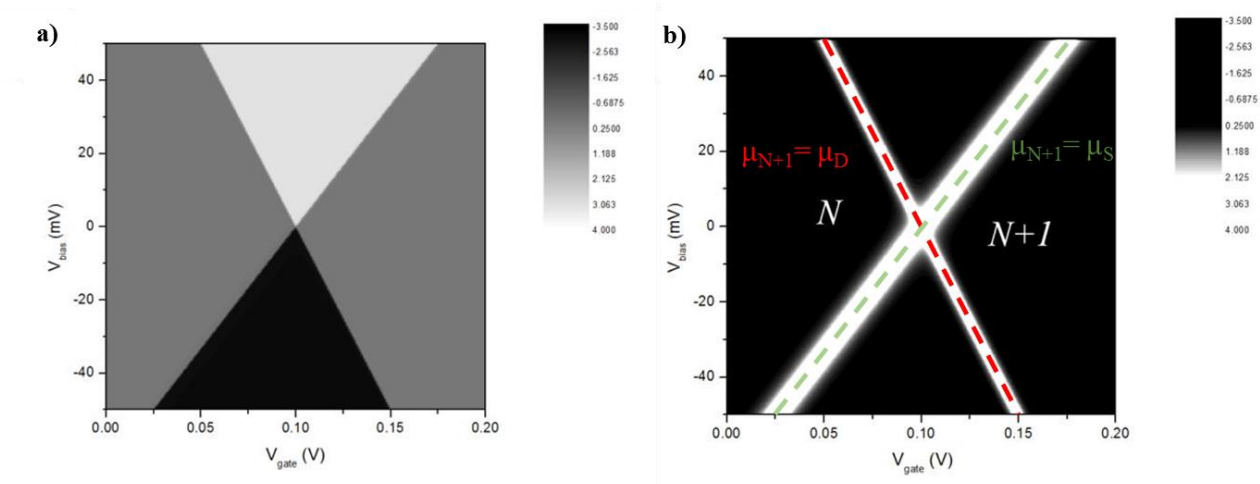

Figure 30: a) Tridimensional contour plot of a molecule in a single-electron transistor, where V_{gate} is in the x axis, V_{bias} in the y axis and the current (I) in the z axis. b) Derivative of the 3D contour plot, in this graph the z axis represents the conductance of the molecule and N and N+1 are, respectively, the neutral and charged states of the molecule. Figures based on reference [56]

The ratio between the gate capacitance and the total capacitance of the system is going to give us the total gate efficiency, β:

$$\beta = \frac{C_G}{C_S + C_T + C_G} \tag{4. 3}$$

4.3. The Coulomb Blockade Theory

The coulomb blockade theory described in this section is based on the review article by Mickael L. Perrin *et al*. [54].

Charge transport through single-molecules follows the laws of quantum mechanics, which means, that electrons are only allowed to populate discrete energy states. Pauli exclusion states that each orbital can only be occupied by two electrons. Therefore, transport will only occur in unoccupied molecular orbitals. The unoccupied orbital with the lowest energy is referred to as LUMO (*i.e.* lowest unoccupied molecular orbital), and the fully occupied molecular orbital with the highest energy is the HOMO (*i.e.* highest occupied molecular orbital). The difference between the LUMO and the HOMO is the HOMO-LUMO gap.

An illustration of the energy diagram of a molecular junction is represented in *Figure 31*. The energy difference between two consecutive charge states of the molecule (μ_N and μ_{N+1}) is called transport gap. The transport gap consists of the HOMO-LUMO gap (level splitting of the molecule, ΔE) plus electrostatic contributions (E_C), such as, charging energy, image correction, etc.

$$E_c + \Delta E = \mu_{N+1} - \mu_N \tag{4. 4}$$

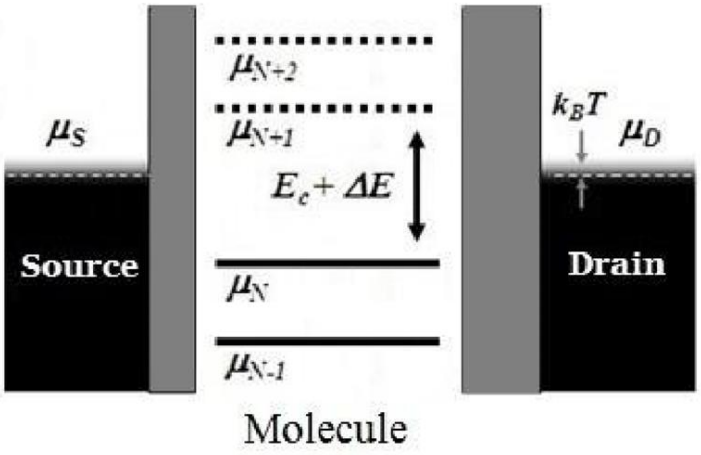

Figure 31: Energy diagram of a molecular junction in equilibrium. The diagram shows a molecule separated from the source and drain electrodes (black) by tunneling barriers (grey). The molecule energy is described by discrete levels μ_N, where the occupied states are represented with solid lines and the unoccupied states with dashed lines. μ_S is the chemical potential of the source, μ_D the chemical potential of the drain, μ_N the chemical potential of the molecule and N is the number of electrons in the molecule.

The presence of the electrodes affects the conduction through the molecule, acting as electron reservoirs with a chemical potential that depends on temperature according to the Fermi distribution of the electronic occupation in the leads:

$$f_{S,D}(E) = \frac{1}{1+e^{\left(\frac{\varepsilon-\mu_{S,D}}{k_BT}\right)}} \tag{4. 5}$$

where S is the source, D is the drain, T the temperature and ε the energy of the electrons.

In equilibrium, we encounter the situation illustrated in *Figure 31*, where the chemical potentials of both electrodes are equal and no current flows through the system. For current to flow there must be an imbalance, which can be achieved by applying a bias voltage. For instance, if a bias voltage is applied to the source electrode its chemical potential will shift as follows:

$$\mu_S = \varepsilon_F + eV, \qquad \mu_D = \varepsilon_F \tag{4. 6}$$

where ε_F is the Fermi energy.

The difference between the chemical potentials of source and drain is the bias window. Only when a molecular level lies in between the bias window will current flow, otherwise transport will be blocked (*i.e.* coulomb blockade regime). If the system is in the coulomb blockade regime (*Figure 32a*) the bias voltage can be increased until the bias window reaches a molecular level (*Figure 32b*).

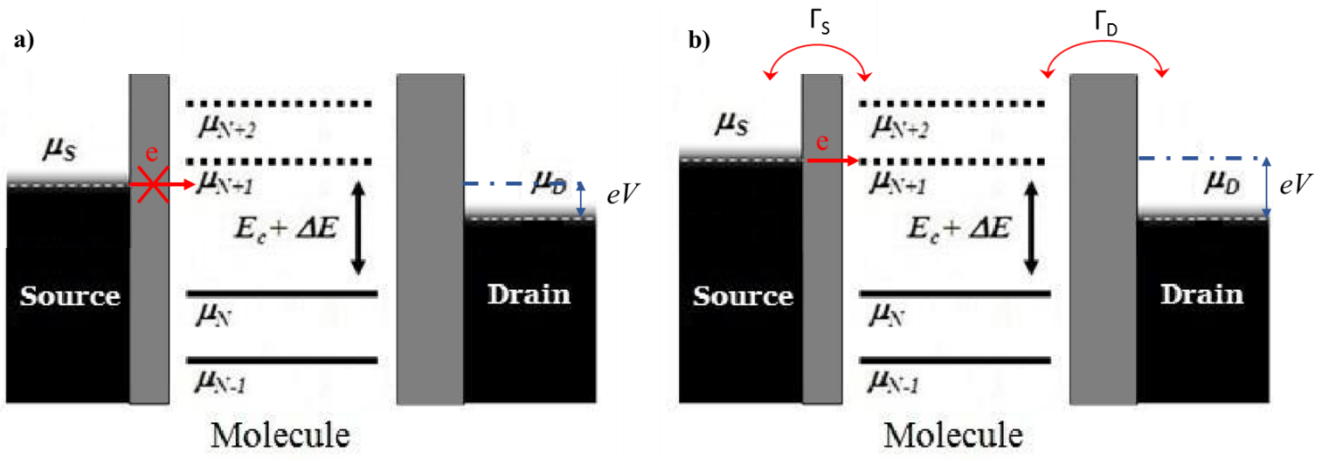

Figure 32: a) Energy diagram of a molecular junction when a bias voltage is applied to the source electrode. The bias voltage generates an imbalance between the chemical potentials of source and drain but no molecular level is present in the bias window and transport is suppressed (Coulomb blockade regime). b) In this situation, a larger bias voltage has been applied such that the source chemical potential reaches the LUMO level of the molecule. Now electrons can tunnel from the source to the molecule and from the molecule to the drain. Γ_S is the electron transfer rate from the source to the molecule and Γ_D is the transfer rate from the molecule to the drain.

The current is determined by the transfer rates, Γ_S and Γ_D, which are related to the coupling between the respective electrodes and the molecule and define the broadening of the energy levels of the molecule. Depending on the ratio of Γ, the confinement energy (Δ), the charging energy (E_C), and k_BT, we can distinguish three different transport regimes: weak coupling regime ($\Gamma << \Delta$, E_C, k_BT), intermediate coupling regime ($\Gamma \approx \Delta$, E_C, k_BT) and strong

coupling regime ($\Gamma > \Delta$, E_C, k_BT). I am only going to focus on the intermediate coupling regime, since is the one dominating transport in the molecular junctions presented in this Thesis.

In the intermediate coupling regime, the molecules are covalently bonded to the electrodes, thus, the level broadening of the molecule must be considered. In small molecules, transport is governed by the molecular level closest to the Fermi energy of the electrodes (*Figure 32a*), hence we can approximate that only one molecular level participates in the conduction (single-level model). Taking that into account, the density of states of the molecule has the following expression:

$$D(\varepsilon) = \frac{4\Gamma_S\Gamma_D}{[\varepsilon-\varepsilon_0]^2+[\Gamma_S+\Gamma_D]^2} \quad (4.\ 7)$$

where ε_0 is the energy difference between the molecular level and the Fermi energy of the electrodes. Due to the hybridization between the electrodes and the molecule, the density of states becomes a Lorentzian instead of a Dirac delta function.

Using the Landauer-Buttiker formalism [59] one can obtain the total current through the molecule:

$$I = \frac{e}{\hbar}\int \frac{dE}{2\pi} T(\varepsilon)[f_S(\varepsilon) - f_D(\varepsilon)] \quad (4.\ 8)$$

where f_S and f_D are the fermi distribution of the leads and $T(\varepsilon)$ is the transmission through the molecule given by:

$$T(\varepsilon) = Tr\left\{\frac{\Gamma_S(\varepsilon)\Gamma_D(\varepsilon)}{\Gamma_S(\varepsilon)+\Gamma_D(\varepsilon)}[G - G^\dagger]\right\} \quad (4.\ 9)$$

G(ε) being the retarded Green's function:

$$G(\varepsilon) = \frac{1}{(\varepsilon S - H - \Sigma_S - \Sigma_D)} \tag{4. 10}$$

here, *H* is the Hamiltonian of the molecule, *S* is the symmetric overlap matrix and $\Sigma = \Lambda(\varepsilon) + i\Gamma(\varepsilon)$ describes the molecule-electrode interaction and Λ(ε) accounts for the level shift because of the hybridization of the molecular orbitals with leads [54]. Due to the uniform density of states of gold near the Fermi energy, we will neglect Λ(ε) and take Γ(ε) to be independent of the energy.

Combining *Equations 4.9* and *4.10* into *Equation 4.8* and considering the low-temperature limit, we find a final expression for the current:

$$I(V) = \frac{4G_0}{e}\frac{\Gamma_S\Gamma_D}{\Gamma_S+\Gamma_D}\left[arctan\left(\frac{\varepsilon_0+\frac{eV}{2}}{\Gamma_S+\Gamma_D}\right) - arctan\left(\frac{\varepsilon_0-\frac{eV}{2}}{\Gamma_S+\Gamma_D}\right)\right] \tag{4. 11}$$

CHAPTER 5:
ELECTRICAL CHARACTERIZATION OF SINGLE S-DPA-C-Fc-C_2-S MOLECULES

5.1. Introduction

In solid state junctions, where an individual molecule or a self-assembled monolayer (SAM) of molecules is contacted to electrodes, charge transport is governed by both the characteristic time that the electron spends in the molecule while tunneling from one electrode to another, described by the Landauer formalism explained in Chapter 4, and the characteristic interaction time resulting from the available degrees of freedom for the charge to sample the molecule, which follows the Marcus theory [60]. For example, for junctions with long molecular wires, or readily accessible degrees of freedom, one would expect long interaction times, leading to a complete charge relaxation in the molecule [60]. Indeed, transition from coherent tunneling to thermally activated charge transport as a function of molecular length has been demonstrated [61-64], but several groups reported unexplained activationless charge transport for junctions where the charge carriers almost certainly interact strongly with the (bio)molecule over large distances of even more than 10 nm [65-67].

Recently, Migliore and collaborators [68] combined the Marcus and Landauer theories to describe charge transport across molecular junctions, suggesting that internal electrostatic gating could push the junction into the inverted Marcus region resulting in activationless charge transport, which could explain anomalous temperature-dependent charge transport. This chapter reports experimental data showing that it is possible to do so with a new molecular diode,

composed of a ferrocene (Fc) head group connected to a conjugated backbone via a $(CH_2)_n$ tether.

5.2. Single-electron Transistors Measurements

To obtain direct evidence of intramolecular orbital gating, we performed charge transport measurements on individual S- DPA-C-Fc-C_2-S molecules by means of single molecule transistor at low temperatures (T = 4K).

5.2.1. SETs Fabrication

The transistors were fabricated via optical and electron-beam lithography. Optical lithography is used for the first three metal layers that will configure the basis of the circuit and the gate electrode. Whereas, the gold nanowires that will form the source and drain electrodes are patterned by means of e-beam lithography. *Figure 33* shows an optical image of the first three metal layers of the transistor.

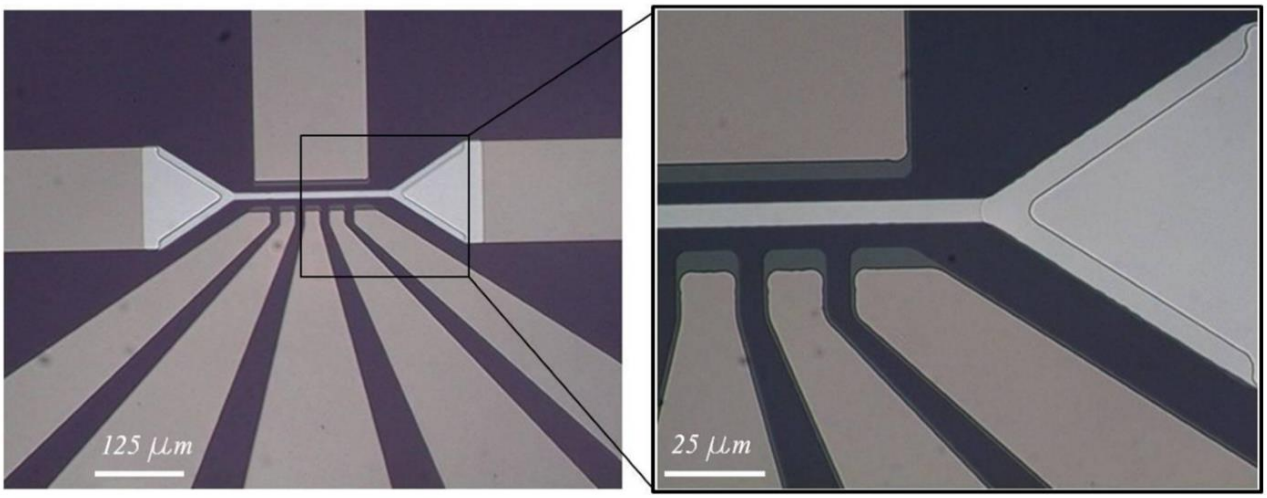

Figure 33: Optical images of the three first layers deposited. The first layer (dark green) consists on 5nm of Ti and 15nm of Pd, the gate (grey) is deposited on top (35nm of Al). Finally, 10nm of Ti and 70nm of Pd are deposited (light brown). The image on the right is a closer look of the area in the rectangle.

After the nanowires have been deposited, a nanometer sized gap must be created. In order to achieve that, we use an electromigration-induced breaking procedure at room temperature. During electromigration, gold atoms move due to the momentum transfer of the conducting electrons. This happens when the maximum current density is reached (j_b ~5×1012A/m^2). The process is controlled by a Labview program that monitors the current through the nanowire while slowly increasing the bias voltage. Once the current value drops, the bias voltage is recoiled back and the process is repeated until the current reaches a value close to the universal single-channel conductance (R = 25.8 kΩ) (*Figure 34a*).

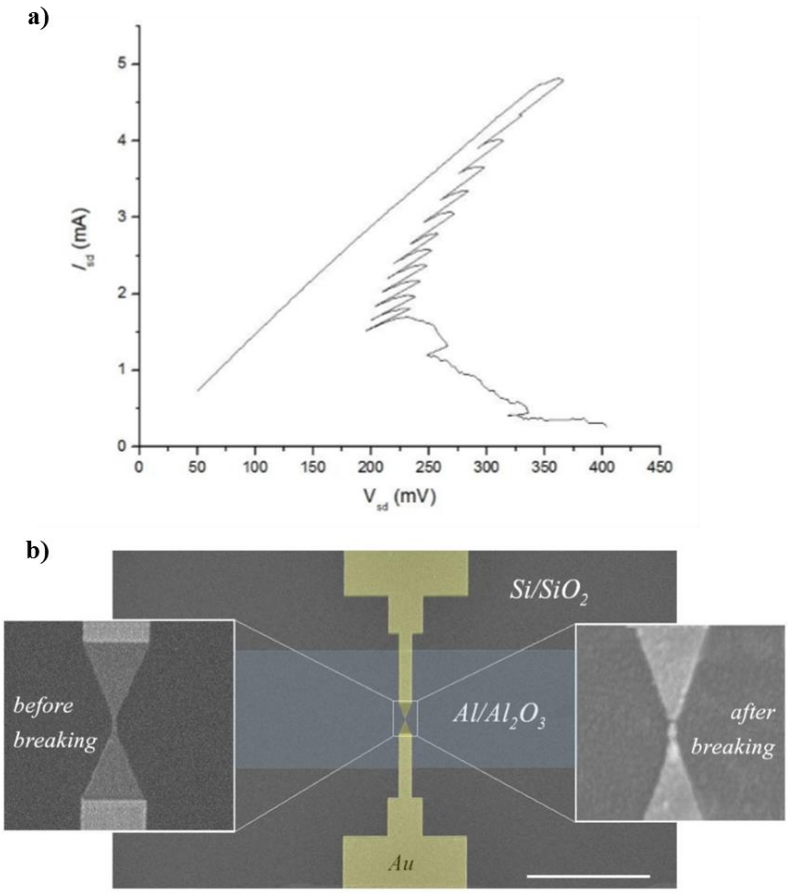

Figure 34: a) I-V graph of the feedback-controlled electromigration-induced breaking process at room temperature. The process is stopped when the resistance through the nanowire approaches 25.8kΩ (38.7μS). b) Scanning electron microscopy (SEM) image of a gold nanowire on top of the Al/Al2O3 back gate. The insets show the narrowing part of nanowire before (left) and after (right) breaking. Scale bar is 10μm.

The nanowires are then left untouched for two hours, time during which the gold atoms will reorganize and create a nanogap separating the source and drain leads due to surface tension. Finally, the transistor is characterized by measuring its I-V curve, which should show tunneling current if the gap is properly formed (*Figure 35*).

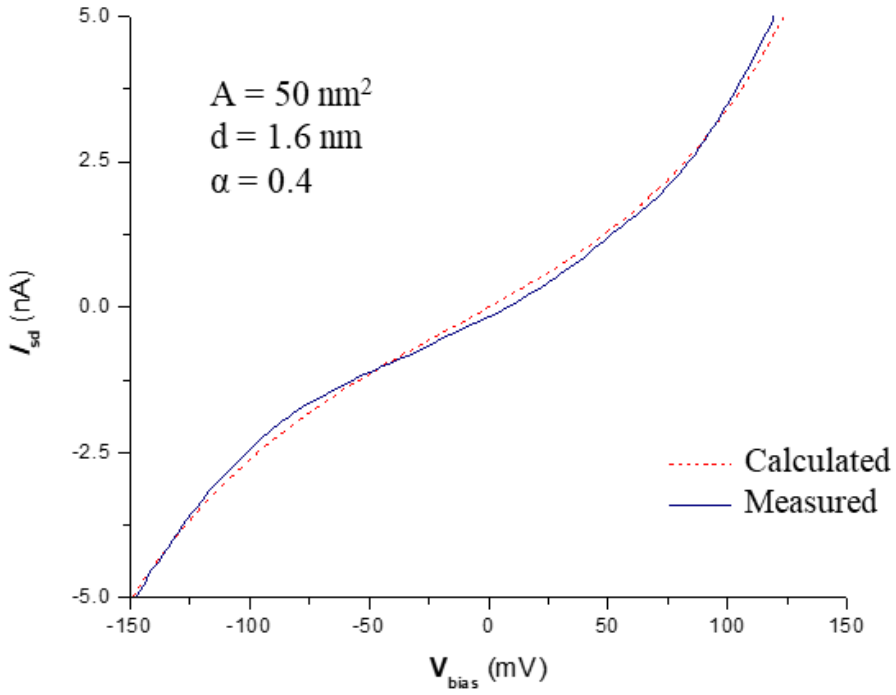

Figure 35: I-V tunneling curve of a nanowire 2h after the electromigration-induced process. In blue the measured value, in red the fitting using the Simmons model for a gap of 1.6nm. For more information about the model see section 6.3.1.

This technique allows the generation of a controlled nanometer-sized gap at room temperature. The molecules are consequently deposited after the electromigration-induced process, avoiding possible damage in their structure. It also prevents the formation of gold nano-islands that could mask their behavior as molecules [58].

5.2.2. SETs results

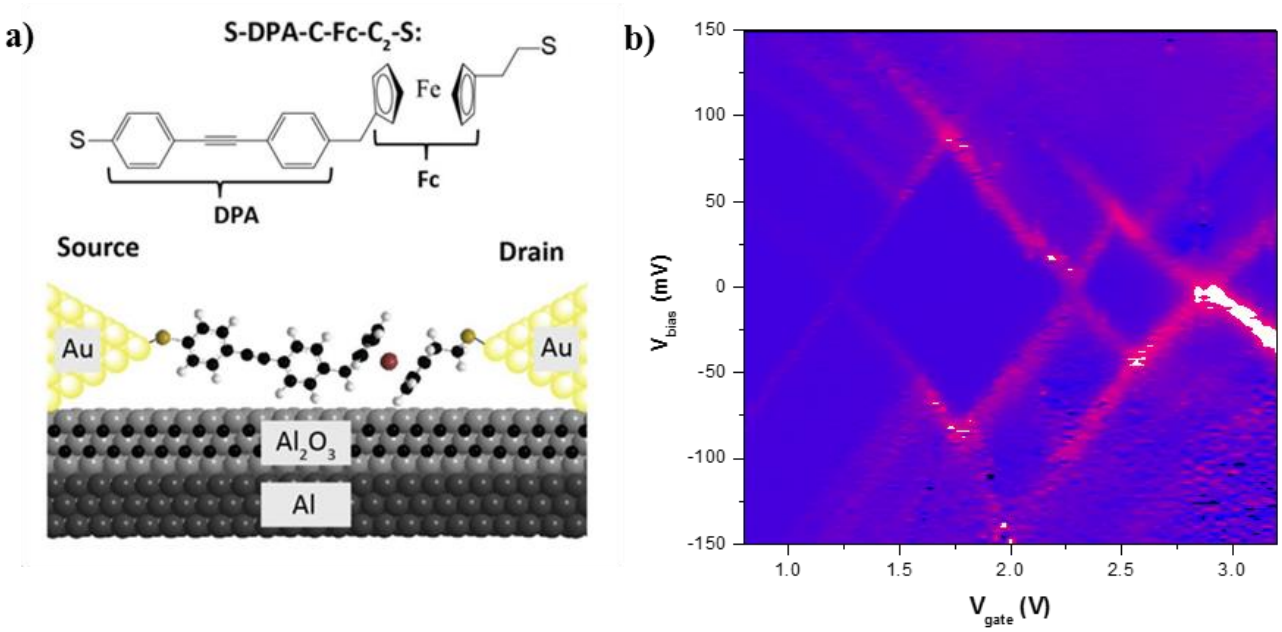

Figure 36: a) Schematic illustration of the single molecule transistor with S- DPA-C-Fc-C$_2$-S. b) Experimental differential conductance stability diagram of a S-DPA-C-Fc-C$_2$-S based SET at *T* = 4 K.

Figure 36b shows the differential conductance as a function of bias and gate voltage. The excitation lines are associated with crossings of molecular orbitals with either the Fermi-level of the source or drain electrodes, and with both at the same time for zero bias, *i.e.*, the charge degeneracy points at 1.23, 2.29, and 2.85 V.

The transport stability diagram resembles that of a double quantum dot where the charge on one dot affects the energy states of the other, and *vice versa*, and which had only been reported before in solid state systems [69], metallic nanoparticles [70], and carbon nanotubes [71], thus constituting the first realization of a molecular double quantum dot. Here, the Fc and the DPA units serve as "quantum dots" separated by a tunneling barrier defined by the number n of connecting -CH$_2$- groups.

DFT calculations of Au-S-DPA-C-Fc-C_2-S-Au show that the HOMO is almost completely localized on the ferrocene and the LUMO on the DPA unit (*Figure 37a*). *Figure 37a* also shows the corresponding energy level diagram with the energy levels localized on the Fc (m) and DPA (p) isolated from each other, and *Figure 37b* shows the equivalent model circuit. Each molecular unit is capacitively coupled to the leads and to each other, with a parallel combination of a resistor and a capacitor, and to a gate.

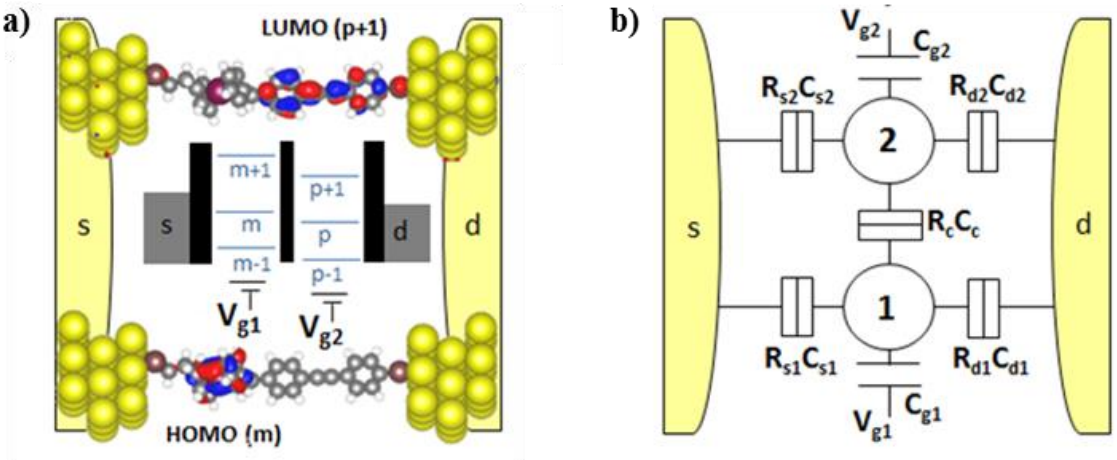

Figure 37: a) Energy level diagram of the molecular SET with the corresponding energetics associated with a double quantum dot picture. The electronic configurations of the HOMO and LUMO levels have been calculated by DFT for the molecule in between gold electrodes. b) Equivalent circuit of the molecular SET in terms of a double quantum dot system.

A commercially available single electron tunnel device and circuit simulator (SIMON) was used for our calculations. To fit our experimental data, we used two energy levels for DPA, with $E_m = 70$ meV and $E_{m+1} = 119$ meV, with level broadenings $\Gamma_m = 0.98$ meV and $\Gamma_m = 2.23$ meV (yellow lines in *Figure 37 a-b*). We used one level for dot Fc, with $E_p = 135$ meV and $\Gamma_p = 2.5$ meV (red lines in *Figure 37 a-b*).

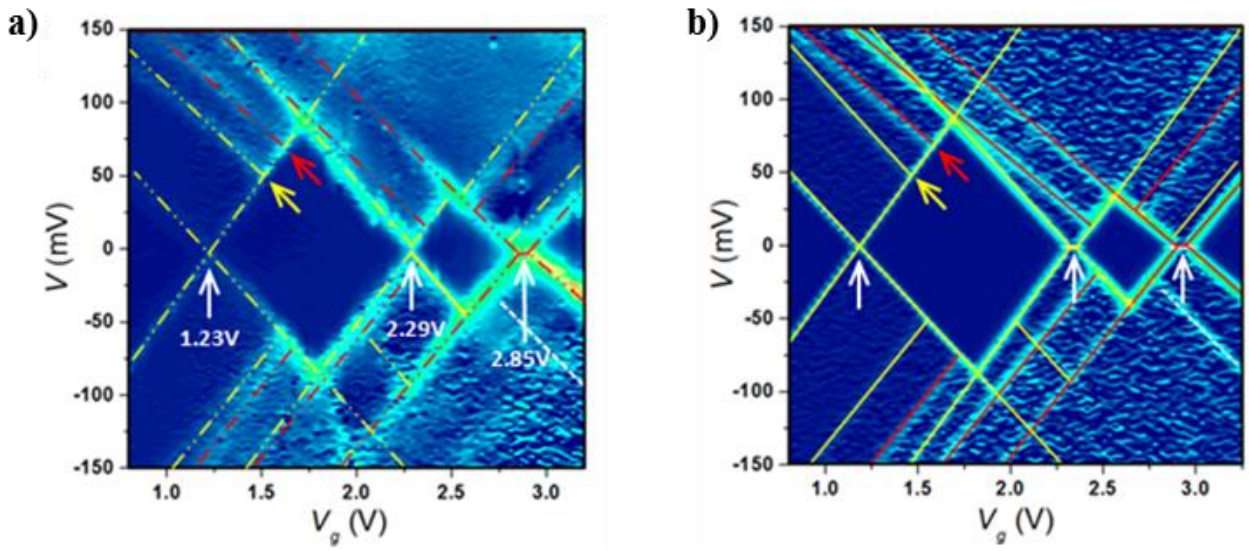

Figure 38: a) Experimental differential conductance stability diagram of a S-DPA-C-Fc-C_2-S based SET at T = 4 K. The lines represent excitations of molecular levels in a double quantum dot representation, with two levels in dot 1 (yellow lines) and one level in dot 2 (red lines). b) The fitting results calculated with $R_{s1(2)}$ = 115(50) kΩ, $C_{s1(2)}$ = 0.99(2.40)×10^{-18} F, $R_{d1(2)}$ = 130(95) kΩ, $C_{d1(2)}$ = 8.9(11.0)×10^{-19} F, $C_{g1(2)}$ = 2.2(1.7)×10^{-19} F, and R_c = 80 kΩ, C_c = 4.57×10^{-18} F.

The model reproduces remarkably well the Coulomb blockage areas defined by the crossings at zero bias of the main excitations (charge degeneracy points), as well as energy splittings in transport excitations that arise directly from the inter-dot coupling. This coupling between the two molecular components can be understood as an effective gating of one molecular unit by the other, *i.e.*, molecular orbital gating. The corresponding coupling potential is given by:

$$V_c = e\frac{C_c}{C_1C_2 - C_c^2} \tag{5. 1}$$

with the charging potential for each unit given by:

$$V_1 = e\frac{C_2}{C_1C_2 - C_c^2}, \text{ and } V_2 = e\frac{C_1}{C_1C_2 - C_c^2}, \tag{5. 2}$$

where *e* is the electron charge, and $C_{1(2)}$ is the sum of the capacitances attached to dot 1(2) [69]. This coupling is responsible for the splittings of the transport excitations observed in *Figure 3*8 *a-b* (yellow and red arrows).

Figure 39 a and *b* show the calculated near-zero-bias differential conductance without and with intermolecular gating, respectively. When the molecular units are uncoupled, gating the energy levels of one unit does not affect the other, while the opposite is true when the Fc and DPA units are coupled resulting in a complex differential conductance stability diagram. In our devices, the Fc and DPA units are both coupled to the same gate electrode and therefore both levels move diagonally across the diagram shown in *Figure 39b*. Here, the red arrow represents the gate potential sweep in *Figures 38 a-b* (V_g = 0.5-3.5 V) crossing excitations separating each charge state at the charge degeneracy points (white arrows in *Figures 38a*, *b* and *Figure 39b*).

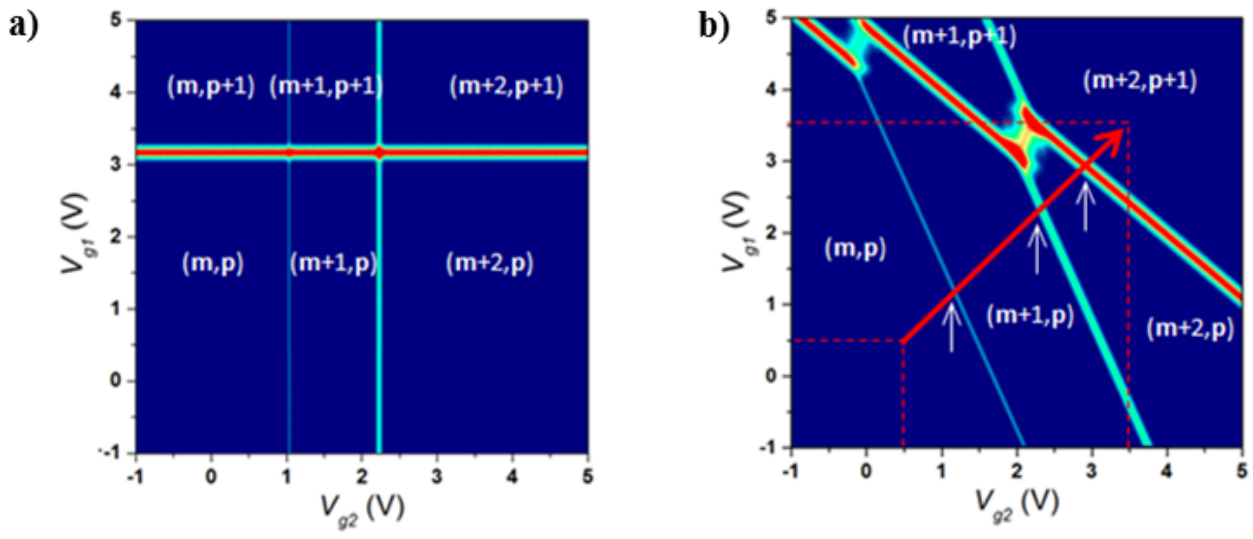

Figure 39: Calculated stability diagrams at low bias (1 mV) as a function of individual gating of each dot without (a) and with (b) inter-dot coupling, respectively. The red arrow represents the single gate voltage sweep in the experiments ($V_g = V_{g1} = V_{g2}$), in correspondence with data in Figure 36.

5.3. Self-Assembled Monolayer Measurements

The work detailed in this section was performed by our collaborators in Singapore.

5.3.1. SAMs characterization

HS-C-DPA-C_n-Fc with n = 0, 1, 2, or 3 derivatives were synthesized and their corresponding SAMs on template-stripped gold (Au^{TS}) surface formed. The value of n determines the coupling between the conjugated backbone of the molecule and the Fc unit. *Figure 40* shows the chemical structure of the molecules. The structure of SAMs was characterized by cyclic voltammetry.

Figure 40: Illustration of the SAM-based junction with the chemical structure of the S-C-DPA-C_n-Fc (n = 0, 1, 2, 3).

The surface coverage was obtained by integration of the oxidation wave. *Figure 41b* shows that the surface coverage is 4.31×10^{-10} mol/cm^2 for n = 3 but the surface coverage decreases with decreasing n. SAM (d_{SAM}) thickness was determined by angle resolved X-ray photoemission spectroscopy (ARXPS) and the molecular length (l) by gas phase density

functional theory (DFT). From these data, we conclude that the SAMs are standing up right and are densely packed, with well-controlled supramolecular structures.

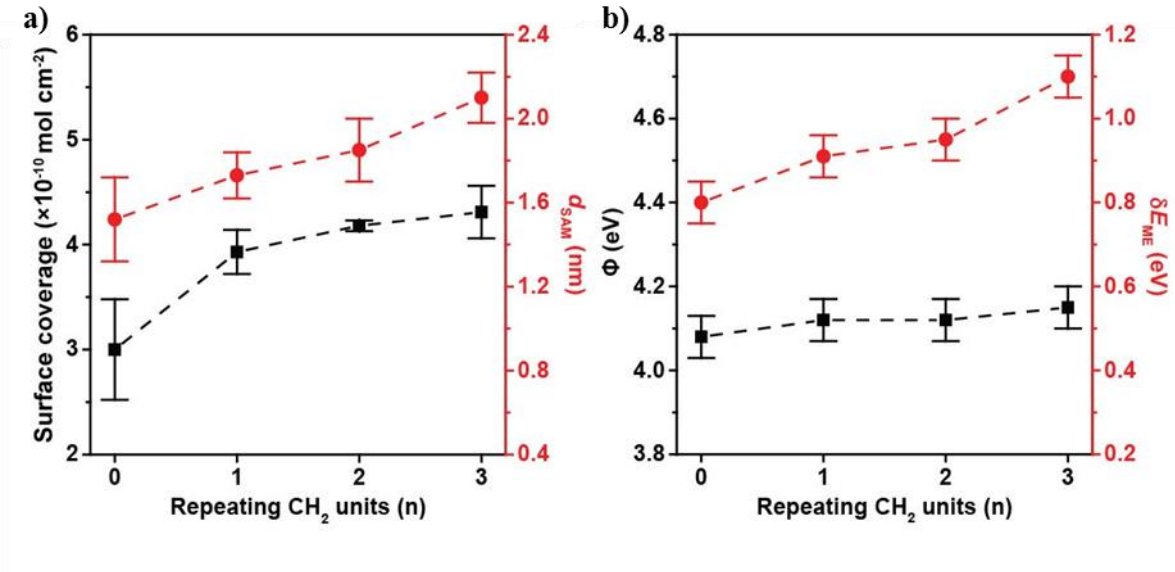

Figure 41: a) The surface coverage determined from the cyclic voltammograms (black squares) and the SAM thickness determined by the ARXPS (red dots). b) The work function (Φ) and HOMO-onset (δE_{ME}) determined by UPS.

To obtain more information regarding the electronic structure of the SAMs, the work function of the SAM-modified bottom-electrode Φ_n and the off-set in energy between the energy of the HOMO, E_{HOMO}, and the Fermi level $\delta E_{ME,n}$ ($=E_{HOMO} - E_F$) were determined from the UPS data. From n = 3 to 0, the values of Φ_n decrease slightly by 0.07 eV due to the well-known "push-back" effects consistent with the small decrease in the surface coverage. The increase of $\delta E_{ME,n}$ as a function of n by 0.30 eV, indicates the decrease of delocalization of the HOMO centered on the Fc unit over the DPA backbone in agreement with DFT calculations. The position of the LUMO levels were estimated using near edge X-ray adsorption fine structure

spectroscopy (NEXAFS). These data were used to construct the energy level diagrams and as a reference for the modelling outlined below.

5.3.2. SAMs results

The SAMs on Au were contacted with EGaIn (eutectic alloy of 75.5% Ga and 24.5% In by weight) top-electrodes. *Figure 41 (a-d)* shows the average J(V,T) traces measured from 240 to 330 K at intervals of 10 K for n = 0, 1, 2 and 3. From the temperature dependence measurements, it is possible to obtain the activation energy (E_a), which relates to thermal excitations of molecular vibrational modes and reorganization of neighboring solvent molecules [72], using the Arrhenius law:

$$I = I_0 e^{-\frac{E_a}{k_B T}} \tag{5. 3}$$

where I_0 is a pre-exponential factor. The Arrhenius plots for n = 0, 1, 2 and 3 and voltages from -0.4V to -1V and from 0.4V to 1V are represented in *Figure 42 (e-l).*

The following information can be extracted from *Figure 42*. i) The rectification ratio R = |J(-1.0V)|/J(+1.0V) decreases from 74 to 23 when n decreases from 3 to 1, but increases again to 71 for n = 0. ii) The mechanism of charge transport is thermally activated at negative bias for junctions with n = 1-3, however, it is activationless for n = 0 (the J(V) characteristics of all junctions are independent of T at positive bias). iii) The value of the activation energy increases with decreasing n from 3 to 1 from 68±8, 1.8×10^2±23 to 2.1×10^2±28 meV (error is one standard deviation from three different devices). iv) The value of E_a increases with applied bias above a threshold value of -0.40 V below which the J(V) curves are independent of T.

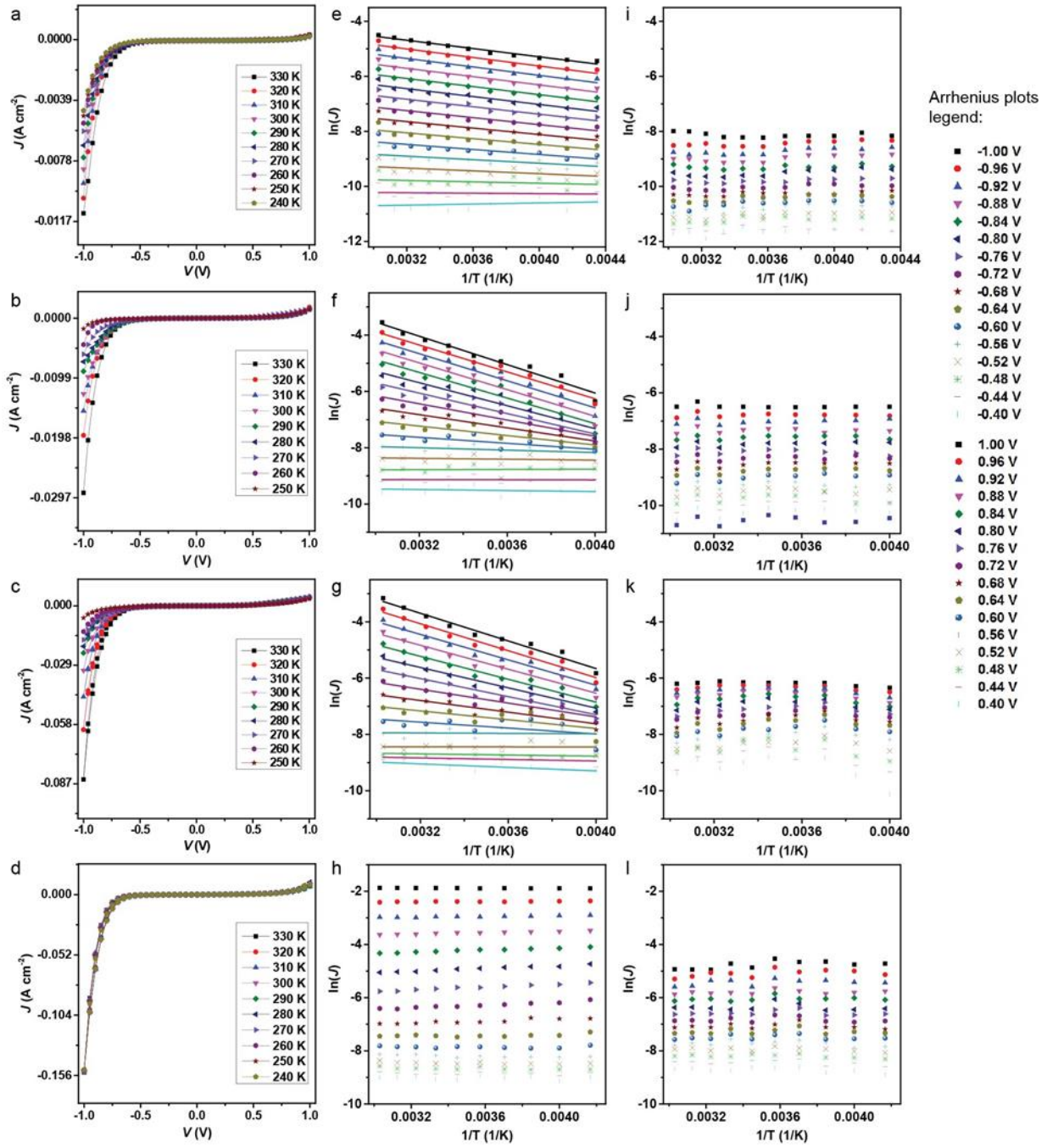

Figure 42: Temperature dependent *J*(V) data for junctions with SAMs of S-C-DPA-C_n-Fc, with n = 3 (a), 2 (b), 1 (c), or 0 (d), and the corresponding Arrhenius plots for *J* from -0.4 to -1.0 V (e-h) and from +0.40 to +1.0 V (i-l). The solid lines are fits to the Arrhenius equation.

The measurements show that the rectification can be tuned by changing the intramolecular coupling between the Fc and DPA units. The molecular diodes with n = 1, 2 and 3, rectify following a similar mechanism as reported before for diodes with an aliphatic backbone (i.e., $S(CH_2)_{11}Fc$) [73-76]). In contrast, the diodes with n = 0 rectify via a new mechanism since the mechanism of charge transport is activationless. In addition, the dependence of E_a on both n and applied bias, cannot be explained by the Marcus theory (which would predict activated transport for all cases) or Landauer theory (temperature independent transport for all cases). Here we argue that molecular orbital gating pushes the junctions with $n = 0$ into the inverted Marcus regime resulting in activationless transport despite strong interactions of the charge carriers with the molecular bridge.

5.4. Charge Transport in the Inverted Marcus Regime

As mentioned in the introduction, Marcus theory combined with the Landauer theory can be used to describe charge transfer where the charge carriers interact strongly with the molecule(s) inside the junction where the electron transfer rates between the neutral and charged molecular states (M and M^-) are expressed by [68]:

$$k_{M\to M^-} = \frac{1}{\sqrt{4\pi\lambda k_B T}} \int d\varepsilon \Gamma_1(\varepsilon)\, e^{-\frac{(\Delta E+\varepsilon-\lambda)^2}{4\lambda k_B T}} f(\varepsilon)$$
$$k_{M^-\to M} = \frac{1}{\sqrt{4\pi\lambda k_B T}} \int d\varepsilon \Gamma_1(\varepsilon)\, e^{-\frac{(\Delta E+\varepsilon+\lambda)^2}{4\lambda k_B T}} [1 - f(\varepsilon)] \quad (5.4)$$

where λ is the reorganization energy, $f(\varepsilon)$ is the Fermi distribution of the electron occupation in the junction electrodes, and $\Delta E = E_M(x_M) - E_{M^-}(x_{M^-}) + \mu$, where μ is the electrochemical potential of the electrodes, and x_M and x_{M^-} represent the configurations at equilibrium with the

molecular species M and M^- in the reaction coordinate. In the Marcus theory, the reaction energetics of the transition from M and M^- can be described using Marcus parabolas. Figure 1e (continuous lines) shows a typical energetically favorable electron transfer reaction with M^- lower in energy at equilibrium than the initial state M. The transition from M to M^-, however, does not occur spontaneously because of the energy barrier between the two states. This so-called activation energy E_a can be provided thermally or simply by applying a large bias. The value of E_a is directly related to the reorganization energy λ which is also defined in *Figure 43a*. This situation is the normal Marcus regime and electron transfer rates increase with increasing energy and $J \propto e^{-E_a/k_B T}$ applies. Migliore *et al.* [68] suggested that for junctions in the inverted Marcus regime, where the Marcus parabolas are arranged as shown in *Figure 43a* (dashed lines), the parabola of M^- crosses with the minimum of the parabola M at point x_c. In this situation, there is no activation energy and the mechanism of charge transport is activationless. To move the Marcus parabolas with respect to each other, independent electrical gating of M and M^- would be necessary, which can be achieved by charging nearby molecular orbitals (*i.e.*, intramolecular orbital gating).

Figure 43b illustrates the situation in the context of a molecular tunnel junction in an energy level diagram which includes the coupling to the environment by means of the nuclear coordinate x. In case μ lies in between the neutral and charged states, the system is in the normal Marcus regime and thermal fluctuations provide the energy necessary to transit from point A to B. The system can be pushed into the inverted Marcus regime when μ shifts (as a result of a gate bias) with respect to points A and B so that x_c reaches, and even overcomes, x_M (or x_{M^-} for the opposite bias). Beyond this point, no thermal energy is required to assist the transition and the

process becomes activationless. The value of E_a changes as a function of gate bias following a bell-shaped curve (inset of *Figure 43b*) arising from the overlapping exponentials in *Equations 5.4* and has a maximum value when μ lies half way between x_M and x_{M^-}. Therefore, by measuring the value of E_a as a function of gate bias one can observe how a junction moves from the normal to the inverted Marcus regime.

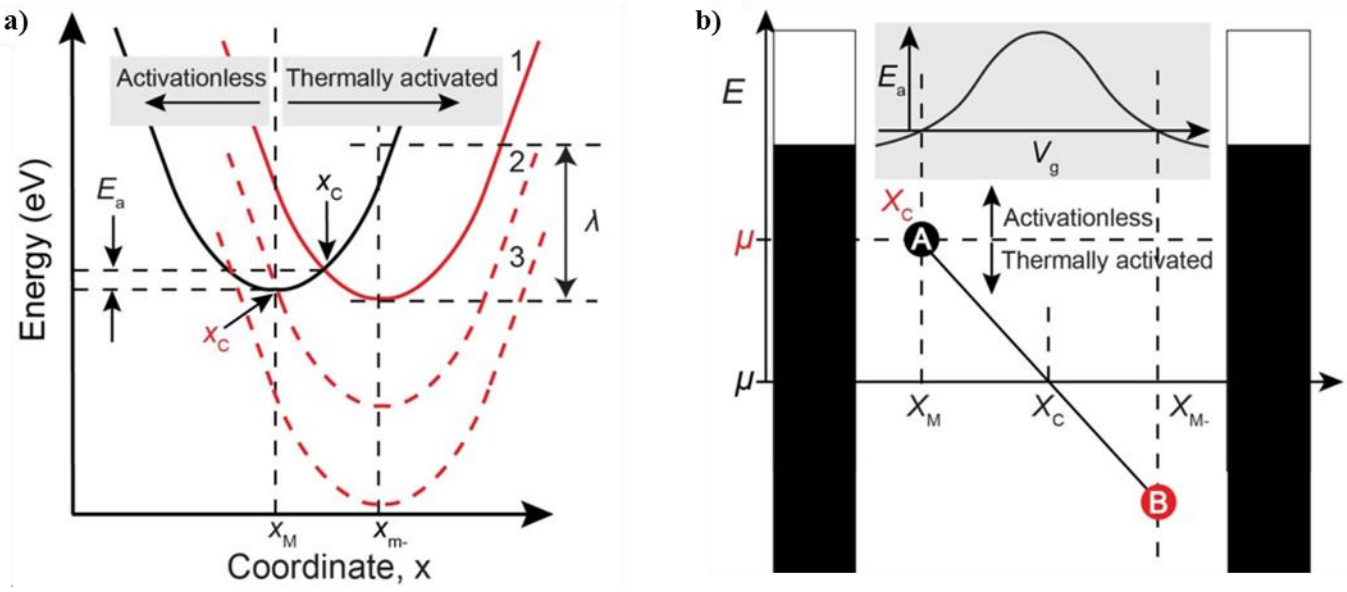

Figure 43: a) Marcus parabolas depicting a charge transfer process (here drawn for $M \rightarrow M^-$) in the Marcus (red solid line, parabola 1) or activationless in the inverted Marcus (red dashed lines, parabolas 2 and 3). See text for details. b) Schematic of the energetics of a molecular state in a tunnel junction in relation to the reaction coordinate *x*. μ is the electrochemical potential of electrons in the metal measured relative to vacuum. The inset illustrates E_a as a function of gating voltage (V_g).

We now return to interpreting the temperature dependence of the SAM-based junctions. The single-molecule experiments show that intramolecular orbital gating functions as a local electrostatic gate. This intramolecular gating could push the two-terminal SAM-based junction into the inverted Marcus region explaining the unusual behaviour of E_a as a function of both the applied bias and *n* shown in *Figure 44b*. The continuous lines in *Figure 44b* are fits to the model proposed by Migliore *et al*. [68] (*Equations 5.4*) corresponding to the bell-shaped function

describing E_a vs. gate voltage shown in *Figure 44a* using λ = 0.9 eV which results in maximum E_a of 230 meV close to the experimentally observed maximum. The value of ΔE = +0.9 eV is in agreement with the spectroscopy data and places the transition into the inverted Marcus regime around zero gate voltage.

The extent of molecular orbital gating is proportional to the charge in the molecule, which increases with bias (see fitting functions representing the charge Q(V, n) in *Figure 44c*). The value of V_c has been taken directly proportional to the bias dependency of the charge according to:

$$V_c(n) = \frac{Q(V,n)}{C_C^*(n)} = Q(V,n)\frac{C_C(n)}{C_1(n)C_2(n)} \quad (5.5)$$

which is a good approximation of the coupling potential $V_c = e\frac{C_c}{C_1C_2 - C_c^2}$ when $C_1C_2 \gg C_c^2$, with the effective capacitive couplings values for SAM-based junctions represented in *Table 3*:

Table 3: Effective capacitive couplings for n=1, 2 and 3 in SAM-based junctions.

	n = 1	**n = 2**	**n = 3**
C_C^*	1.88×10^{-19} F	2.12×10^{-19} F	3.48×10^{-19} F

We note that the C_C^* increases with separation, as expected from its inverse relation with the coupling capacitance, C_C, which decreases with separation between the units. The fitting results are in excellent agreement with the data and confirm the transition from the activationless inverted Marcus regime at V < -0.5 V (no charge in the molecule), to the thermally activated Marcus regime for V > -0.5 V. The corresponding maximum values of the intramolecular

coupling potential ($V_c(n) = Q(1V,n)/C_C^*(n)$ = 0.85, 0.75, and 0.46 V, for n = 1, 2 and 3, respectively) achieved in each molecule for the maximum bias (V_{max} = -1.0 V) are marked with dashed lines in *Figure 43a*.

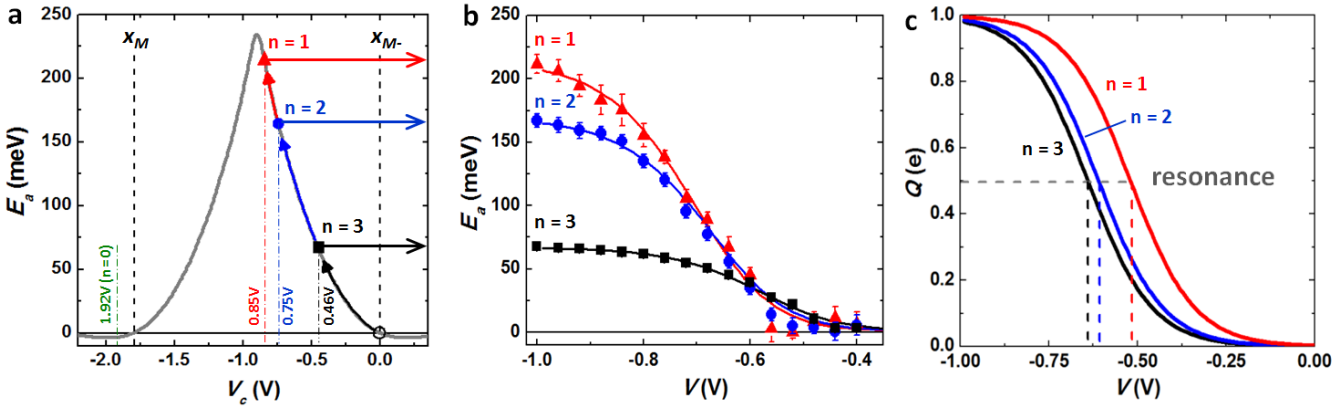

Figure 44: a) Bell-shaped activation energy vs. gate voltage function calculated from Eqns. 1used to fit the experimental results. b) Experimental activation energies of SAM-based junctions with n = 1, 2, and 3, (symbols) and the corresponding fits to the Marcus theory in which molecular orbital gating results from capacitive coupling between the Fc unit and DPA. c) Theoretical functional representing the charge in the n = 1, 2, and 3, molecules as a function of bias used to fit the results.

One can extend this interpretation to the case of the temperature independent behaviour of the SAM-based junction with n = 0. Although the absence of thermal activation in the transport precludes evaluating the exact value of the maximum coupling potential for n = 0, one can estimate it by linearly extrapolating the n = 1-3 values of the effective capacitive coupling, which results in $C_C^*(n=0) \sim 0.79\times10^{-19}$ F and $V_c(n=0) = Q(1V,n=0)/C_C^*(n=0) \sim 1.92$ V (*Figure 45*). This molecule has the largest intramolecular gating effect, pushing the molecule directly into the inverted Marcus region at negative bias. This explains why the mechanism of charge transport is independent of temperature despite the charge carriers interacting strongly with the molecule since all 4 molecules rectify and have similar lengths.

It is worth noting that the molecular orbital coupling between the Fc and DPA units in SAM-based junctions translates into gate voltages of the order of one volt, while in single molecule junctions is lower than 50mV (yellow and red arrows in *Figures 38 a-b*). This difference can be understood in terms of strong energy renormalization effects due to charge image effects in the electrodes [72, 77].

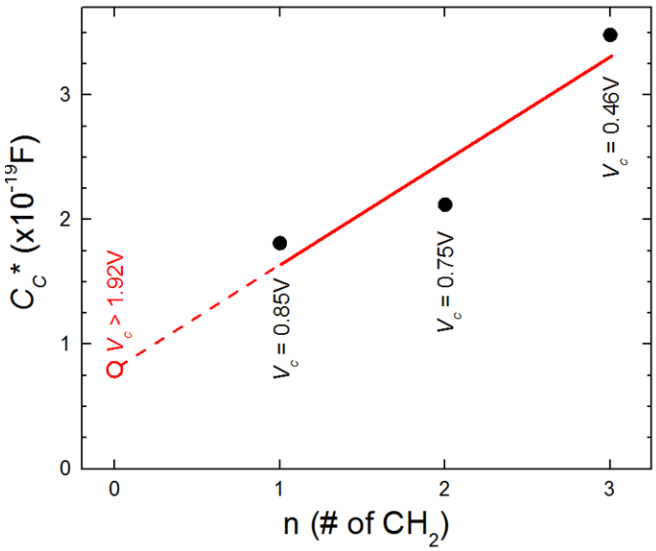

Figure 45: Effective coupling capacitance as a function of the number of CH_2 groups (n) separating the DPA and the ferrocene units (solid circles). The red line represents a linear fit to the data. Extrapolation to n = 0 gives an upper bound estimate for the effective coupling capacitance of 0.79×10^{-19} F, which represents a lower bound estimated for the coupling potential of 1.92 V.

5.5. Conclusions

We have demonstrated that the mechanism of charge transport of a molecular diode can be pushed deep into the inverted Marcus regime via intramolecular orbital gating. Our data fit well to a model put forward by Migliore *et al*. which combines both the Landauer and Marcus theories. These results indicate that molecular junctions can operate in between these two extremes with profound implications:

1. Temperature-dependent measurements alone cannot distinguish whether a junction operates in the coherent tunneling regime or in the charge transfer regime, as junctions in the inverted Marcus regime show activationless charge transport.
2. Despite the lack of solvent molecules in solid state molecular junctions, Marcus processes are important and must be taken into consideration, particularly for junctions in the weak coupling regime.
3. Intramolecular orbital gating can push a junction into the inverted Marcus regime eliminating the need for a gate electrode to do so.

The latter could lead to new means of controlling the mechanism of charge transport across molecular tunnel junctions. Also from a practical perspective, our results are interesting as they provide means of obtaining efficient molecular diodes (with nearly two orders of magnitude rectification) in both the Marcus and inverted Marcus regions. We hope that our results inspire future theoretical and experimental studies.

CHAPTER 6:
DEVELOPMENT OF GRAPHENE-BASED SINGLE-ELECTRON TRANSISTORS

6.1. Introduction

It was noted in Chapter 4 that graphene is a promising alternative as an electrode material for single-molecule measurements. Recent studies have demonstrated that graphene-based junctions are stable over weeks at room temperature [78], contrary to gold junctions that are stable only at low temperatures. In addition, graphene electrodes open the door to transport measurements in the presence of light, which will allow for the study of photo-active molecules [79] and plasmon resonances in gold nanoparticles, along with polarized current transport measurements via graphene-based spin valves. The fabrication of fully functionalized multilayer graphene-based single-electron transistors is reported in the present Chapter.

6.2. Graphene-based SETs Fabrication

6.2.1. Graphene exfoliation

Graphite is exfoliated onto a silicon/silicon oxide wafer (Waferpro: 3" N/AS <1-0-0> <0.005 ohm-cm, 381+/-25um prime silicon wafer, SSP, 1 SEMI FLAT with 2,800A+/-10% thermal oxide on both sides) patterned with alignment markers. The wafer has been previously cleaned using a standard recipe (acetone, ethanol and isopropanol). After exfoliation, the samples are studied under an optical microscope in order to select the optimal flakes. The aforementioned markers will serve as coordinates for the future localization of the flakes.

The criteria for selection is the following: the area around the flakes must be clean from graphite and glue and the flakes must be ≈ 3-20nm thickness (*Figure 46 a-b* shows an optical and AFM image of a desired flake). The reason for the thickness criteria being that the electrodes must be thin enough so that the gate coupling with the molecule is maximized, but thick enough that the electrodes still act as a continuous reservoir of electrons [78, 80, 81].

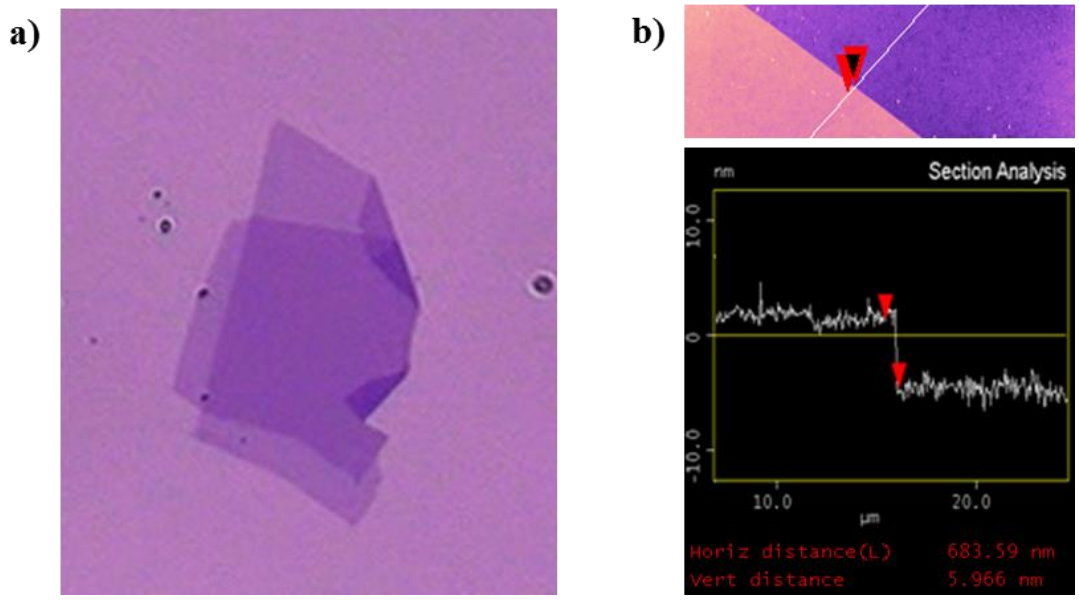

Figure 46: a) Optical image of an exfoliated multilayer graphene flake. b) AFM analysis of the flake step height.

Considering that each flake will present a different geometry, optical lithography is not an option and each transistor must be designed separately and patterned via electron beam lithography. The software used to design and pattern each device is DesignCad.

During the fabrication process, gold contacts are patterned first, followed by the writing and etching of the multilayer graphene nanowires.

6.2.2. Contacts

Figure 47 depicts the design of the contacts layer for one device. Each color in the figure represents a different layer. Each layer will be patterned at different currents, the larger the designed features are, the larger the current. This process allows the optimization of the writing time.

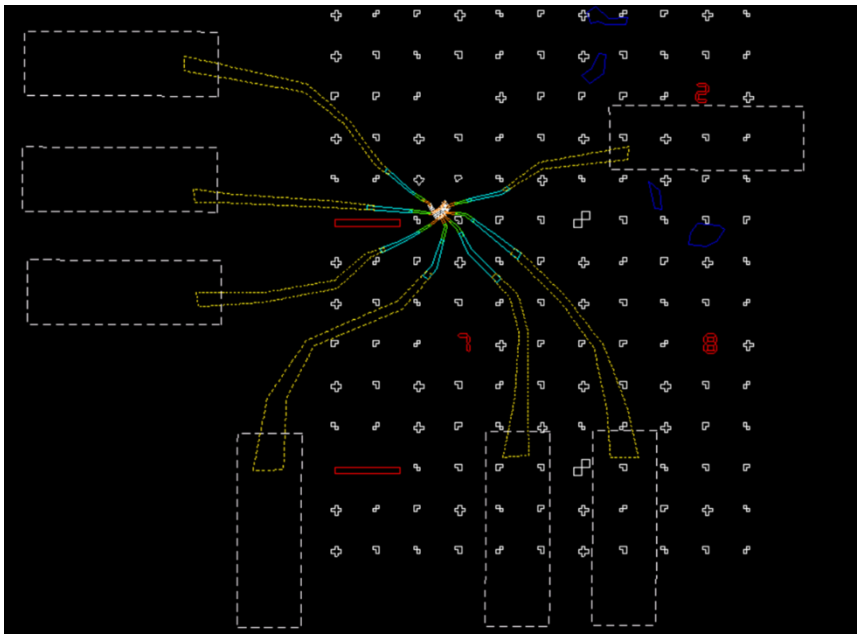

Figure 47: DesignCad design of the contacts of a transistor. The different colors represent different layers for the writing process.

After the design is ready, the sample is spin coated with e-beam resists (MMA 8.5 EL (6) and PMMA 495 A4) following the parameters in *Table 4*.

Table 4: Spin coating and baking parameters for MMA 8.5 EL (6)/PMMA 495 A4 bilayer.

MMA 8.5 EL (6)	PMMA 495 A4
2s at 500rpm/ 50s at 4000rpm/ 2s at 0rpm	2s at 500rpm/ 50s at 4000rpm/ 2s at 0rpm
Bake at 175°C for 5min	Bake at 175°C for 5min

A Vega SBH SEM built by Tescan is employed for the e-beam lithography process. The beam is aligned and a Run File is created. The Run File sets the magnification, current and dosage at which each layer is patterned. The current dosage corresponding to the MMA 8.5 EL (6)/ PMMA 495 A4 bilayer is 325 μC/area.

Once the writing is finished, the sample is developed in a MIBK:IPA (1:3) solution for 45s. Finally, 7nm of Ti and 75nm of Au are deposited by means of an e-beam evaporator. The process is completed by submerging the sample in acetone, which will lift-off all the unwanted metal.

6.2.3. Nanowires

The nanowires are patterned following a similar procedure as the one described above. The desired etching pattern is designed (*Figure 48*) and the sample is spin-coated with PMMA 495 A2 and PMMA 495 A5 (*Table 5*). This recipe allows the writing of features as small as 100nm.

Table 5: Spin coating and baking parameters for 3 layers of PMMA 495 A2 and a layer of PMMA 495 A4.

3 layers of PMMA 495 A2	**PMMA 495 A4**
2s at 500rpm/ 50s at 4000rpm/ 2s at 0rpm	2s at 500rpm/ 50s at 4000rpm/ 2s at 0rpm
Bake at 170°C for 5min	Bake at 170°C for 5min

The current dosage corresponding to three layers of PMMA 495 A2 and a layer of PMMA 495 A4 is 550 μC/area.

The device is developed in a cold solution of isopropanol and DI water (3:1) for 1min 20s. Once the development process is finished, a SAMCO RIE etcher is employed to etch the

multilayer graphene from the exposed areas. The parameters optimized for the etching of the nanowires are detailed in *Table 6*.

Table 6: SAMCO RIE etcher parameters for multilayer graphene etching.

Power	scc	Pressure	Time
50 W	5	53 mTorr	16s

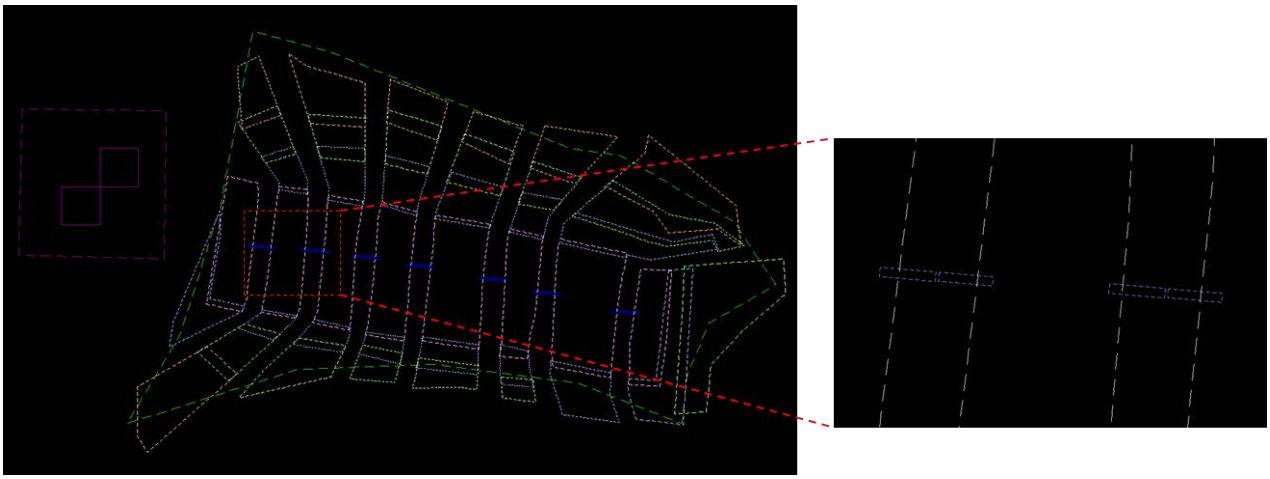

Figure 48: DesignCad design of the graphene etching layers. The narrowest part is designed to be 100nm wide. The green dashed lines follow the edges of the flake. The inset shows a zoom into the 100nm narrowing.

The sample is then left in acetone overnight to remove the remainder e-beam resist. Once the transistors are clean from residues, they are electrically characterized with a probe station. The nanowires resistance should be between 1- 2 kOhm. Finally, the transistors are wire bonded to a chip carrier. The parameters used for the wire bonding of graphene-based transistors are represented in *Table 7*. It is crucial not to use a higher power or force than the ones in *Table 7*, as it could burn the device.

Table 7: Parameters for wire bonding graphene-based transistors.

	Search	*Force*	*Time*	*Power*
1st bond	0	5.2	5.5	464
2nd bond	20	1.5	3	300

6.2.3. Nanogap

The nanogap is opened using a feedback controlled electroburning technique [79]. Voltage is applied between the gold leads, generating current through the nanowires and heating graphene by the Joule effect. The hot carbon atoms react with the oxygen in the atmosphere and burn.

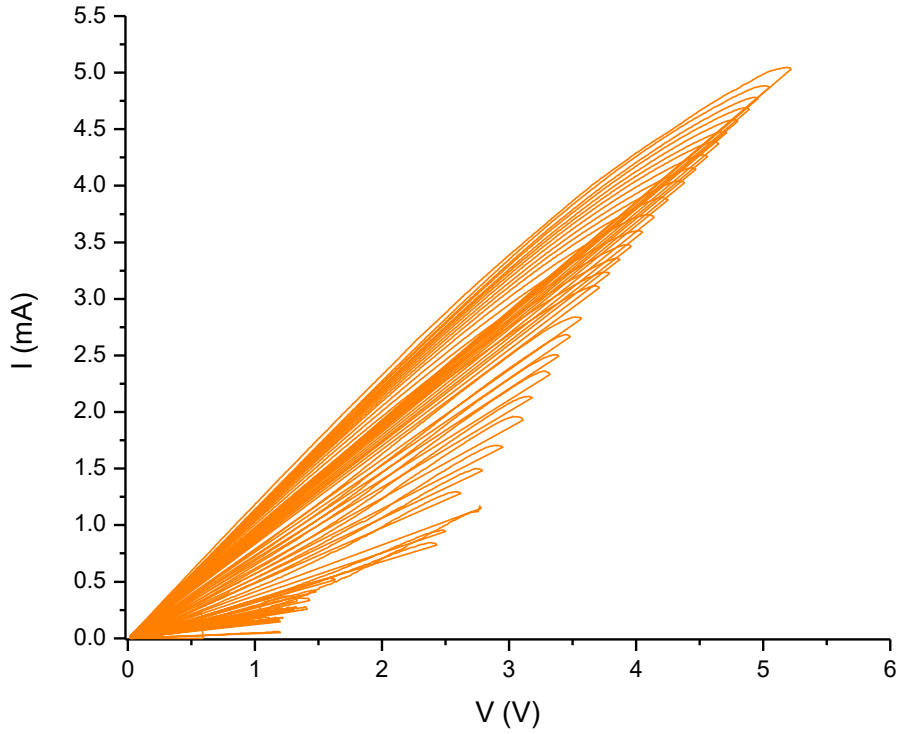

Figure 49: I-V graph of the feedback-controlled electroburning induced breaking process at room temperature. The process is stopped when the resistance through the nanowire reaches 4 MOhms.

The program used to control the graphene breaking is similar to the one explained in Section 5.2.1. The current through the nanowire is recorded while increasing the bias voltage. Once the current drops 0.002%, the voltage is recoiled back to zero in miliseconds. The process is repeated until the resistance reaches 4MOhms (*Figure 49*). The values of the percentage of the current drop and the final resistance have been optimized through several breaking processes. For more information about the different parameters used in the Labview program see *Appendix B.*

6.3. Gap Characterization

In order to estimate the gap size generated, current-voltage characteristics are recorded. *Figure 50* shows an IV curve indicative of tunneling behavior. The dashed line in the figure is a fit from the Simmons model.

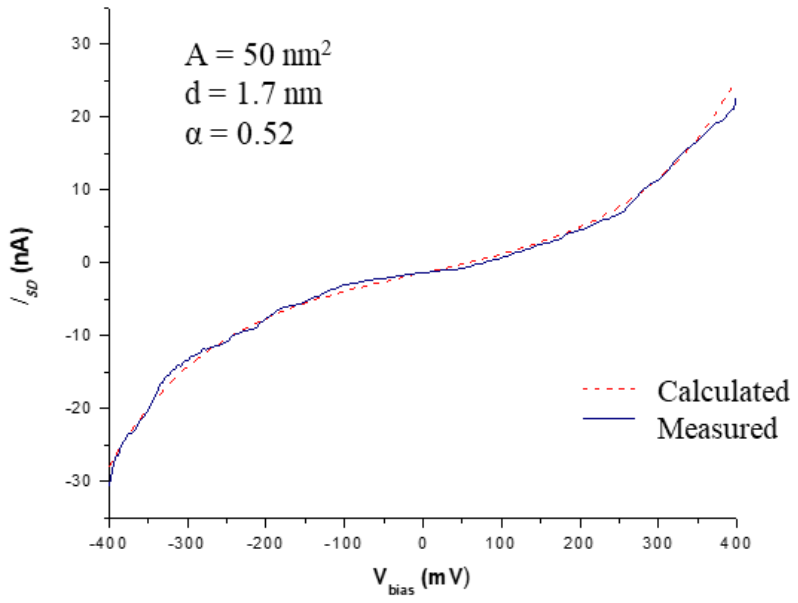

Figure 50: I-V characteristic of a multilayer graphene nanogap (blue solid line). The dashed line represents the Simmons model fit with a gap of 1.7nm, an area (A) of 50nm^2 and an asymmetry of 0.52.

6.3.1. Simmons model

The Simmons model describes the current-voltage behavior of tunneling junctions under vacuum. It assumes a trapezoidal barrier when the $V_{bias} < \Phi$, where Φ is the barrier height [82] (*Figure 51*). Bearing that in mind, the current density in the tunnel junction is given by [53, 83]:

$$j = e\frac{4\pi m}{h^3}\int_0^\infty d\varepsilon[f_L(\varepsilon) - f_R(\varepsilon)]\int_0^\varepsilon d\varepsilon_x T(\varepsilon_x) = e\frac{4\pi m}{h^3}\int_{\mu_R}^{\mu_L} d\varepsilon \int_0^\varepsilon d\varepsilon_x T(\varepsilon_x) \quad (6.\ 1)$$

where $T(\varepsilon_x)$ is the tunnel probability of an electron with kinetic energy ε_x in the x-direction, and it has been assumed that $k_BT << \mu_L, \mu_D, \Phi$. Therefore, the Fermi distribution of the electrons energy in the leads can be approximated to a step function.

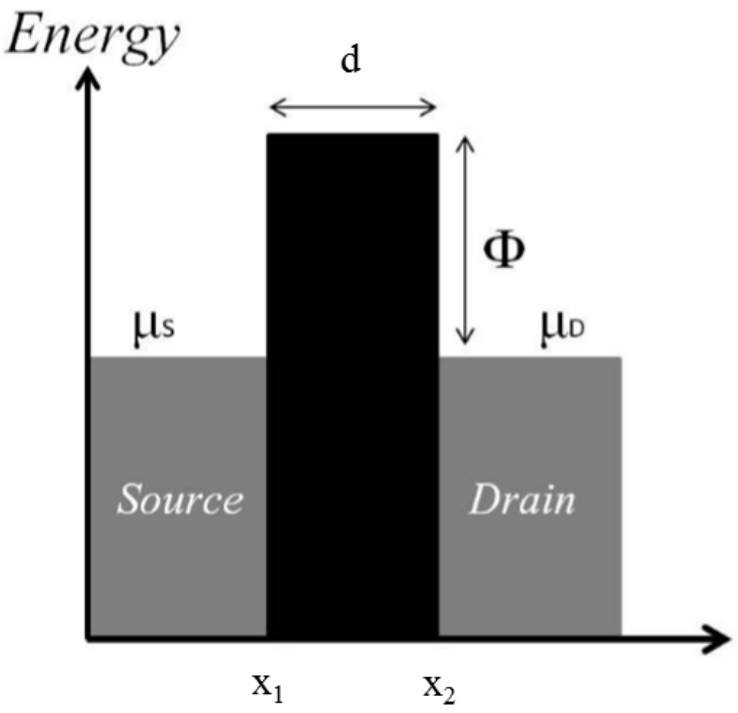

Figure 51: Schematic energy diagram of a junction with a thin insulating film of width d between source and drain. Where Φ is the potential barrier height.

Using the WKB-approximation, one can obtain an expression for the tunnel probability [53]:

$$T(\varepsilon_x) = e^{-\frac{2}{\hbar}\int_{x_1}^{x_2} dx|p_x|} = e^{-\beta\int_{x_1}^{x_2} dx\sqrt{\Phi(x)-\varepsilon_x}} = e^{-\beta d\sqrt{\Phi-\varepsilon_x}} \qquad (6.\ 2)$$

where $\beta = 2\frac{\sqrt{2m}}{\hbar}$, $d = x_2 - x_1$ and Φ is independent of x when the left and right electrodes have the same work function (situation illustrated in *Figure 50*).

Substituting *Equation 7.2* into Equation *7.1*, the current density becomes:

$$j \approx \frac{e}{2\pi h d^2}\left[(\Phi-\mu_L)e^{-2d\frac{\sqrt{2m(\Phi-\mu_L)}}{\hbar}} - (\Phi-\mu_R)e^{-2d\frac{\sqrt{2m(\Phi-\mu_R)}}{\hbar}}\right] \qquad (6.\ 3)$$

Equation 6.3 is a good approximation when the junction has totally symmetric electrodes. For a more general model, we can introduce a parameter (α) that will account for the asymmetry between the electrodes (*Equation 6.4*) [58].

$$j \approx \frac{e}{2\pi h d^2}\left[(\Phi-\alpha\mu_L)e^{-2d\frac{\sqrt{2m(\Phi-\alpha\mu_L)}}{\hbar}} - (\Phi-(1-\alpha)\mu_R)e^{-2d\frac{\sqrt{2m(\Phi-(1-\alpha)\mu_R)}}{\hbar}}\right] \qquad (6.\ 4)$$

6.3.2. Statistics

From the electroburning of 50 junctions, 8 broke abruptly (the feedback was not fast enough during the breaking process), 8 broke all the way hours after the electroburning process and 34 showed the characteristic tunneling I-V response (statistics shown in *Figure 52*). The Simmons model was used to fit the IV curves of the 34 junctions and the gap size corresponded to 1.5nm – 2nm.

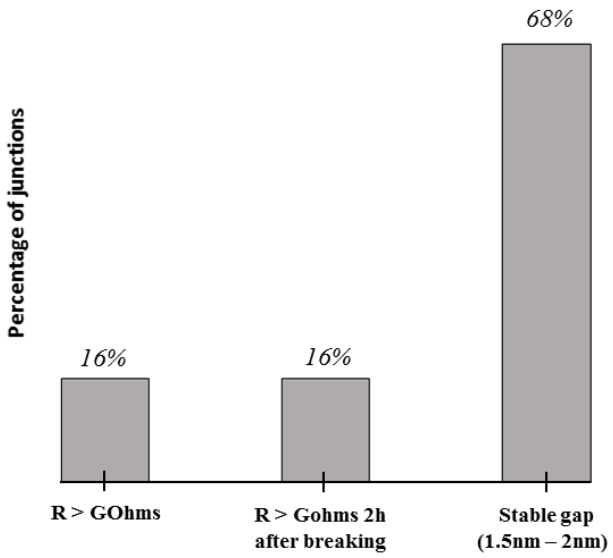

Figure 52: Histogram of the percentage of junctions divided in three groups: infinite resistance in the electroburning process (16%), infinite resistance 2h after breaking (16%), stable gap over time of 1.5nm to 2nm (68%).

6.4. Conclusions

The fabrication of multilayer graphene transistors with a nano-constriction of 100nm (*Figure 52*) and the subsequent controlled electroburning process for the generation of gaps between 1.5 and 2nm has been reported in this Chapter. The gaps are electrically characterized and the gap sizes are estimated by fitting the tunneling IV curves to the Simmons Model.

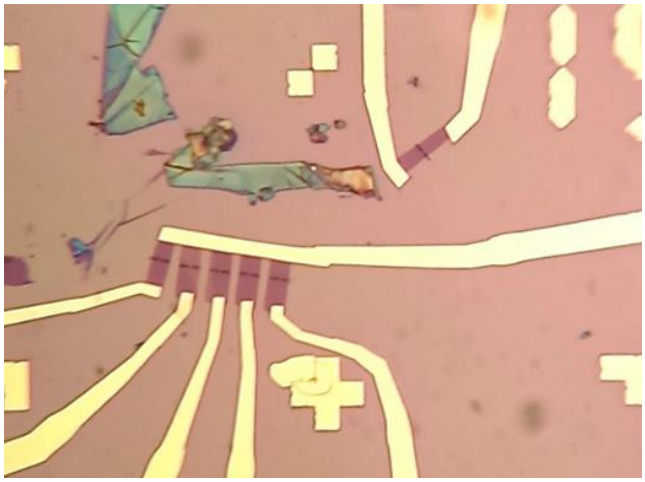

Figure 53: Optical image of six multilayer-graphene based nanowires.

CHAPTER 7:
GRAPHENE-BASED GATEABLE SCANNING TUNNELING MICROSCOPY

7.1. Introduction

Scanning probe microscopy techniques have been widely used to study the conduction through individual molecules deposited on a metallic surface (Chapter 4). Unfortunately, these two-terminal transport measuring techniques lack the possibility of electrically gating the molecules, limiting a complete spectroscopic determination of the energy landscape. Alternatively, three-terminal SET devices, as the ones described in Chapter 5 and 6, although excellent for transport spectroscopy, carry low yields and a lack of control of the molecule's disposition within the junction region.

The work presented in the current chapter pretends to overcome the gate limitation of the STM measurements by efficiently gating through graphene. Although there have been some advances in this direction, the coulomb blockade diamond of a molecule has never been measured by means of an STM [84, 85].

7.2. Device Fabrication and Characterization

The STM images and measurements in the present section and in section 7.3 are done in collaboration with Jens Martin at NUS.

Figure 54 illustrates the device geometry. The transistor is based on an undoped GaAs wafer with high quality CVD graphene transferred on top of an aluminum gate, which has been previously oxidized (2nm of oxide layer). The patterning consists of four steps: a first contact

layer for the gates (5nm Ti/15nm Au), Al/Al_2O_3 gates (45nm), CVD graphene transfer, and a second contact layer for the gates and contacts for graphene (5nm Ti/85nm Cu/20nm Au). For a detailed fabrication recipe see *Appendix C*.

Once the lithography processes are completed, the sample is annealed using an optimized flow of Argon and Hydrogen at 300 degrees Celsius for further cleaning of the graphene sheet.

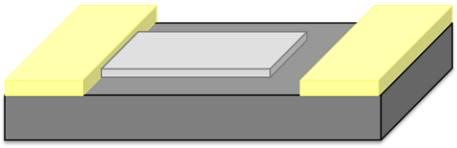

Figure 54: Schematic illustration of the CVD graphene transistor device. The device is patterned on top of a GaAs wafer.

STM measurements require atomically clean samples. To confirm the imaging of molecules would be possible in the proposed device, the quality and roughness of the CVD graphene on top of the aluminum gate were analyzed via AFM and STM. *Figure 55 a-b* shows AMF and STM images of graphene in one of our devices. From the AFM scale bar, it can be inferred that the roughness of our transistors is ±1nm. At the same time, *Figure 55b* shows that our graphene is atomically clean.

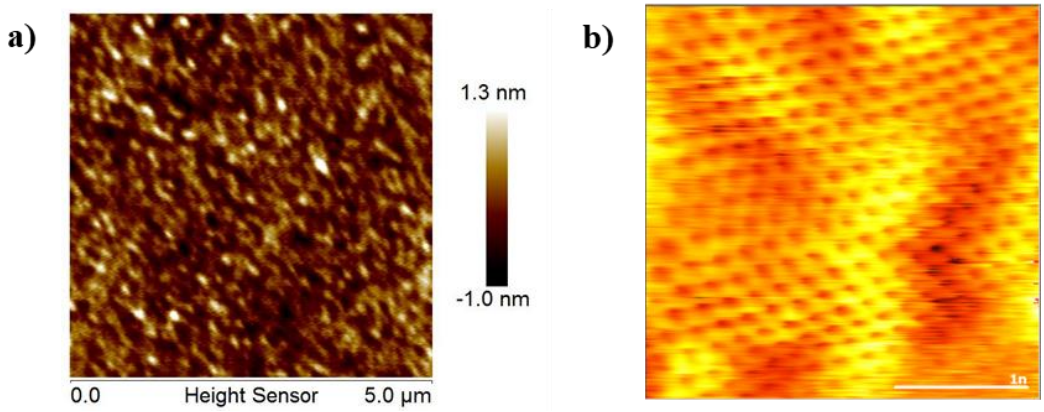

Figure 55: a) AFM height image of CVD graphene on top of an Al/Al_2O_3 gate. The roughness in an area of 5µm by 5µm is ±1nm. b) STM image taken in constant current mode of CVD graphene lattice on top of an Al/Al_2O_3 gate. The scale bar is 1nm.

We also examined the gate dependence of the graphene sheet. *Figure 56 a-b* show the STM spectroscopy measurements taken at liquid Nitrogen temperatures.

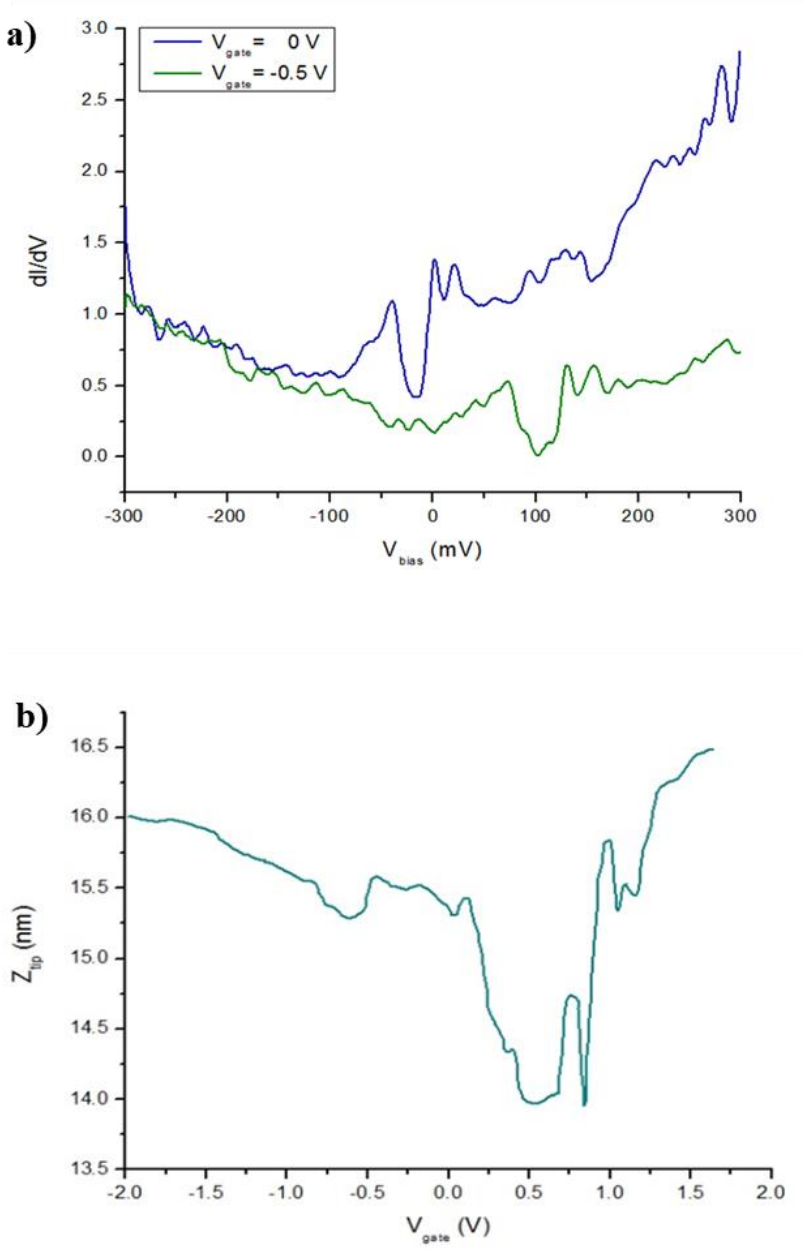

Figure 56: a) Conductance versus bias voltage for two different gate voltages (V_{gate} = 0V and V_{gate} = -0.5V). b) Tip Height (z) versus gate voltage. Measurement taken at a constant tunneling current. Graphene Dirac point is located at positive 0.5V gate voltage.

7.3. PTM Radical Molecules

The molecules chosen for the study are polychlorotriphenylmethyl (PTM) radicals synthesized by our collaborator Jaume Veciana. The chemical structure and energy scheme of the PTM radical can be seen in *Figure 57 a-b*. The energy scheme was obtained using DFT calculations [86].

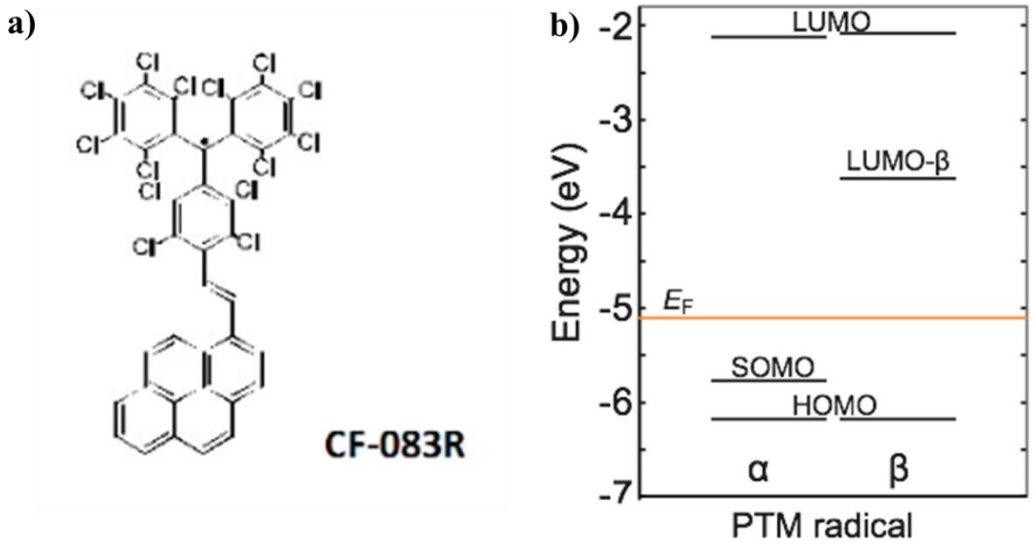

Figure 57: a) Chemical structure of a polychlorotriphenylmethyl (PTM) radical. b) Energy scheme of the PTM radical obtained via DFT calculations.

7.3.1. Molecule deposition

Studies for the optimization of the deposition process were performed. The first approach was to optimize the concentration on a HOPG substrate. *Figure 58* consists of two AFM images of the molecules on HOPG. The first HOPG sample (*Figure 58a*) was immersed for 90min in a solution of PTM radical molecules diluted in Toluene ($1x10^{-4}$ M), whereas 20μL of the same solution were drop casted for the second sample (*Figure 58b*).

In *Figure 58a* either residues or molecules accumulations can be observed. However, the sample obtained by drop casting shows a clean surface with elongated bright features on top. A height profile of the bright features measured an average thickness of 1.2nm, thus confirming that these features are monolayer molecule arrangements.

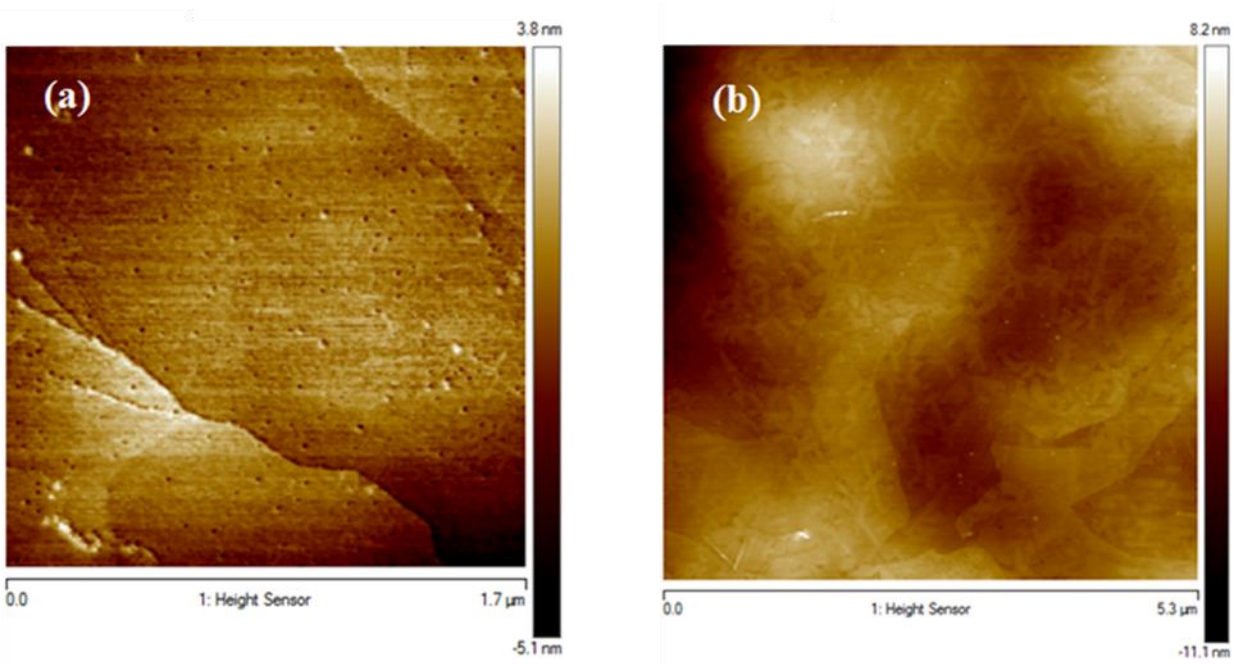

Figure 58: AFM images of the radical molecules on the surface of cleaned HOPG grown with different methods. a) immersing HOPG in $1x10^{-4}$M solution of toluene for 90min. b) drop casting 20µL of the same solution.

The same dilution concentration and drop casting method was used for our devices. The AFM images, height and phase profile, are displayed in *Figure 59 a-b*. From the images, it can be observed that the surface is almost fully covered by molecules. The dark spots in the height profile image (bright spots in the phase profile image) correspond to the areas without molecules. Some elongated features can still be appreciated in the height profile image.

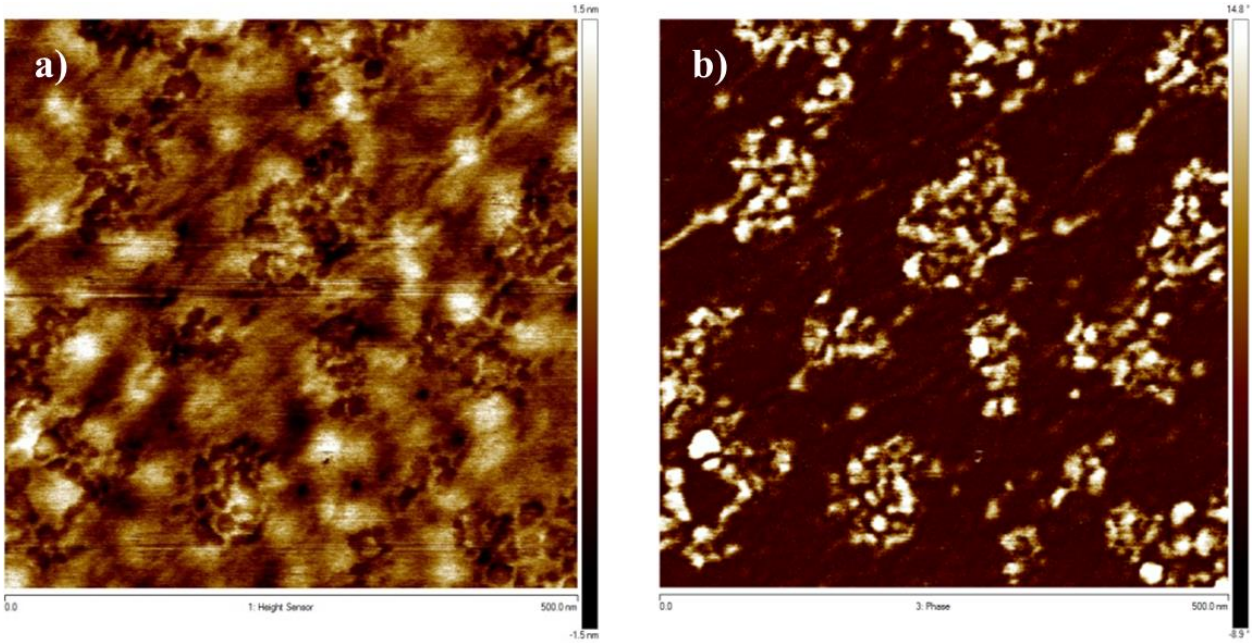

Figure 59: a) AFM height profile of PTM radical molecules drop casted on CVD graphene. b) AFM phase profile of PTM radical molecules drop casted on CVD graphene. Both images are taken on top of the Al/Al_2O_3 gate.

We have determined that the CVD Graphene surface is atomically clean, tested the efficiency of the gate, and optimized the deposition of the PTM radical molecules on our devices. The next step is to analyze the molecules with the STM.

7.3.2. STM measurements

In the following page, scanning tunneling images of PTM molecules on top of CVD graphene are shown (*Figure 60 a-b*). The images show the graphene lattice distorted. The distortion is due to the presence of molecules between the tip and graphene. However, the high charging energy of the molecules made the imaging of its density of states impossible.

A recent study performed in SET, demonstrates that within a gate window of ±4V it is not possible to charge the PTM radical molecule [86], hence this molecule is not suitable for our experiment.

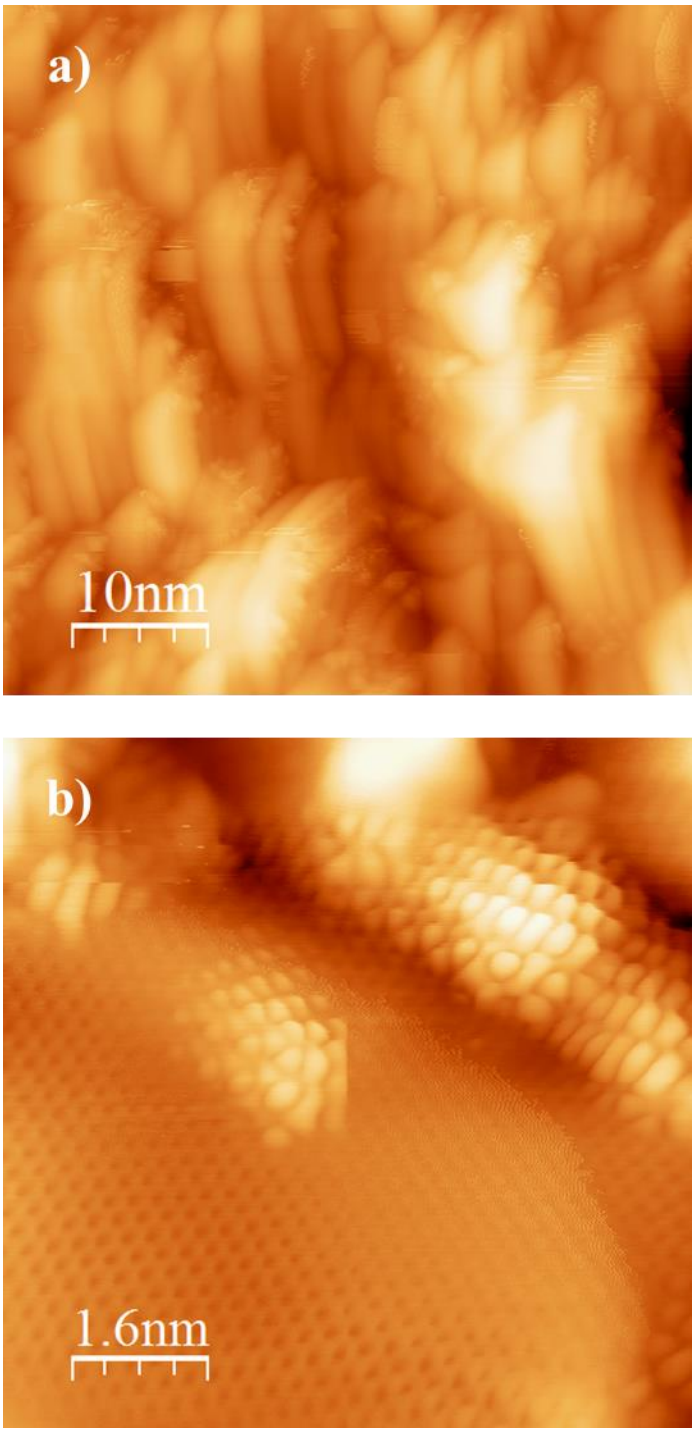

Figure 60: Scanning tunneling images of PTM molecules on top of CVD graphene. a) area scanned is 40nm by 40nm. b) area scanned is 5nm by 5nm.

7.4. C_{60} Molecules

The work presented in this section was performed in collaboration with Masahiro Ishigami at UCF.

Fullerene molecules (C_{60}) (chemical structure represented in *Figure 61*) were chosen this time. The temperature for its sublimation and the parameters for imaging its density of states have been previously reported, since C_{60} molecules have been thoroughly studied in the STM field [56]. However, none of the reports show a complete spectroscopy (coulomb blockade diamond) of the molecule.

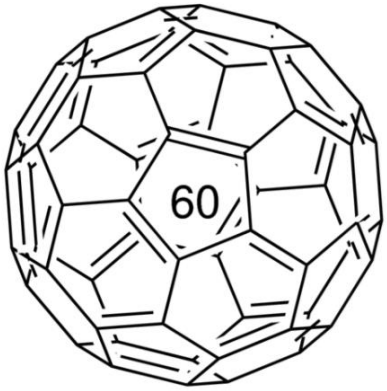

Figure 61: Fullerene C_{60} molecule chemical structure.

7.4.1. Molecules deposition

We wanted to avoid the presence of solvent in our samples, therefore the molecules had to be sublimated in situ. In order to determine the parameters for the molecule evaporation, a thermocouple was installed in a UHV chamber with a thickness monitor attached to it (*Figure 62a*). The current and voltage parameters were slowly increased until a constant frequency shift of 10 Hz was observed in the crystal. The obtained parameters are represented in *Table 8*.

Table 8: Current, voltage and frequency parameters for C_{60} sublimation in UHV.

Current	Voltage	Freq. shift
0.75 A	6.0 V	10 Hz

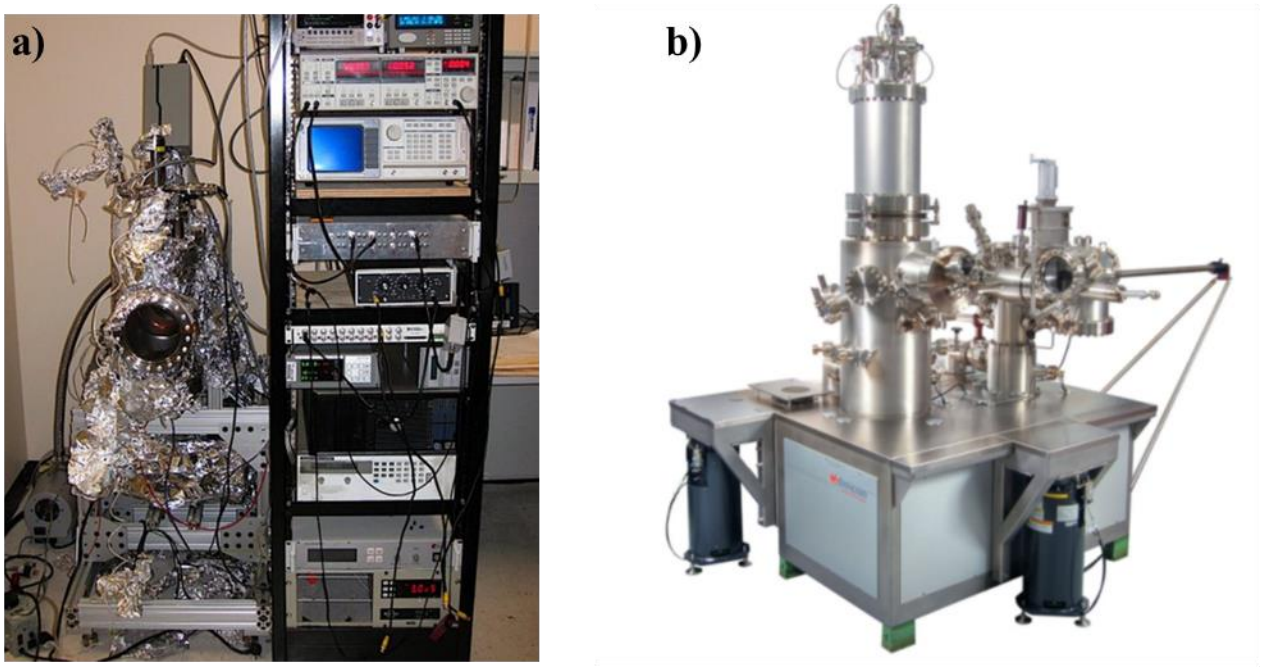

Figure 62: a) UHV chamber with thickness monitor employed to obtain the current and voltage parameters for the sublimation of the C_{60} molecules. b) Omicron scanning tunneling microscope used for the measurements presented in this section.

Once the sublimation parameters were established, an HOPG sample was prepared and the thermocouple was installed in the STM prep chamber (*Figure 62b*). The thermocouple current and voltage parameters were set to the values in *Table 8*, and the sample was exposed to the sublimated molecule in UHV for 30s. To assure only a monolayer of C_{60} was present in the sample, after the sublimation, the substrate was heated at 450 degrees (temperature above C_{60}

evaporation) for 5s. *Figure 63* shows an STM image of the monolayer of C_{60} molecules obtained on the HOPG substrate.

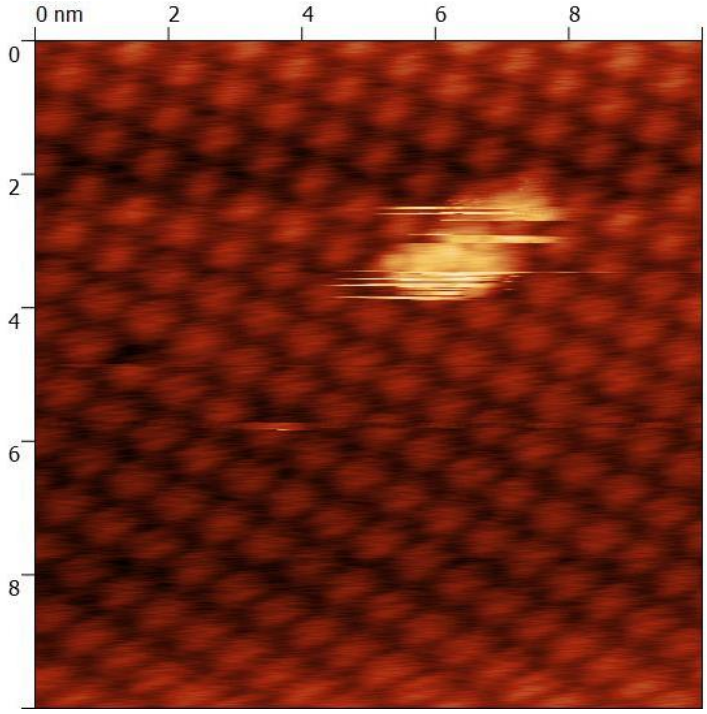

Figure 63: Scanning Tunneling Microscope constant current image of sublimed C_{60} molecules on top of HOPG.

7.4.2. Future work

Unfortunately, after taking the image in *Figure 63* the measurements had to be stopped due to a leak in the STM system. The next step is to use the same sublimation parameters on a CVD graphene-based transistor, confirm that a monolayer of C_{60} molecules is present and perform spectroscopy measurements for different gate voltage values.

APPENDIX A:
GRAPHENE TRANSFER PROCESS

Graphene Transfer Recipe

1. Cut the desired size piece of copper foil (with graphene on both sides).
2. Cut a piece of plastic slightly larger than the copper foil piece. Blow N2 on it.
3. Use Kapston tape to tie the copper foil on the plastic as shown in the *Figure 64a*, very carefully so the copper foil does not bend.

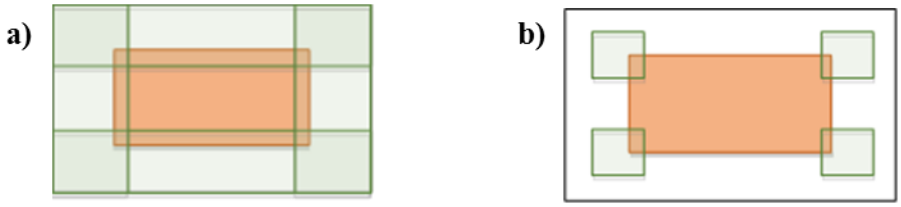

Figure 64: Illustration showing the graphene/Cu foil tied on plastic with Kapton tape ready for spin coating. b) Graphical representation of how to prepare the graphene/Cu for etching.

4. Spin coat a layer of PMMA A4 495 resist using program G. (4000 rpm 45 seconds)
5. Heat at 155° C for 3 minutes.
6. Very carefully remove the tape.
7. Place the copper foil with the spin coated side facing down on a new piece of plastic.
8. Use Kapston tape to tie the copper foil (*Figure 64b*).
9. Etch graphene with O_2 plasma Oxidation (see *Table 9*).
10. Remove the tape and cut the copper foil into smaller pieces if necessary.
11. Prepare 1% APS Copper etchant solution on a plastic container.

Table 9: O_2 plasma parameters for CVD graphene etching.

SCCM	Power	Pressure	Time
5	50 W	53 mTorr	45 s

12. Place very gently the copper pieces with the spin coated side facing up in the solution.
13. Leave overnight
14. Prepare a small container with ultrapure water and place a clean glass slide in it.
15. Prepare new 1% APS Copper etchant solution on a clean plastic container.
16. After leaving it overnight the copper has been etched, we will find a layer of polymer and graphene floating in the solution.
17. Use the clean glass slide previously placed in ultrapure water to scoop graphene out of the solution. Place the glass slide into the solution at a 45° angle and very carefully approach the target piece. Once the film is touching the glass slide slowly remove it from the solution and place it carefully into the fresh 1% APS solution.
18. Leave on solution for 3 hours.
19. After 3 hours, place ultrapure water in a plastic container.
20. Scoop graphene out of the 1% APS solution (same as n and q) and place it in the ultrapure water container.
21. Leave overnight
22. Prepare a new recipient with fresh ultrapure water.
23. Scoop graphene out of the water and place it in the fresh ultrapure water recipient. Leave for 3 hours.
24. Scoop graphene out of ultrapure water container, instead of using a glass slide for the process now we will be using the desired substrate previously cleaned using standard process.

25. Wait for the water between the substrate and graphene to evaporate (5-10 minutes). Then heat at 55°C for 5 minutes and at 180°C for 5 minutes after that.
26. Leave the sample cool down (usually 5 minutes) and place it in acetone for 5 minutes.
27. Place the substrate in a fresh acetone recipient. Leave overnight
28. Remove from acetone and gently blow dry with N2

APPENDIX B:
PARAMETERS FOR FEEDBACK-CONTROLLED LABVIEW PROGRAM

Control parameters used in the Labview program (*Figure 65*) for the feedback-controlled electroburning process are represented in *Table 10*.

Table 10: Control parameters for feed-back controlled Labview program

Initial Drain Voltage	0.010 V
Final Drain Voltage	7.0 V
Increment Drain Voltage	0.010 V
Initial Percentage	0.002%
Current to Change	2.6 mA
Percentage After Change	0.0025%
Resistance to Stop	4.5 MOhms

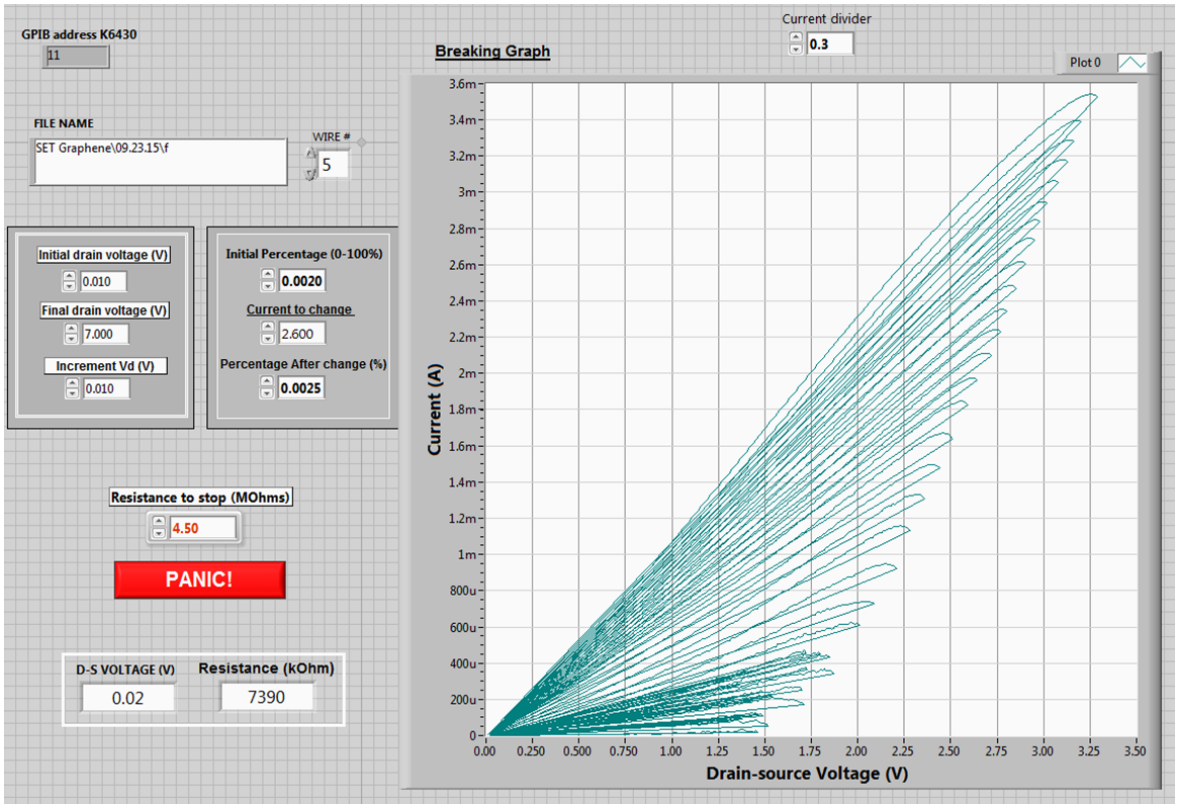

Figure 65: Screenshot of the Labview program interface.

APPENDIX C:
GRAPHENE-BASED TRANSISTORS FOR STM MEASUREMENTS FABRICATION RECIPE

Photolithography Process

Sample Preparation:

a. Take a **Si/SiO2 doped** wafer and cut it pieces of **11 mm** x **2.5 mm** (2.5 mm maximum, these are the dimensions for the STM in Singapore)
b. Clean wafer with Acetone, Ethanol, and IPA (in that order) then blow dry with Nitrogen gas.

Polymers Spin Coating:

c. Clean wafer with Acetone, Ethanol, and IPA (in that order) then blow dry with Nitrogen gas.
d. Spin **LOR** resist and bake for **5 minutes** at **175°C**.
e. Spin **Shipley** resist and bake for **2 minutes** at **120°C**.

Table 11: Spin coating parameters for LOR 3A and Shipley bilayer.

LOR 3A (B)	Shipley S1813 (A)
2s at 500rpm / 30s at 3000rpm / 2s at 0rpm	2s at 500rpm / 30s at 5000rpm / 2s at 0rpm

Alignment and Development:

f. Clean Mask with Acetone, Ethanol, IPA and then sonication in DI water for at least 5 minutes.
g. Place wafer on mask aligner using cut away plastic to ensure sample vacuum. (**Read guide lines of Mask Aligner**).
h. With your eyes align wafer piece to the sample pattern on the mask.

i. Using contact vacuum raise wafer also you can use the dial.

j. Use micrometers to align layers.

k. Once it is aligned, check the intensity of the UV-light in order to choose the time of exposition correctly. The exposing relation must be ~ $\mathbf{126}\ \frac{\mathbf{mJ}}{\mathbf{cm^2}}$.

l. After exposing, develop in **CD-26** for **45 seconds**, then quickly in DI water.

m. Blow dry with Nitrogen.

n. Check under the microscope, if the etches and color is good and uniform; place the sample at **130° C** for **5 minutes**, then **1 minute** in **CD-26** followed by DI water and Nitrogen blow dry.

o. It is very recommendable to use new CD-26 in every development. Also, Change DI water every time that it has been used.

Gold Layer (for Al contact)

a. Tape sample on sample holder and mount in chamber. The evaporations should take place at **<5E-6 Torr**.

b. Right before this deposition clean the wafer with **O2 plasma.**

Table 12: O_2 plasma parameters to remove residues before evaporation.

SCCM	Power	Pressure	Time
12	50 W	200 mTorr	10 s

Table 13: Evaporation parameters for Layer 1 (17~20 nm Ti/Au).

	Ti	Au
Density	**4.5 g/cm^3**	**19.3**
Z-ratio	**0.628**	**0.381**
Tooling Factor	**170 %**	**175 %**
Deposition Rate	**1 Å/s**	**1.5 Å/s**
Thickness	**10 nm**	**10 nm**
Current	**~30 mA**	**~ 50**

Aluminum Gates

a. Repeat steps from Polymer Spin Coating to Development.
b. Tape sample on sample holder and mount in chamber. The evaporations should take place at **<5E-6 Torr**.
c. Before every deposition clean the wafer right before the evaporation with **O2 plasma.** Using parameters from *Table 12*.
d. Evaporate 10nm before opening the shutter in order to remove the Al2O3 first.

Table 14: Evaporation parameters for Aluminum.

	Al
Density	***2.7 g/cm^3***
Z-ratio	***1.08***
Tooling Factor	***160 %***
Deposition Rate	***0.6 Å/s***
Thickness	***45 nm***
Current	***~200 mA***

Oxidation:

e. After the Aluminum evaporation, turn off e-beam source and ion gauge and leave it cooling down for 1hour. Use the manual **Instructions to be followed by user during introduction of oxygen to the Evaporator Chamber**. This manual is next to the chamber in the clean room.
f. First open the oxygen valve and then add oxygen "slowly" to the chamber with the leak valve
g. Stop at **250 mTorr**
h. Close oxygen valve and the leak valve
i. Leave it in **250 mTorr** for **40 min**
j. Then, pump with **dry pump** for **15s** and then **roughing pump** around **20 min** (until pressure in the chamber is very low)
k. Then turn off roughing and dry pump
l. Vent chamber

Aluminum Lift Off and Oxidation:

m. For the **Al** layer place the sample in **Acetone** at **Room Temperature** for about **45 min**, spray with acetone for helping the lift off, followed by **5 min** in **PG** and then DI water.
n. After lift off leave the sample for **24** hours at atmosphere conditions. Also, it might be useful to oxidize the gates even more with **O2 plasma Oxidation.**
o. Then check with meter or probe station the resistance of the gates. They should be around **~ 400 Ω**.

Table 15: O_2 plasma parameters for Aluminum oxidation.

SCCM	Power	Pressure	Time
12	50 W	100 mTorr	10 min

Graphene transfer (see *Appendix A*)

Gold Layer (Contact for Graphene and Second Layer for Aluminum)

a. Repeat steps from Polymer Spin Coating to Development.

b. Tape sample on sample holder and mount in the chamber. The evaporations should take place at **<5E-6 Torr**.

Table 16: Evaporation parameters for Ti, Cu and Au.

	Ti	***Cu***	***Au***
Density	**4.5 g/cm^3**	**8.93**	**19.3**
Z-ratio	**0.628**	**0.437**	**0.381**
Tooling Factor	**170 %**	**175 %**	**175 %**
Deposition Rate	**1 Å/s**	**1.5 Å/s**	**1 Å/s**
Thickness	**15 nm**	**85 nm**	**20 nm**
Current	**~30 mA**	**~ mA**	**~ 50 mA**

LIST OF REFERENCES

[1] G. Maruccio, Spintronic devices for molecular electronics, Consiglio Nazionale delle Ricerche (CNR), Italy (2006).

[2] O. Mosendz, V. Vlaminck, J. E. Pearson, F. Y. Fradin, G. E. Bauer, S. D. Bader, and A. Hoffmann, Detection and quantification of inverse spin Hall effect from spin pumping in permalloy/normal metal bilayers, *Phys. Rev. B* **82**, 214403 (2010).

[3] M. Galbiati, Molecular Spintronics (Doctoral Thesis), University of Valencia, Spain (2016).

[4] Y. Tserkovnyak, A. Brataas, G.E.W. Bauer, Enhanced Gilbert Damping in Thin Ferromagnetic Films, *Phys. Rev. Lett.* **88**, 117601 (2002).

[5] M. Farle, Ferromagnetic resonance of ultrathin metallic layers, *Rep. Prog. Phys.* **61**, 755–826 (1998).

[6] O. Yalçın, Ferromagnetic Resonance – Theory and Applications, *InTech* 978-953-51-1186-3 (2013).

[7] S. Singh, Dynamical Spin Injection in Graphene (Doctoral Thesis), University of Central Florida (2014).

[8] S. V. Vonsovskii, Ferromagnetic Resonance, *Pergamon Oxford* (1966)

[9] R. Urban, G. Woltersdorf, and B. Heinrich, Gilbert Damping in Single and Multilayer Ultrathin Films: Role of Interfaces in Nonlocal Spin Dynamics, *Phys. Rev. Lett.* **87**, 217204 (2001).

[10] Y. Tserkovnyak, A. Brataas, G. E. W. Bauer, Spin pumping and magnetization dynamics in metallic multilayers, *Phys. Rev. B* **66**, 224403 (2002).

[11] K. Xia, P. J. Kelly, G. E. W. Bauer, A. Brataas, and I. Turek, Spin torques in ferromagnetic/normal-metal structures, *Phys. Rev. B* **65**, 220401(2002).

[12] A. Brataas, Y. V. Nazarov, and G. E. W. Bauer, Finite-Element Theory of Transport in Ferromagnet–Normal Metal Systems, *Phys. Rev. Lett.* **84**, 2481 (2000).

[13] Y. Tserkovnyak, A. Brataas, G.E.W. Bauer, B. I. Halperin, Nonlocal magnetization dynamics in ferromagnetic heterostructures, *Reviews of Modern Physics*, Volume 77 (2005).

[14] K. Ando, S. Takahashi, J. Ieda, Y. Kajiwara, H. Nakayama, T. Yoshino, K. Harii, Y. Fujikawa, M. Matsuo, S. Maekawa and E. Saitoh, Inverse spin-Hall effect induced by spin pumping in metallic system, *J. App. Phys.* **109**, 103913 (2011)

[15] H.L. Wang, C.H. Du, Y. Pu, R. Adur, P.C. Hammel, F.Y. Yang, Scaling of Spin Hall Angle in 3d, 4d, and 5d Metals from Y3Fe5O12 Metal Spin Pumping, *Physical Review Letters* **112**, 197201 (2014).

[16] C. Du, H. Wang, F. Yang, P.C. Hammel, Systematic variation of spin-orbit coupling with d-orbital filling: Large inverse spin Hall effect in 3d transition metals, *Physical Review B* **90**, 140407 (2014).

[17] S. Watanabe, K. Ando, K. Kang, S. Mooser, Y. Vaynzof, H. Kurebayashi, E. Saitoh, H. Sirringhaus, Polaron spin current transport in organic semiconductors, *Nat. Phys.* **10**, 308-313 (2014).

[18] A.K. Patra, S. Singh, B. Barin, Y. Lee, J.-H. Ahn, E. del Barco, E.R. Mucciolo, B. Özyilmaz, Dynamic spin injection into chemical vapor deposited graphene, *Applied Physics Letters* **101**, 162407 (2012).

[19] S. Singh, A. Ahmadi, C.T. Cherian, E.R. Mucciolo, E. del Barco, B. Özyilmaz, Dynamical spin injection at a quasi-one-dimensional ferromagnet-graphene interface, *Applied Physics Letters* **106**, 032411 (2015).

[20] Z. Tang, E. Shikoh, H. Ago, K. Kawahara, Y. Ando, T. Shinjo, M. Shiraishi, Dynamically generated pure spin current in single-layer graphene, *Physical Review B* **87**, 140401 (2013).

[21] E. Saitoh, M. Ueda, H. Miyajima, G. Tatara, Conversion of spin current into charge current at room temperature: Inverse spin-Hall effect, *Applied Physics Letters* **88**, 182509 (2006).

[22] A. Hoffmann, Spin Hall Effects in Metals, Magnetics, *IEEE Transactions* **49**, 5172-5193 (2013).

[23] T. Tanaka, H. Kontani, M. Naito, T. Naito, D.S. Hirashima, K. Yamada, J. Inoue, Intrinsic spin Hall effect and orbital Hall effect in 4d and 5d transition metals, *Physical Review B* **77**, 165117 (2008).

[24] K. Ando, E. Saitoh, Observation of the inverse spin Hall effect in silicon, *Nat. Commun.* **3**, 629 (2012).

[25] R. Springell, S.W. Zochowski, R.C.C. Ward, M.R. Wells, S.D. Brown, L. Bouchenoire, F. Wilhelm, S. Langridge, W.G. Stirling, G.H. Lander, A study of uranium-based multilayers: I. Fabrication and structural characterization, *Journal of Physics: Condensed Matter* **20**, 215229 (2008).

[26] J. C Gonzalez-Pons, Geometrical Control of the Magnetization Direction In High-Aspect Ratio PdNi Ferromagnetic Nano-Electrodes (Honors in the Major Thesis), University of Central Florida (2008)

[27] S. Singh, M. Anguera, E. del Barco, R. Springell, and C. W. Miller, Moderate positive spin hall angle in Uranium, *Appl. Phys. Lett* **107**, 232403 (2015)

[28] J.-M.L. Beaujour, W. Chen, K. Krycka, C.-C. Kao, J.Z. Sun, A.D. Kent, Ferromagnetic resonance study of sputtered Co|Ni multilayers, *Eur. Phys. J. B* **59**, 475-483 (2007).

[29] W. Zhang, V. Vlaminck, J.E. Pearson, R. Divan, S.D. Bader, A. Hoffmann, Determination of the Pt spin diffusion length by spin-pumping and spin Hall effect, *Appl. Phys. Lett.* **103**, 242414 (2013).

[30] A. Azevedo, L.H. Vilela-Leão, R.L. Rodríguez-Suárez, A.F. Lacerda Santos, S.M. Rezende, Spin pumping and anisotropic magnetoresistance voltages in magnetic bilayers: Theory and experiment, *Physical Review B* **83**, 144402 (2011).

[31] K. Ando, S. Takahashi, K. Harii, K. Sasage, J. Ieda, S. Maekawa, E. Saitoh, Electric Manipulation of Spin Relaxation Using the Spin Hall Effect, *Physical Review Letters* **101**, 036601 (2008).

[32] L. Liu, T. Moriyama, D.C. Ralph, R.A. Buhrman, Spin-Torque Ferromagnetic Resonance Induced by the Spin Hall Effect, *Physical Review Letters* **106**, 036601 (2011).

[33] A. V. Dediu, L. E. Hueso, I. Bergenti, C. Taliani, Spin routes in organic semiconductors, *Nat. Mater.* **8**, 707 (2009).

[34] D. Sun, K. J. van Schooten, M. Kavand, H. Malissa, C. Zhang, M. Groesbeck, C. Boehme, Z. V. Vardeny, Inverse spin Hall effect from pulsed spin current in organic semiconductors with tunable spin-orbit coupling, *Nat. Mater.* **15**, 863-869 (2016).

[35] L. E. Hueso, J. M. Pruneda, V. Ferrari, G. Brunell, J. P. Valdes-Herrera, B. D. Simons, P. B. Littlewood, E. Artacho, A. Fert, N. D. Mathur, Transformation of spin information into large electrical signals using carbon nanotubes, *Nature* **445**, 410-413 (2007).

[36] D. Pesin, A. H. MacDonald, Spintronics and pseudospintronics in graphene and topological insulators, *Nat. Mater.* **11**, 409 (2012).

[37] K. S. Novoselov, A. K. Geim, S. V. Morozov, D. Jiang, Y. Zhang, S. V. Dubonos, I. V. Grigorieva, A. A. Firosov, Electric Field Effect in Atomically Thin Carbon Films, *Science* **306**, 666 (2004).

[38] N. Tombros, C. Jozsa, M. Popinciuc, H. T. Jonkman, B. J. van Wees, Electronic spin transport and spin precession in single graphene layers at room temperature, *Nature* **448** (7153), 571 (2007).

[39] A. H. Castro Neto, F. Guinea, Impurity-Induced Spin-Orbit Coupling in Graphene, *Phy. Rev. Lett.* **103**, 026804 (2009).

[40] C. Cao, M. Wu, J. Jiang, H. P. Cheng, Transition metal adatom and dimer adsorbed on graphene: Induced magnetization and electronic structures, *Phys. Rev. B.* **81**, 205424 (2010).

[41] Z. Wang, Strong interface-induced spin-orbit coupling in graphene on WS_2, *Nat. Commun.* **6**, 8339 (2015).

[42] F. Calleja, H. Ochoa, M. Garnica, S. Barja, J. J. Navarro, A. Black, M. M. Otrokov, E. V. Chulkov, A. Arnau, A. L. Vazquez de Parga, F. Guinea, R. Miranda, Spatial variation of a giant spin-orbit effect induces electron confinement in graphene Pb islands, *Nat. Phys*. **9**, 284-287 (2013).

[43] S. Singh, A. K. Patra, B. Barin (UG), E. del Barco, B. Ozyilmaz. Spin Pumping in Permalloy/Graphene and Permalloy/Graphite Interfaces, *IEEE Trans. Magn.* **49**, 3147 (2013).

[44] R. Ohshima, A. Sakai, Y. Ando, T. Shinjo, K. Kawahara, H. Ago, M. Shiraishi, Observation of spin-charge conversion in CVD grown single-layer graphene, *Appl. Phys. Lett.* **105**, 162410 (2014).

[45] J. B. S. Mendes, O. Alver Santos, L. M. Meireles, R. G. Lacerda, L. H. Vilela-Leao, F. L. A. Machado, R. L. Rodriguez-Suarez, A. Azevedo, S. M. Rezende, Spin-current to charge-current conversion and magnetoresistance in a Hybrid structure of graphene and Yttrium Iron Garnet, *Phys. Rev. Lett.* **115**, 226601 (2015).

[46] S. Dushenko, H. Ago, K. Kawahara, T. Tsuda, S. Kuwabata, T. Takenobu, T. Shinjo, Y. Ando, M. Shiraishi, Gate-tunable spin-charge conversion and the role of spin-orbit interaction in graphene, *Phys. Rev. Lett.* **116**, 166101 (2016).

[47] L. Bogani, W. Wernsdorfer, Molecular spintronics using single-molecule magnets, *Nature Materials*, vol **7** (2008).

[48] Nijhuis, C. A., Reus, W. F., Barber, J., Dickey, M. D. & Whitesides, G. M, Charge transport and rectification in arrays of SAM-based tunneling junctions, *Nano Lett*. **10**, 3611- 3619 (2010).

[49] A. S. Blum, J. G. Kushmerick, D. P. Long, C. H. Patterson, J. C. Yang, J. C. Henderson, Y. X. Yao, J. M. Tour, R. Shashidhar, B. R. Ratna, Molecularly inherent voltage-controlled conductance switching, *Nat. Mater.* **4**, 167-172 (2005).

[50] H. Park, J. Park, A. K. L. Lim, E. H. Anderson, A. P. Aliviasatos, P. L. McEuen, Nanomechanical oscillations in a single-C_{60} transistor, *Nature* **407**, 57-60 (2000).

[51] X. F. Guo, J. P. Small, J. E. Klare, Y. Wang, M. S. Purewal, I. W. Tam, B. H. Hong, R. Caldwell, L. Huang, S. O'Brien, J. Yan, R. Breslow, S. J. Wind, J. Hone, P. Kim, C. Nuckolls, Covalently Bridging Gaps in Single-Walled Carbon Nanotubes with Conducting Molecules, *Science* **311**, 356-359 (2006).

[52] L. Venkataraman, J. E. Klare, C. Nuckolls, M. S. Hybertsen, M. L. Steigerwald, Dependence of single-molecule junction conductance on molecular conformation. *Nature* **442,** 904-907 (2006).

[53] F. Prins, A. Barreiro, J. W. Ruitenberg, J. S. Seldenthuis, N. Aliaga-Alcalde, L. M. K. Vandersypen, H. S. J. van der Zant, Room-temperature gating of molecular junctions using few-layer graphene nanogap electrodes, *Nano Lett.* **11**, 4607–4611 (2011).

[54] M. L. Perrin, E. Burzuri, H. S. J. van der Zant, Single-molecule transistors, *Chem. Soc. Rev.* **44**, 902 (2015).

[55] G. Binning, H. Rohrer, *Helvetica Physica Acta* **55**, 726-35 (1982).

[56] M. Ishigami, Scanning Tunneling Microscopy of Novel Nanoscale Materials (Doctoral Thesis), University of California, Berkeley (2004).

[57] A. M. Moore, P. S. Weiss, Functional and Spectroscopic Measurements with Scanning Tunneling Microscopy, *Annu. Rev. Anal. Chem.* **1**, 857–82 (2008).

[58] A. R. Garrigues, Electrostatic Control over Temperature-Dependent Tunneling across Single-Molecule Junctions (Doctoral Thesis), University of Central Florida (2016).

[59] Landauer formalism

[60] C. Joachim, M. A. Ratner, Molecular electronics: Some views on transport junctions and beyond. *Proc. Natl. Acad. Sci. U. S. A.* **102**, 8801-8808 (2005).

[61] A. Batra, P. Darancet, Q. Chen, J. S. Meisner, J. R. Widawsky, J. B. Neaton, C. Nuckolls, L. Venkataraman, Tuning rectification in single-molecular diodes. *Nano Lett.* **13**, 6233-6237 (2013).

[62] T. Hines, I. Diez-Perez, J. Hihath, H. Liu, Z.Wang, J. Zhao, G. Zhou, K. Müllen, N. Tao, Transition from tunneling to hopping in single molecular junctions by measuring length and temperature dependence. *J. Am. Chem. Soc.* **132**, 11658-11664 (2010).

[63] X. Zhao, C. Huang, M. Gulcur, A. S. Batsanov, M. Baghernejad, W. Hong, M. R. Bryce, T. Wandlowski, Oligo(aryleneethynylene)s with terminal pyridyl groups: Synthesis and length dependence of the tunneling-to-hopping transition of single-molecule conductances. *Chemistry of Materials* **25**, 4340-4347 (2013).

[64] L. Luo, L. Balhorn, B. Vlaisavljevich, D. Ma, L. Gagliardi, C. D. Frisbie, Hopping transport and rectifying behavior in long donor–acceptor molecular wires. *J. Phys. Chem. C* **118**, 26485-26497 (2014).

[65] N. Amdursky, D. Ferber, I. Pecht, M. Sheves, D. Cahen, Redox activity distinguishes solid-state electron transport from solution-based electron transfer in a natural and artificial

protein: cytochrome C and hemin-doped human serum albumin. *Phys. Chem. Chem. Phys.* **15**, 17142-17149 (2013).

[66] M. Koch, F. Ample, C. Joachim, L. Grill, Voltage-dependent conductance of a single graphene nanoribbon. *Nat. Nanotechnol.* **7**, 713-717 (2012).

[67] K. S. Kumar, R. R. Pasula, S. Lim, C. A. Nijhuis, Long-range tunneling processes across ferritin-based junctions. *Adv. Mater.* **28**, 1824-1830 (2016).

[68] A. Migliore, P. Schiff, A. Nitzan, On the relationship between molecular state and single electron pictures in simple electrochemical junctions. *Phys. Chem. Chem. Phys.* **14**, 13746-13753 (2012).

[69] W. G. van der Wiel, S. De Franceschi, J. M. Elzerman, T. Fujisawa, S. Tarucha, L. P. Kouwenhoven, Electron transport through double quantum dots. *Rev. Mod. Phys.* **75**, 1-22 (2002).

[70] D. M. Schröer, A. K. Hüttel, K. Eberl, S. Ludwig, M. N. Kiselev, B. L. Altshuler, Kondo effect in a one-electron double quantum dot: Oscillations of the Kondo current in a weak magnetic field. *Phys. Rev. B* **74**, 233301 (2006).

[71] N. Mason, M. J. Biercuk, C. M. Marcus, Local gate control of a carbon nanotube double quantum dot. *Science* **303**, 655-658 (2004).

[72] A. R. Garrigues, L. Wang, E. del Barco, C. A. Nijhuis, Electrostatic control over temperature-dependent tunnelling across a single-molecule junction, *Nat Commun.* **7**, 11595 (2016).

[73] Nijhuis, C. A., Reus, W. F., Barber, J. R., Dickey, M. D. & Whitesides, G. M. Charge transport and rectification in arrays of sam-based tunneling junctions. *Nano Lett.* **10**, 3611-3619 (2010).

[74] H. Jeong, D. Kim, G. Wang, S. Park, H. L., K. Cho, W. Hwang, M. Yoon, Y. H. Jang, H. Song, D. Xiang, T. Lee, Redox-induced asymmetric electrical characteristics of ferrocene-alkanethiolate molecular devices on rigid and flexible substrates. *Adv. Funct. Mater.* **24**, 2472-2480 (2014).

[75] L. Müller-Meskamp, S. Karthäuser, H. J.W Zandvliet, M. Homberger, U. Simon, R. Waser, Field-emission resonances at tip/α, ω-mercaptoalkyl ferrocene/Au interfaces studied by STM. *Small* **5**, 496-502 (2009).

[76] Mentovich, E. D. *et al.* Gated-controlled rectification of a self-assembled monolayer-based transistor. *J. Phys. Chem. C* **117**, 8468-8474 (2013).

[77] A. R. Garrigues, L. Yuan, L. Wang, E. R. Mucciolo, D. Thompon, E. Del Barco, C. A. Nijhuis, A Single-level tunnel model to account for electrical transport through single molecule- and self-assembled monolayer-based junctions, *Sci. Rep.* **6**, 26517 (2016).

[78] E. Burzuri, F. Pins, H. S. J. van der Zant, Characterization of Nanometer-Spaced Few-Layer Graphene Electrodes, *Graphene* **1**, 26-29 (2012).

[79] C. Jia, A. Migliore, N. Xin, S. Huang, J. Wang, Q. Yang, S. Wang, H. Chen, D. Wang, B. Feng, Z. Liu, G. Zhang, D. Qu, H. Tian, M. A. Ratner, H. Q. Xu, A. Nitzan, X. Guo, Covalently bonded single-molecule junctions with stable and reversible photoswitched conductivity, *Science* **352**, Issue 6292, 1443-1445 (2016).

[80] S. S. Datta, D. R. Strachan, E. J. Mele, At. T. C. Johnson, Surface Potentials and Layer Charge Distributions in Few-Layer Graphene Films, *Nano Letters* **9**, No. 1 7-11 (2008).

[81] A. Castellanos-Gomez, R. H. M. Smit, N, Agrait, G. Rubio-Bollinger, Spatially Resolved Electronic Inhomogeneities of Graphene Due to Subsurface Charges, *Carbon* **50**, 932-938 (2012).

[82] D. Xiang, Y. Zhang, F. Pyatkov, A. Offenhäusser, D. Mayer, Gap size dependent transition from direct tunneling to field emission in single molecule junctions, *The Royal Society of Chemistry* (2011)

[83] J. G. J. Simmons, *Appl. Phys*. **34**, 1793 (1963).

[84] V. W. Brar, R. Decker, H. Solowan, Y. Wang, L. Maserati, K. T. Chan, H. Lee, C. O. Girit, A. Zettl, S. G. Louie, M. L. Cohen, M. F. Crommie, Gate-controlled ionization and screening of cobalt adatoms on a graphene surface, *Nature Physics* **7**, 43-47 (2010).

[85] A. Riss, S. Wickenburg, L. Z. Tan, H. Tsai, Y. Kim, J. Lu, A. J. Bradley, M. M. Ugeda, K. L. Meaker, K. Watanabe, T. Taniguchi, A. Zettl, F. R. Fischer, S. G. Louie, M. F. Crommie, Imaging and Tuning Molecular Levels at the Surface of a Gated Graphene Device, *ACS Nano* **8**, (6) 5395–5401 (2014).

[86] R. Frisenda, R. Gaudenzi, C. Franco, M. Mas-Torrent, C. Rovira, J. Veciana, I. Alcon, S. T. Bromley, E. Burzurí, H. S. J. van der Zant, Kondo Effect in a Neutral and Stable All Organic Radical Single Molecule Break Junction, *Nano Lett.* **15**, (5), 3109–3114 (2015).